Joel Matthew Kindem

115 Words

The Anomalous Magnetic Moment of the Positive Muon

A measurement of the anomalous magnetic moment of the positive muon (a_μ) has been made in a new experiment using the Alternating Gradient Synchrotron at Brookhaven National Laboratory. Polarized muons were stored in a precision magnetic field and a_μ was determined by measuring the difference frequency (ω_a) between the spin precession frequency and cyclotron frequency. A detailed analysis of the first data set (1997) is presented. Focus is on using the Ratio Method technique for extracting ω_a from the muon decay spectrum. The Ratio Method yielded the value:

$$a_\mu = 1\ 165\ 933(16) \times 10^{-9}\ (\pm 14\ ppm)\ ,$$

where the values of $\frac{\omega_a}{\omega_p} = 3.707\ 245(52) \times 10^{-9}$ and $\frac{\mu_\mu}{\mu_p} = 3.183\ 345\ 47(47)$ were used to calculate a_μ. This value of a_μ agrees with the Standard Model prediction to within one standard deviation

$$a_\mu^{SM} = 1\ 165\ 916.28(77) \times 10^{-9}\ (\pm 0.66\ ppm)\ .$$

UNIVERSITY OF MINNESOTA

This is to certify that I have examined this bound copy of a doctoral thesis by

Joel Matthew Kindem

and have found that it is complete and satisfactory in all respects and that any and all revisions required by the final examining committee have been made.

Professor Priscilla Cushman

(Faculty Adviser)

GRADUATE SCHOOL

The Anomalous Magnetic Moment of the Positive Muon

A THESIS
SUBMITTED TO THE FACULTY OF THE GRADUATE SCHOOL
OF THE UNIVERSITY OF MINNESOTA
BY

Joel Matthew Kindem

IN PARTIAL FULFILLMENT OF THE REQUIREMENTS
FOR THE DEGREE OF
DOCTOR OF PHILOSOPHY

September, 1998

The Anomalous Magnetic Moment of the Positive Muon

by Joel Matthew Kindem

Under the supervision of Professor Priscilla Cushman

ABSTRACT

A measurement of the anomalous magnetic moment of the positive muon (a_μ) has been made in a new experiment using the Alternating Gradient Synchrotron at Brookhaven National Laboratory. Polarized muons were stored in a precision magnetic field and a_μ was determined by measuring the difference frequency (ω_a) between the spin precession frequency and cyclotron frequency. A detailed analysis of the first data set (1997) is presented. Focus is on using the Ratio Method technique for extracting ω_a from the muon decay spectrum. The Ratio Method yielded the value:

$$a_\mu \quad = \quad 1\ 165\ 933(16) \times 10^{-9}\ (\pm 14\ ppm)\ ,$$

where the values of $\frac{\omega_a}{\omega_p} = 3.707\ 245(52) \times 10^{-9}$ and $\frac{\mu_\mu}{\mu_p} = 3.183\ 345\ 47(47)$ were used to calculate a_μ. This value of a_μ agrees with the Standard Model prediction to within one standard deviation

$$a_\mu^{SM} \quad = \quad 1\ 165\ 916.28(77) \times 10^{-9}\ (\pm 0.66\ ppm)\ .$$

Acknowledgements

My first thought, when writing these acknowledgments, was to think of some criteria by which I would include people who had helped with the direct writing and compilation of my thesis. After giving it a second thought, I realized what a bad idea this was. Its really the idea behind the thesis—the culmination of an education spanning an entire lifetime—which is important. In this respect, I would like to try and thank all those people throughout the years who have formed and changed the way I've thought about the world, and who are responsible for my education.

Thanks first to my parents Roald and Shirley, for giving me unmeasurable love and support as well as so many great brothers and sisters (spouses): Mark (Miriam), Mike (Diane), Kris (Jean), Kari (Thomas), Erik, Peter (Gabrielle), and Randi (Albert). From my family members alone, I've received a well rounded education, learning from each of their varied interests. I can think of no family that I would rather be a part of!

Thanks to all the kids from the neighborhood where I grew up, spending every afternoon playing some kind of sport: Cory and Craig Cook, Jason Hunkins, Scott Horn, Dave Schmidt, Spencer Metcalf, Doug and Brett Tomlinson, Rod and Rob Kubier, Greg Bried, and Eric English.

Thanks to my great teachers throughout the years: Grade school—Betty Ward, Mr. Fratske, Mr. DeLong; High School—Ms. Lee, Mr. Strandquist, Corby Smith, Bud Bjornaraa, Neil Michels (who introduced me to physics!); College—Randall Brown, Dennis Barnaal, Loyal Rue; Grad—Ben Bayman, Leonid Glazman, and Oriol Valls.

Thanks to everyone who went to Luther College in 1987–91 for making it four of the best years of my life, especially: my roommates—Todd Borgie, Jim Fletcher, John Hatle, Wes Jorde; my "physics friends"—Brent Englebert, Pete Lee, Paul Ferlemann, Randy Cheney, John Moore, Paul Halverson, my Norse Football teammates, and my Sigma Chi Theta fraternity brothers.

Special thanks to my long time friend Mark Gray, first boss Duane Moe, and co-workers Chris Ingerson and Tom Hesse, for raising my standard of a hard days work.

Thanks to my Grad School friends at Minnesota—Dave Dikeman, Mike Naus, and Jason Sielaff, for making Grad School feel like the right choice; and my roommates—Jim Fletcher, A.J. Dull, Scott Greseth, Steve Giron, and Greg Brown for dealing with me.

Experiencing Brookhaven first hand—through test beams, data runs, and living on site—gave me the chance to fully understand what a monumental and collaborative effort an experiment like (g-2) really is. This thesis would certainly not have been possible without the dozens of highly skilled professionals working together. Thanks to everyone at (g-2)! Special thanks goes out to those who made life at Brookhaven more enjoyable: Jim Ablett, Tracy Zaslow, Rich Larson, Arnie Stillman, Ofer Rind, Bill Deninger, Axel Steinmetz, Matt Hare, and the countless undergraduate students on the ultimate field. The Minnesota contingent—Adriaan Heering, Dean Miller, Long Duong, Ron McNabb, Charles Timmermans, Ivan Kronkvist, and Matt Schmidt. Many thanks also go out to direct contributors and readers of my thesis: Sergei Sedykh, Dave Kawall, Stratos Efstathiadis, Lee Roberts, Jim Miller, Francis Farley, Yannis Semertzidis, Gerry Bunce, Bill Morse, Rob Carey, and Vanya Logashenko. Extra thanks to Sergei Redin for several of his figures which helped me finish on time, and to my advisor Prisca Cushman for her skillful editing, patience, and financial support over the past four years.

Last but not least I'd like to thank Susan Hansen for all her love, patience, and support that was necessary in making a three year New York-to-Iowa relationship work.

Table of Contents

List of Tables

List of Figures

Chapter 1

Introduction

A key pursuit in modern high-energy physics is to test the reach of the Standard Model (SM). This is done by either directly observing deviations from the SM (looking for *new* physics) or by measuring quantities that the SM predicts (determining at what level the SM breaks down). This thesis describes the latter pursuit, a precision measurement of the anomalous magnetic moment of the positive muon (a_μ). Throughout this thesis (g-2) and a_μ are synonymous.

The ultimate goal of experiment E821 taking place at Brookhaven National Laboratory (BNL), is to measure a_μ to a precision of 0.35 parts per million (ppm). This represents a factor of 20 improvement on the experimental precision of 7.3 ppm, measured by the last CERN experiment [1, 2]. In this thesis, detailed analysis is presented for the first set of data, taken in April–July of 1997. The precision of this measurement was limited by statistics to 14 ppm. Many things were learned en route to completion of this first run. This thesis will be focused more on illuminating the path by which we came, the obstacles that were overcome, and the techniques that were developed, since any meaningful statements about limits to the SM must await the more precise measurement expected in the upcoming set of runs (August 1998 and January 1999).

1.1 Definition of g and a

The magnetic moment of a particle or atomic system in free space is given by [3]

$$\vec{\mu} = \gamma_g \hbar \vec{J} = g \mu_B \vec{J} \ , \tag{1.1}$$

where the total angular momentum ($\hbar\vec{J}$) is the sum of the orbital ($\hbar\vec{L}$) and spin ($\hbar\vec{S}$) angular momenta, and where the Bohr magneton ($\mu_B = e\hbar/2mc$) is the fundamental unit of the magnetic moment. The constant γ_g is called the gyromagnetic ratio and is the ratio of the magnetic moment to the angular momentum; g is called the g factor and characterizes the strength of the magnetic moment. Dirac's theory predicts a value of $g = 2$ for a point lepton ($L = 0, S = 1/2$); however, the measured value is $g \approx 2.002$. Thus, g is usually written in terms of a which is called the *anomalous* g factor

$$g = 2(1 + a) \ . \tag{1.2}$$

Hence, a is defined

$$a \equiv \frac{g-2}{2} \ . \tag{1.3}$$

Comparing a for a proton to a for an electron or muon, we see that for a proton (which has constituent quark and gluon mass distribution) $a_p = 1.79$, while for an electron or a muon $a_{e,\mu} \approx 0.001$. This reflects the fact that a lepton is a 'point-particle' whose charge extension is only due to the cloud of virtual particles surrounding it [4].

1.2 Motivation and Theory

A precision measurement of a_μ provides a means to see the average effect of quantum fluctuations of the particle. Governed by the Uncertainty Principle, a charged particle emits and absorbs virtual particles. When the particle travels through an external magnetic field, photons from the field interact with the 'fluctuating' particle, in turn affecting its spin and magnetic moment. This can be seen schematically in the form of

Feynman diagrams, Figure 1.1 shows a subset of the diagrams which contribute to the Standard model prediction for (g-2). An interesting feature of the (g-2) experiment is that it is an expectation value experiment (i.e., directly proportional to a_μ). It therefore has further reach in testing predicted higher-order contributions than a cross-section or lifetime measurement, which are based on calculations involving the square of the expectation value.

1.2.1 The Standard Model prediction for a_e

For the electron, the anomaly is well understood, and theory and experiment are in excellent agreement

$$a_e\,(expt) - a_e\,(theo) = (33 \pm 23) \times 10^{-12}. \tag{1.4}$$

The value of $a_e\,(theo)$ has been calculated by perturbation theory as a power series in α according to QED. T. Kinoshita *et al.* have calculated terms through α^4 [6] with the expansion written:

$$a_e\,(theo) = C_1(\frac{a}{\pi}) + C_2(\frac{a}{\pi})^2 + C_3(\frac{a}{\pi})^3 + C_4(\frac{a}{\pi})^4 + \cdots \tag{1.5}$$

$$\begin{aligned} C_1 &= +0.5 \\ C_2 &= -0.328\ 478\ 965 \\ C_3 &= +1.181\ 241\ 456 \\ C_4 &= -1.409\ 2(384)\ , \end{aligned}$$

where uncertainty in C_4 is due to evaluation by numerical integration. The result from (1.5) only includes virtual photon, electron, and positron fields; muon, tau, hadronic, and electroweak contributions must also be added:

$$\begin{aligned} a_e{}^{muon} &= 2.711 \times 10^{-12} \\ a_e{}^{tau} &= 0.010 \times 10^{-12} \\ a_e{}^{had} &= 1.64(4) \times 10^{-12} \\ a_e{}^{weak} &= 0.030 \times 10^{-12} \end{aligned}$$

All together

$$a_e\,(theor) = 1\ 159\ 652\ 155.6(22.9) \times 10^{-12}\ , \tag{1.6}$$

where the error is dominated by the value of $\alpha = e^2/\hbar c$ which is based on a measurement of the quantum Hall effect [7].

The value of a_e (expt) has been measured by observing transitions between low-lying orbital and spin states for a single electron in a Penning trap with a field of 5 Tesla and at a temperature of 4.2 K [8] using microwave spectroscopy. The reported value is,

$$a_e\,(expt) = 1\ 159\ 652\ 188.4(4.3) \times 10^{-12}\ . \tag{1.7}$$

Since contributions other than electromagnetic are small, the calculation of a_e represents a relatively *pure* QED process. Therefore, agreement between theory and experiment solidly confirm QED to this level.

1.2.2 The Standard Model prediction for a_μ

With confirmation of QED at the ppb level from a_e, a measurement of a_μ will provide complementary information: a test of the hadronic and electroweak aspects of the Standard Model. Since the muon has a mass ~200 times that of an electron, additional virtual processes contribute to a_μ. Specifically, the virtual photon in Figure 1.1 acts like a 'mini-particle accelerator', with the energy scale set by the square of the external particle mass. In the case of the muon, the virtual photon energy scale is a factor of $(\frac{m_\mu}{m_e})^2 \approx 40000$ times greater than the electron.

The theoretical value of a_μ in the Standard Model has its dominant contribution from QED, but strong and electroweak interactions also contribute at the level of the BNL experiment [9]. Table 1.1 summarizes the QED, hadronic, and electroweak contributions to Standard Model contributions to a_μ. From table 1.1, one can see that measuring

Table 1.1: Current QED, Hadronic, and electroweak contributions to a_μ, and reference.

Theory	a_μ $\times 10^{-9}$	a_μ *ppm*	reference
QED	1 165 847.06(2)	—	[10]
Had	67.71(77)	58.1±0.66	[11, 12, 13]
Weak	1.51(4)	1.3±0.03	[10, 14]
SM	1 165 916.28(77)	±0.82	[10, 14]

a_μ to a precision 0.35 ppm will test both hadronic and electroweak contributions. Most importantly, agreement of theory and experiment at this level would demonstrate that the renormalization prescription of unified electroweak theory is correct, as well as put constraints on 'new physics'.

Some 'new physics' includes the following: compositeness models, super-symmetric particles, and the Higgs. The influence of compositeness (substructure) on a_μ has been detailed in [15]. Essentially, agreement between a_μ (expt) and a_μ (SM) will set a length scale (size) cut off only below which substructure could exist. Super-symmetric particles are thought to have masses on the order of the electroweak mediators ($W^\pm$ and Z); thus, contributions to a_μ should show up at a similar level [16, 17]. On the other hand, the Higgs, which has a constrained mass that is substantially higher than a W or Z, will make a negligible contribution to a_μ (<0.01 ppm) [18].

At present, uncertainties in hadronic contribution would prevent full use of such a precise measurement. The hadronic contribution comes principally from the single vacuum polarization loop with hadrons present. The calculation cannot now be done from first principles using QCD, so the calculation is done using a dispersion relation based on an experimentally measured ratio

$$R(s) = \frac{\sigma_{tot}(e^+ + e^- \rightarrow hadrons)}{\sigma_{tot}(e^+ + e^- \rightarrow \mu^+ + \mu^-)} \ , \tag{1.8}$$

where s denotes the total energy squared measured in the center of mass frame. In addition to the single vacuum polarization loop contribution, higher order terms from hadronic vacuum polarization [12] and light-by-light scattering [13] must be added. It is expected that current activities at the e^+e^- colliders of BINP, Beijing, Frascatti, and Cornell, will reduce the theoretical uncertainty in a_μ (Had) and consequently a_μ (SM). It is likely that this uncertainty will be at or below the level of the 0.35 ppm measurement [18].

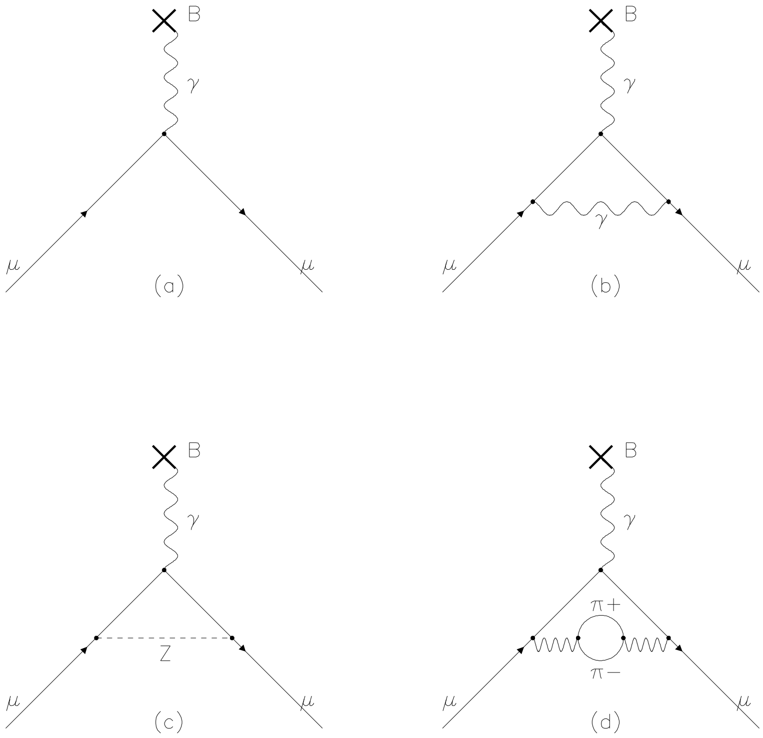

Figure 1.1: Feynman diagrams for fluctuating muon and an external magnetic field. (a) The tree-level diagram: the muon interacts solely with the external field, producing the Dirac result (g=2). (b) The lowest-order QED radiative correction: the muon emits a virtual photon , interacts with the external field, and then absorbs the virtual photon (the Schwinger [5] term). (c) The lowest order Electroweak diagram: the muon emits and absorbs a virtual mediator of the weak force (Z, W^+, W^-), in this case shown with a Z. (d) A sample QCD diagram: the muon emits a virtual photon which undergoes hadronization—production of strongly interacting quark and anti-quark pairs. In the picture shown, virtual quark pairs (u and d) form a $\pi^+\pi^-$.

Chapter 2

Measuring a_μ

2.1 Principle

The principle behind measuring a_μ is the same as that used 20 years ago in the third CERN experiment. The (g-2) precession frequency, which is the difference between the spin precession frequency and the cyclotron frequency, is measured in the precision magnetic field of a storage ring. The basic equations for the spin precession frequency ω_s and the cyclotron frequency ω_c for a charged particle moving in a uniform constant magnetic field are:

$$\omega_s = \frac{geB}{2mc} + (1-\gamma)\frac{eB}{mc\gamma} \tag{2.1}$$

$$\omega_c = \frac{eB}{mc\gamma}\ , \tag{2.2}$$

where γ is the relativistic factor. The first term in Eq. (2.1) is the Larmor precession frequency (the spin precession of a particle at rest) and the second term is the Thomas precession frequency (the kinematic precession arising from the particle's acceleration perpendicular to the particle's velocity [19]). Hence, the (g-2) precession frequency ω_a is

$$\omega_a = \omega_s - \omega_c = \left(\frac{g-2}{2}\right)\frac{eB}{mc} = a\,\frac{eB}{mc}\ . \tag{2.3}$$

In order to keep polarized muons in the storage ring for many turns, it is necessary to use focusing quadrupoles. Electrostatic quadrupoles are used because an electric field ($\vec{E}$) modifies Eq. (2.3) as follows:

$$\vec{\omega}_a = \frac{e}{mc}\left[a_\mu \vec{B} - \left(a_\mu - \frac{1}{\gamma^2 - 1}\right)\vec{\beta} \times \vec{E}\right]. \tag{2.4}$$

Thus, the contribution of an electric field to ω_a can be made zero by choosing γ such that

$$\left(a_\mu - \frac{1}{\gamma^2 - 1}\right) = 0. \tag{2.5}$$

At $\gamma = 29.3$ (the so-called 'magic' γ), the second term in Eq. (2.4) goes to zero, and there is focusing and storage without affecting ω_a! This fixes the muon orbital momentum in the ring to be p_μ=3.09 GeV/c. B is chosen to be 1.45 Tesla [20], which in turn fixes the storage ring radius at 7.11 m.

2.2 Overview

The (g-2) experiment is designed to operate in two modes: pion injection and muon injection (data for this thesis was collected exclusively using pion injection). Protons from the AGS hit a target, and resulting pions are channeled down the beamline (refer to Figure 2.1). In the beamline a fraction of the pions decay via $\pi \rightarrow \mu\nu_\mu$. For pion injection, the pion fraction is directed through a superconducting inflector into the storage ring where a small fraction get 'kicked' onto stored orbits from the momentum transfer in the decay. For muon injection, the muons are directed into the ring and are deflected via a 'kicker' magnet onto stored orbits. In both cases, non-conservation of parity in the decay results in the high energy and forward component of decay muons becoming longitudinally polarized (i.e., the decay muon spin starts with the same phase relative to their momentum vector).

At injection, those pions which do not decay to captured muons create an intense burst of radiation as they strike the storage ring walls. This causes a large background in

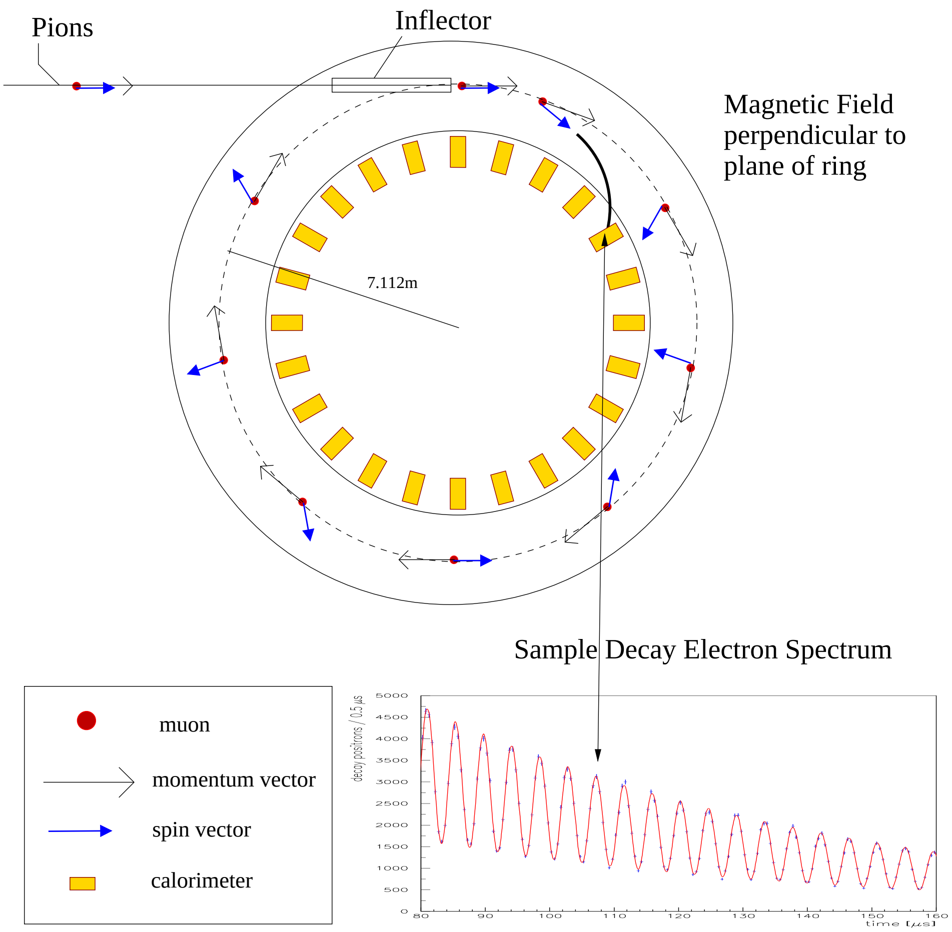

Figure 2.1: Overview of the (g-2) experiment (not to scale).

the electron detectors called the 'flash'. The flash has two components: (1) The prompt flash, due to the $\sim 6 \times 10^7$ charged particles striking the detectors at injection. (2) The delayed flash, due to the bath of neutrons and induced γ's reaching thermal equilibrium.

In the ring, stored muons circulate, their spin precesses, and they eventually decay according to $\mu \rightarrow e\nu_\mu\nu_e$. Decay electrons spiral inward and are recorded in one of the 24 calorimeter stations spaced evenly around the inner perimeter of the ring. High-energy decay electrons (>1.6 GeV) are more likely to be recorded if the spin of their parent muon was pointed in the direction of a calorimeter when they decayed due to their longitudinal polarization. This creates a modulation of the exponential muon lifetime by a frequency ω_a. The number of forward-going, high-energy decay electrons striking a calorimeter has the functional form:

$$N(t) = N_{\circ} e^{-t/\gamma\tau}[1 - A\cos(\omega_a t + \phi)], \tag{2.6}$$

where $N_{\circ}$ is the number at $t = 0$, A is the asymmetry (i.e., amplitude of oscillation), $\gamma\tau$ is the muon lifetime in the laboratory ($\sim 64.4\mu$s), and ϕ is the phase of the oscillation. The main focus of the (g-2) analysis is to extract a precise value of ω_a from careful fits of the decay spectrum, while eliminating sources of systematic error that can shift its fit value. The statistical accuracy with which ω_a can be determined from the observed decay electron distribution is given by:

$$\frac{\delta\omega_a}{\omega_a} = \frac{\sqrt{2}}{\omega_a A\gamma\tau\sqrt{N_e}}, \tag{2.7}$$

where N_e is the total number of decay electrons observed.

Taking the ratio of the Larmor precession frequency ω_L in Eq. (2.1) to ω_a

$$\frac{\omega_a}{\omega_L} = \frac{a}{1+a}. \tag{2.8}$$

From a separate experiment [21], the value of ω_L is determined from the ratio of muon to proton magnetic moments at rest $\lambda = \mu_\mu/\mu_p = 3.183\ 345\ 47(47)$ together with measurement of the magnetic field B in terms of the proton precession frequency ω_p ($\omega_L = \lambda\omega_p$). Hence

$$a = \frac{\omega_a}{\lambda\omega_p - \omega_a} = \frac{\mathcal{R}}{\lambda - \mathcal{R}}\ , \tag{2.9}$$

where

$$\mathcal{R} = \frac{\omega_a}{\omega_p} = \frac{f_a}{f_p}\ . \tag{2.10}$$

Ultimately, the (g-2) experiment measures the value of $\mathcal{R}$.

Chapter 3

Apparatus

The experiment took place at BNL, using the Alternating Gradient Synchrotron (AGS) proton beam as the source for stored muons. Figure 3.1 shows a plan view of the site.

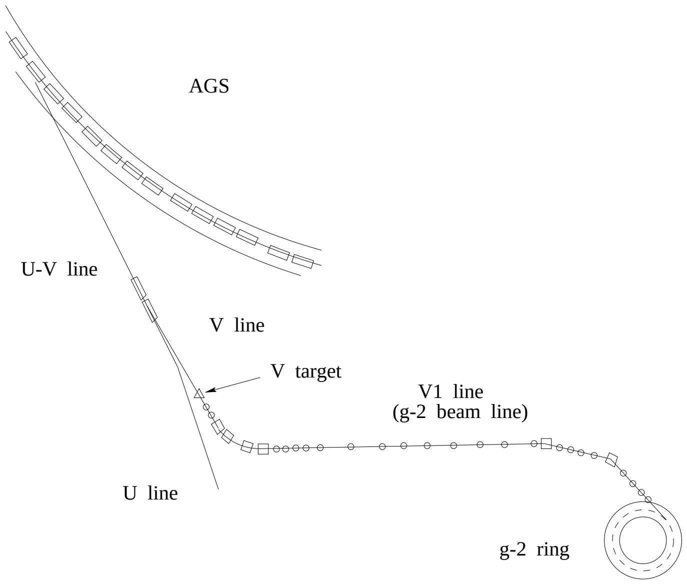

Figure 3.1: Plan view of AGS, beamlines and (g-2) storage ring.

3.1 AGS

An AGS cycle was repeated every 2.6 seconds during stable running conditions and consisted of the following. Protons from the 200 MeV LINAC were injected into the AGS booster and accelerated to 1.6 GeV with a second harmonic to give two bunches. These bunches were transferred to the AGS ring and this process was repeated four times to give 8 bunches [22]. In the AGS, the 8 bunches were accelerated to final momentum of 24 GeV/c, where they were separated by 337 ns and had a full AGS period of 2.69μs. Each bunch had a width of 27 ns and was extracted via a pulsed kicker-magnet into the U-beamline at intervals of 33 ms. Intensity of the proton bunches varied throughout the run. The design goal was to run at 60 Tera-protons (TP) per AGS cycle. Losses at extraction and in the U and V transfer lines tripped off radiation monitors that were too sensitive. This, combined with the larger flash associated with higher intensity, precluded practical running at intensities greater than 40 TP per AGS cycle. Even at 40 TP, radiation monitors would occasionally trip due to injection loss. In the end, running was more stable at the lower intensity of 30 TP.

3.2 U-V Beamline

After extraction from the AGS, protons were deflected $\sim 3^\circ$ from the U-line to the V-line and directed at the V-target station. The (g-2) experiment shared the U-line with the RHIC facility, which is responsible for instrumentation and software for the U-line. We used their existing monitoring for the U-line but found it to be problematic in the sense that feedback was slow and no expert for that control system was on duty for (g-2) running. Sensitive controls amplified the effect of slow feedback. Radiation monitors would trip off beamline magnets as a result of losses incurred during magnet adjustment. This system will be improved in the next run so that the beam can be better tuned, reducing losses and therefore allowing for higher intensity running.

3.3 V Target

The target was designed to handle the high peak and average beam intensities of 60 TP per AGS cycle. The target was a cylindrical sandwich of nickel disks. It was steadily rotated about its axis through a partial bath of water, so heating from the 8 bunches was distributed and the high average heating was reduced.

3.4 V1 Beamline

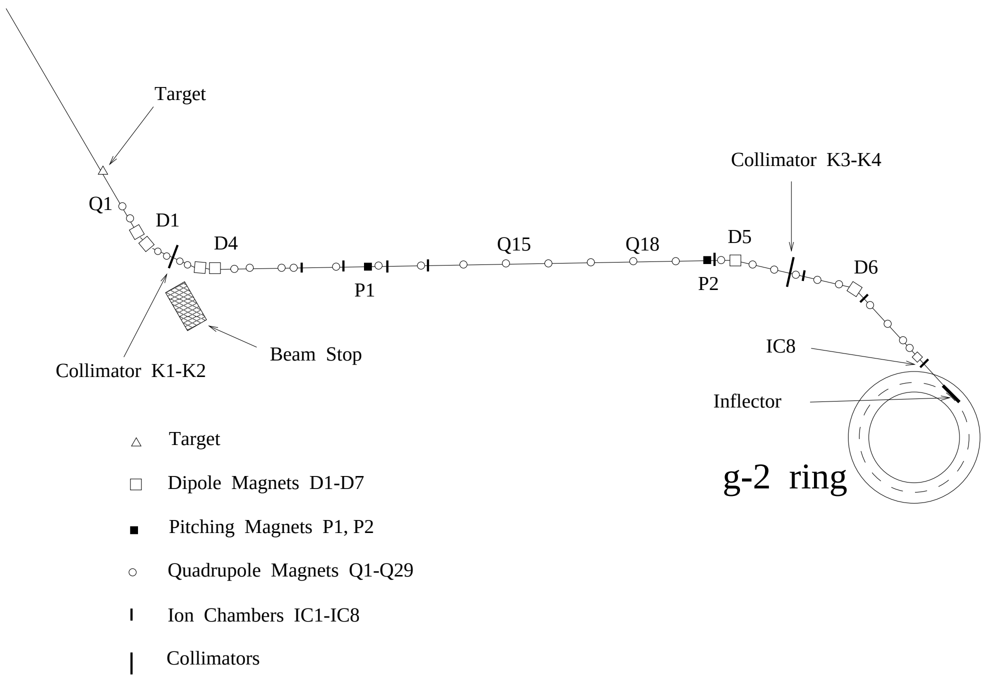

Figure 3.2: V1-beamline: magnets and instrumentation.

The long (116 m) secondary beamline channeled the pions to the ring for injection and provided a decay volume for the $\pi \rightarrow \mu\nu_\mu$ decay. After the target, two large dipoles, in combination with momentum defining slits, selected π^+ with a central momentum of 3.11 GeV (0.5% higher than the 'magic' momentum). The momentum width ($\frac{\Delta p}{p}$ =0.5–2.0%), was determined by adjusting the slits. The slit apertures were reduced from the design reports 2% setting, in order to increase the ratio of detected decay electrons to flash (signal to noise) seen by the calorimeters. After momentum selection, the pions were manipulated through a variety of beamline elements including: steering dipoles, focusing and defocusing quadrupoles, pitching magnets, and further momentum selecting slits (see Figure 3.2). These elements, together with an array of beamline instrumentation, were used to 'tune' the beam in order to maximize the number of detected decay electrons.

There was an additional loss of pions due to multiple scattering (~30%) in a section of the beamline just downstream of the target where a mylar window had broken. Due to radiation safety concerns, the window could not be fixed during the 1997 run. For the 1998 run this section of beamline will be operated with helium instead of vacuum. This should reduce multiple scattering losses, as well as eliminate the strain on the mylar window that broke due to a combination of high intensity running and the vacuum-atmosphere pressure differential.

3.5 Beamline Instrumentation

The V and V1 beamline instrumentation consisted of a flag, segmented wire ion chambers (SWICs), a calibrated secondary emission chamber (SEC), and calibrated ion chambers (see Figure 3.2 for location of beamline monitoring elements). For fast timing of the injected bunch, a Čerenkov counter ('T∅ ') was placed in the beam just prior to the entrance of the ring.

3.5.1 Flag, SWIC and Ion Chamber

The flag was a phosphorescent screen located just upstream from the V target which lit up when the proton beam passed through it. A CCD camera, focused on the flag, directed the image to a television monitor. The flag demonstrated that things were basically working by showing the position of the beam and its relative brightness.

The SWICs were monitoring devices that provided pion beam profiles. High voltage is applied between a cathode plane and anode wires of a SWIC. The plane and wires are in a volume filled with special gases; in our case, they were operated at $\sim$1000 V and with a gas mixture of 50% carbon dioxide and 50% argon. When charged particles pass through the active volume of a SWIC, electron ion pairs are produced [23]. The electrons drift to the wires which are closest and provide position information. In general, wires have integrating amplifiers (capacitors for higher intensity running) that get reset by a trigger pulse, after which they integrate until they receive a hold signal. In practice (at BNL), the levels on the wires are sampled by multiplexing the voltage level from the amplifiers onto a serial line which gets plugged into an oscilloscope. The signal is continually rebroadcast and either a separate signal line, or a signal on the broadcast line, is used for triggering the scope. Typically the SWICs have been used in slow extracted beams where the signal on the wires continually builds over the roughly 3-second cycle and can be viewed quite easily on an analog scope. However, for the (g-2) experiment, we needed to look at 8 bunches separated by just 33 ms, which would have required the use of a digital oscilloscope. Since there are 10 SWICs in the beamline, each with an x- and y-plane, 20 channels of digital scope information would have been necessary. I therefore designed and built a CAMAC module that digitized 16 channels worth of SWIC information for the 8 fills of the experiment. This CAMAC module, along with a stand-alone data acquisition system and graphical user interface, is described in [24].

The ion chambers were calibrated devices used to measure the number of charged particles in the beam. The ion chambers worked in a similar fashion to the SWICs, having a single anode plane instead of separate anode wires, and essentially integrated the SWICs profiles. Ion chambers had either amplifiers or capacitors (like the SWICs) that integrated the charge induced by passing particles, producing a proportional voltage level. For the ion chambers, this level was converted to a pulse train and was fed into a scaler, whose count was calibrated to a known number of particles: 88$\pm$17 counts corresponded to 1×10^7 charged particles [32]. The ion chamber scaler readout was also incorporated into the SWIC read out and display system which is described in [24].

3.5.2 T∅ Counter

The T∅ counter was used to measure the timing and shape of particle bunches injected into the ring. It was a 1 mm-thick Lucite Čerenkov counter, 10 cm in diameter, read out by a 2" photomultiplier tube (PMT) placed one foot below the plastic. The Lucite was wrapped in black paper to reduce light output. Black paper, with a hole about 1/4" in diameter, was also used to cut down the active aperture on the photocathode [25]. The signal was split to a discriminator, waveform digitizer, and two ADCs. One of the ADC inputs was attenuated by a factor of ten to cover a larger dynamic range.

The T∅ counter was useful for giving a time marker and displaying the shape of the input bunch. A comparison between ion chamber 710, located one foot away, showed that the number of ion chamber counts were generally in agreement with the integrated pulse from T∅ . Due to continual beam tuning and increasing intensities, the counter was not very useful as an intensity monitor. The T∅ counter showed the FWHM of the beam to be about 60ns. Comparison of the timing from the T∅ counter with the pre-bunch signal from the AGS (induced by the bunch extraction kicker magnet) showed a jitter on the order of several nanoseconds. The reproducibility of the pre-bunch signal allowed it to be used to define $t = 0$. This was convenient because it came 35μs before injection instead of at injection. For this reason, it could be used to initiate gating pulses for the electron detector PMTs and start the read-out electronics.

3.6 Superconducting Inflector

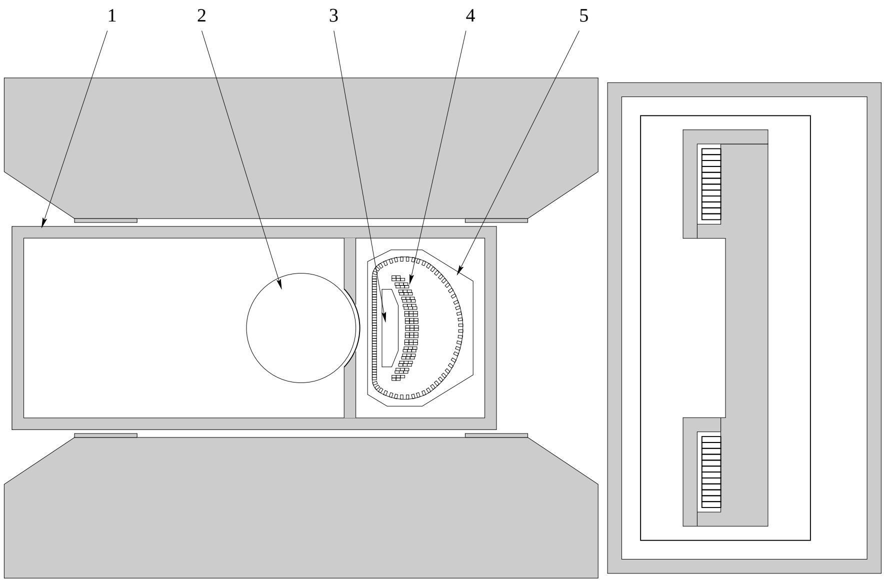

Figure 3.3: Cross-section of inflector and vacuum chamber: 1–Vacuum chamber wall, 2–Muon storage region, 3–Beam channel, 4–Coils, 5–Inflector body.

Ideally, particles in the beam should see a step function transition from the zero field outside the ring to the 1.5 Tesla field inside the ring. The inflector realized this transition by creating a homogeneous dipole magnetic field (1.5 Tesla) over the length of its 1.7 meters, canceling the integrated fringe field from the storage ring. The inflector used a superconducting sheet to cancel its own fringe field, minimizing its field's effect on the precision magnetic field of the storage ring [26] (see Figure 3.3).

When the main magnet was energized, a magnetic flux was created through the superconducting sheet. As the inflector was cooled down, its coils and sheet became superconducting. The inflector was then energized, creating a dipole field that canceled that of the main magnet within the inflector channel (a small region 18 mm horizontal by 45 mm vertical where the beam will pass). The superconducting sheet then served to cancel out the fringe field from the inflector coils, since the amount of flux passing through the sheet should remain fixed. Because the superconducting sheet was actually formed from coiled superconducting wire, the fringe field cancelation was not perfect. However, this was not a problem [27] since the inflector fringe field fell off rapidly.

3.7 Precision Muon Storage Ring

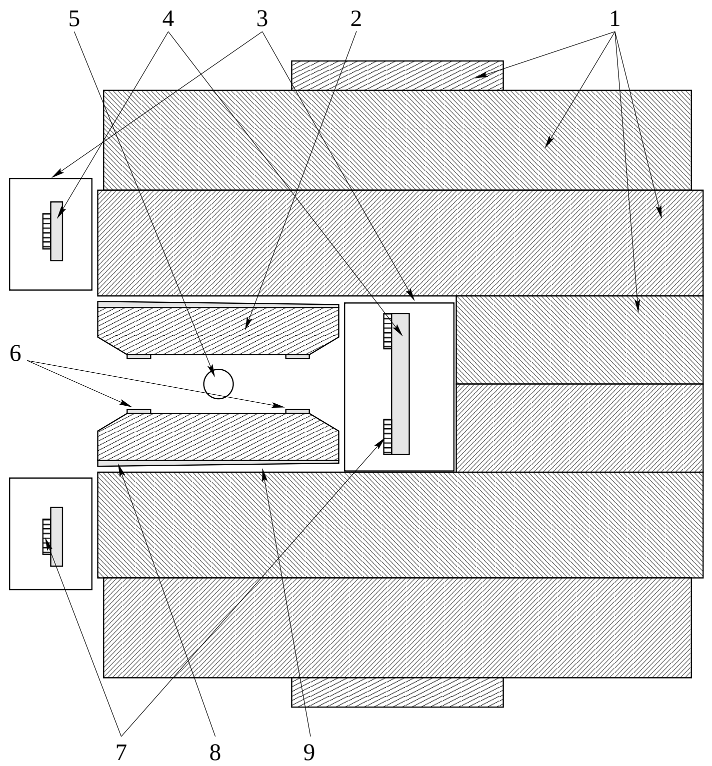

Figure 3.4: The 'C' of the magnet opens on the inside of the ring and electrons from the muon decays are detected on the inner perimeter. 1–Yoke plates, 2–Pole, 3–Cryostat, 4–Mandrel, 5–Muon storage region, 6–Rose shims, 7–Superconducting coils, 8–Wedge shims, 9–Air gap.

The muon storage ring provided a field of 1.45 Tesla, over a storage region that was 14 m in diameter which had a circular cross-section 9 cm in diameter, where the muons circulated, precessed, decayed, and then exited the storage region. Figure 3.4 shows a cross-section of the magnet.

3.7.1 Main Magnet

The main magnet for the (g-2) storage ring was an iron C-magnet excited by superconducting coils. The eventual goal for the 0.35 ppm measurement is to know the field over the muon phase space to 0.1 ppm. For the 1997 run, which was statistics limited only, the requirements on the field were less stringent, and the field sampled by the muons was measured to about 0.9 ppm [27, 28]. Reference [20] contains a complete description of main magnet construction and operation.

3.7.2 Monitoring the Magnetic field

With the vacuum chamber in place, measurement of the magnetic field in the storage region was accomplished by using 366 fixed NMR probes (probes distributed evenly in azimuth, and attached in grooves to the outside top and bottom walls of the vacuum chamber), together with 17 movable NMR probes (probes distributed over the cross-section of the storage region and attached to a movable trolley [29]). The trolley ran along specially designed rails mounted on the inside of the vacuum chamber (see Figure 3.5). The trolley was pulled around the ring via two cables, and measured the field every 0.7 cm. Its position within the vacuum chamber was read out using a bar-code etched in the trolley rails. The trolley was parked out of the storage region when taking data. The field was monitored continually with the fixed probes, and when there was 'down-time' (1–2 times per week) the trolley system would take about two hours to map the field in the ring, for later offline calibration of the fixed probes. This combined system of NMR probes permitted relative monitoring of the magnetic field to about 0.9 ppm [27]. The absolute calibration of the NMR probes in the trolley was obtained by calibrating them with a special NMR probe which contained a spherical volume of pure water for which the ratio of the proton magnetic moment to that of a free proton was known [30, 31].

3.7.3 Vacuum Chamber

The storage region was maintained at a vacuum of $< 3 \times 10^{-6}$ Torr (running with positive muons) to reduce multiple scattering and prevent electrostatic breakdown between the quadrupole plates. The vacuum was achieved through use of 4 rough pumps, 4 turbo pumps, and 40 distributed ion pumps, capable of pulling vacuum to the range of 5×10^{-6} Torr in about 3–4 hours. A 'scalloped' design for twelve 28°vacuum chamber sections was used in order to minimize the amount of material that decay electrons would have to traverse in route from the storage region to the electron detectors (see Figure 3.7). This design insured that the analyzing power of the decay electrons was maintained, so that the asymmetry was not reduced.

3.7.4 Electrostatic Quadrupoles

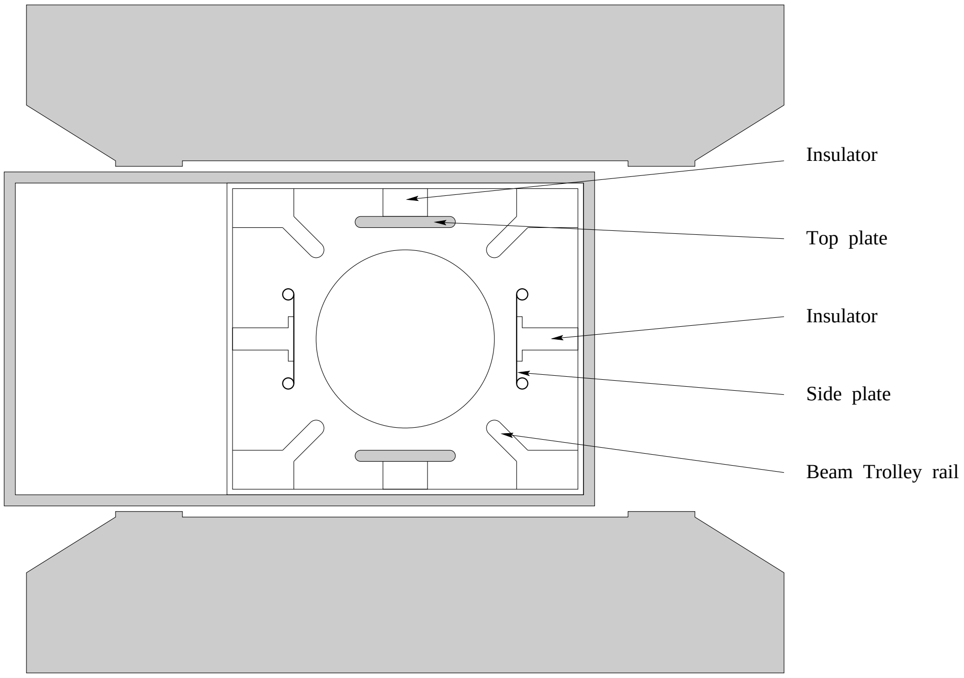

Figure 3.5: Cross-section of vacuum chamber with electrostatic quadrupole.

After traveling through the inflector channel (73% transmission [32]), a small fraction

($\sim$25 ppm, or 465 muons per TP [32]) of the transmitted pions were kicked onto stored orbits from the momentum transfer in $\pi \rightarrow \mu\nu_\mu$. There, four sections of pulsed electrostatic quadrupoles weakly focused the muons and prevented them from exiting the ring vertically due to their initial momentum spread (Figure 3.5 details the cross-section of quadrupole section). The quadrupole plates were pulsed to prevent electrostatic breakdown. The plates were energized for roughly 35μs before injection and maintained for 800μs.

The quadrupoles were also used to 'scrape' the muon beam. Scraping was accomplished through use of passive collimators (copper apertures 9 cm in diameter and 3 mm thick), which were manually rotated into the storage region. By powering the quadrupole plates asymmetrically, the beam was pushed slightly off center, and muons on the edges of the momentum distribution were forced into the collimators. In this way, once the plates were at their full voltage (15μs after T$\emptyset$), the muon distribution was narrower, and the probability that a muon would be lost had been greatly reduced.

3.7.5 Fiber Harp

The fiber harps were designed to give profile information as feedback for tuning injection parameters when first injecting pions into the storage ring. Two sets, consisting of a vertical and horizontal fiber harp, were located at 180°and 270°, for tuning momentum and inflection angle respectively (see Figure 3.6). Each fiber-harp consisted of seven 0.5 mm scintillating fibers separated by 10 cm. The scintillating fibers were joined to clear fibers and then connected to an optical vacuum to air feed-thru. On the other side, a set of clear fibers carried the light signals to 7 independent PMTs. The harps were pneumatically inserted into the storage ring; hence, were a destructive measurement of the beam profile (muons striking the fibers would multiply scatter and be lost).

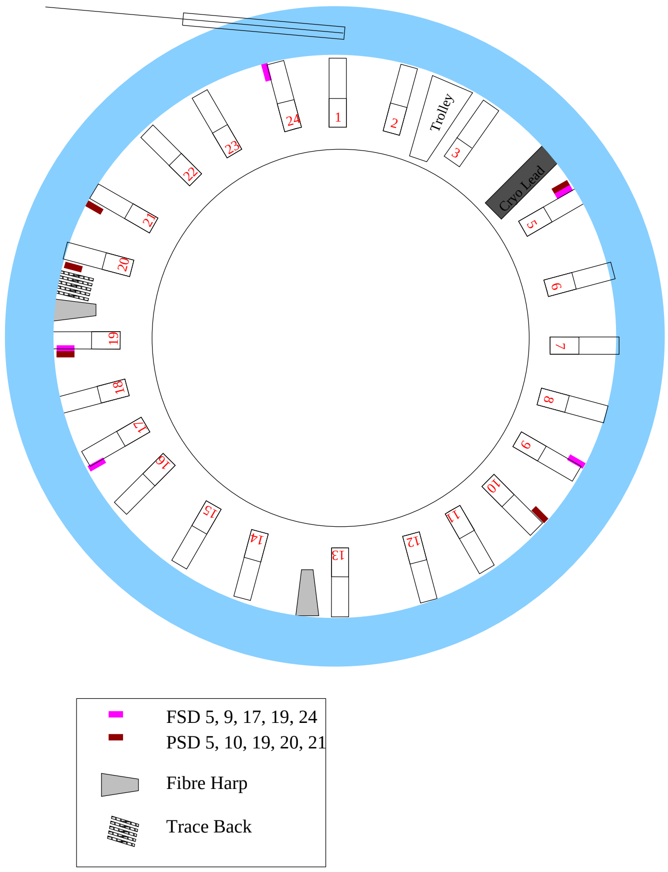

Figure 3.6: The location and numbering of the electron detectors

3.8 Electron Detectors

There were three main types of detectors used in the experiment: electron calorimeters, position sensitive detectors (PSD), and front slab detectors (FSD) (Figure 3.7). For the 1997 run, 22 calorimeters (detectors 2 and 3 were missing), 5 PSDs, and 5 FSDs were placed at the ring positions indicated in Figure 3.6. In addition, there was a set of three wire chambers located just upstream of ring position 20.

3.8.1 Calorimeter

Calorimeters were used to measure the time and energy of the decay electrons. The calorimeters were made of 1 mm plastic scintillating fibers embedded in a lead/antimony

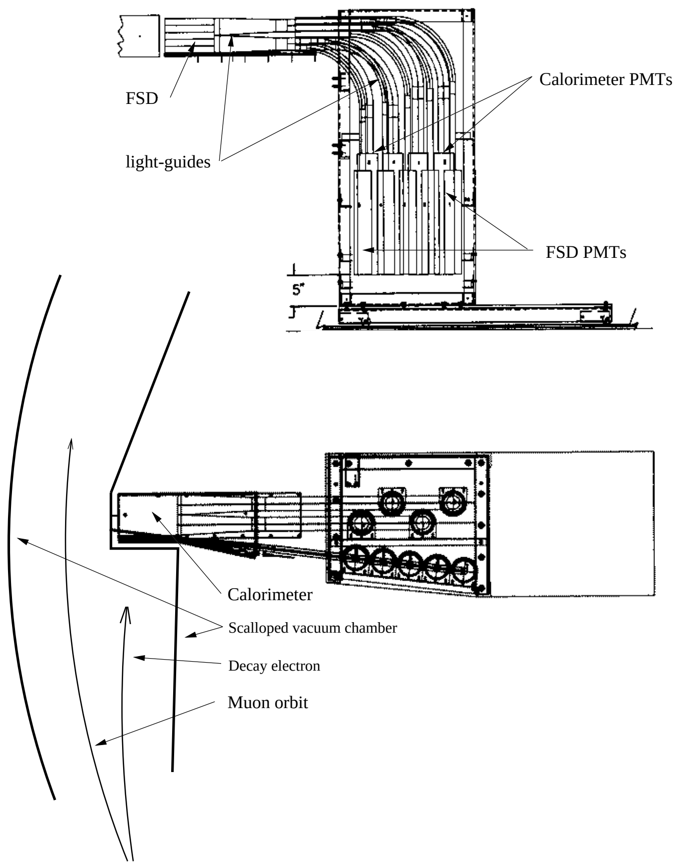

Figure 3.7: A (g-2) detector station.

(6%) matrix (Pb/SCIFI) [33]. The Pb/SCIFI modules were constructed by gluing stretched nets of evenly spaced fibers between grooved lead plates (35% plastic by volume). Each Pb/SCIFI module was 22.5 cm wide × 14 cm high × 15 cm deep and had a radiation length of about 1 cm. These parameters were chosen to minimize the background from low-energy side-entering decay electrons, while maximizing shower containment and light output. The fibers were oriented radially with respect to the storage ring, such that high-energy decay electrons would enter the module nearly perpendicular to the fibers. Half of the modules had boron added to the optical epoxy surrounding the fibers to increase the neutron capture cross-section which, in turn, reduced the die-away time of the delayed flash. To each Pb/SCIFI module was glued four intermediate segments of Lucite[1] light-guide. The intermediate light-guide had a rectangular cross-section (7 cm high $\times$ 7.5 cm deep) that attached to the calorimeter, and reduced to a 2" diameter circular cross-section which attached to final 2" Lucite light-guide. The final light-guides bent through 90°to bring the light to the 2" PMTs. This light pipe arrangement was chosen in order to keep the PMTs out of mid-plane of the magnet where the flash was expected to be most intense. Using the four individual PMTs rather than one large PMT reduced rate-dependent effects which could bias the (g-2) measurement at early times.

All calorimeters were calibrated in the test beam at BNL prior to installation into the (g-2) ring (the calorimeter located at ring position 20 was calibrated using cosmic rays). The calorimeters were calibrated with Kodak 2E 'yellow filters' placed between the final light-guide and PMT of each quadrant. The filters 'flattened' radial calorimeter response by cutting off the shorter (below $\sim$ 430 nm) and more quickly attenuating wavelengths of the scintillator light.

3.8.2 PSD and FSD

The PSD was a scintillating tile fiber hodoscope located on the front face of the calorimeter read out by a multichannel PMT [34]. The PSD was designed to use geometric segmentation (32 vertical tiles and 20 horizontal tiles each tile 7mm in width) to locate the position at which decay electrons entered the calorimeters, as well as reject multiple hits that occurred within a time bin centered on a calorimeter hit. In addition, the PSD was designed to be used to put a limit on the electric dipole moment of the muon (EDM) [35]. The presence of an EDM would have tilted the plane of the spin precession and introduced an up-down wobble to the electron distribution.

The FSD consisted of 5 scintillator slabs 22 cm $\times$ 28 mm wide, oriented horizontally which covered the active area of a calorimeter. Light from the scintillator was guided

[1]DuPont address

through Lucite lightguides to a 1" PMT. The FSDs were designed to use accurate timing (via fast PMTs and read-out electronics) as well as their limited segmentation to measure electron decay times and to aid in multiple-hit rejection.

3.9 PMTs and Gated Bases

The calorimeters used two types of PMTs: 8 calorimeters had Hamamatsu R1828-01 PMTs and 14 had Hamamatsu R3489. The tubes had the same internal structure, but they had bi-alkali and multi-alkali photocathodes respectively. The R3489 had better short-term stability with respect to recovery from an intense light flash due to the lower resistance of the multi-alkali photocathode [36]. Therefore, the calorimeters outfitted with the R3489 PMTs were placed near injection to the ring where the flash was most intense. The FSDs were equipped with Hamamatsu R1355 bi-alkali PMTs, and the PSDs were equipped with Philips XP1723/D1 64 channel PMTs.

A peculiarity of the g-2 experiment is that all detector PMTs needed to be gated-off to protect them from the prompt flash. Gating for the calorimeter and FSD tubes was accomplished by interchanging the voltages on several dynodes on the base, creating reverse bias between switched and adjacent dynodes and reducing gain [37]. On the PSD, reverse bias was created by ac-coupling a voltage pulse into the dynode chain at several locations [34]. The calorimeter and FSD gating scheme was bi-stable (either the 'gated-on' or the 'gated-off' state could be maintained indefinitely); while, the PSD could be safely gated off for a maximum of about 40μs.

3.10 Detector Electronics

The detector read-out electronics was broken up into two basic chains: 9U-VME based electronics and CAMAC based electronics. Figure 3.8 shows the complete cabling diagram for the experiment. The VME electronics consisted of Waveform digitizers (WFD),

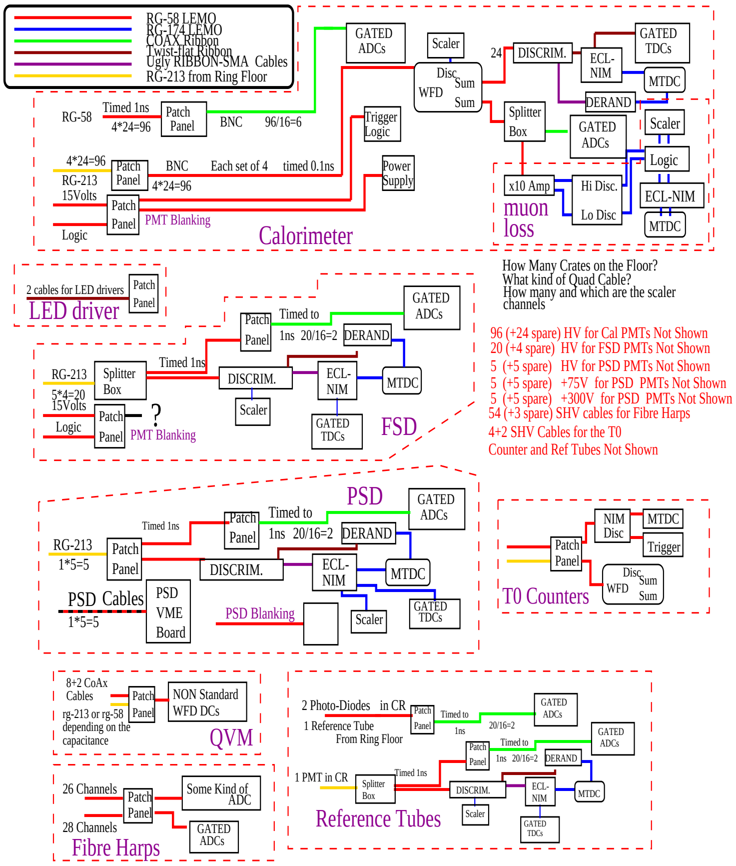

Figure 3.8: Cabling for detector station

multi-hit time to digital converters (MTDC), and special electronics designed to read out the PSD. For calibration, LeCroy CAMAC 2249A analog to digital converters (ADC), and LeCroy 2228 time to digital converters (TDC) were used. Only calorimeter cabling is described, FSD cabling follows similarly. The PSD cabling and read-out electronics is more complicated and the reader is referred to [38].

Calorimeter Cabling

For recording of decay electrons in the calorimeter, a split anode output from the base of each of the quadrants went through RG213 cable which was cut just long enough to make the distance to the control room (100–220 ns). There, the four quadrants were timed-in[2] with short adjustment cables and plugged into a WFD. The WFD summed the four input signals from the quadrants and digitized them. The WFD also provided two copies of the summed signal. One of these was discriminated and used to record the time of the pulse in the MTDC. This input was also fed into a bank of CAMAC scalers, and proved useful for debugging improperly terminated cables (reflections from poor termination would show up as extra pulses in the scalers when pulsing the calibration system).

For calorimeter calibration, the other split anode output from each of the quadrants was sent through RG58 cable to the control room (equal lengths for all detectors) and was fed into LeCroy ADCs used for pulse height calibration with laser and LED signals. The remaining summed calorimeter output from the WFD was also input into the ADCs for comparisons with the individual quadrants. For timing calibration, the discriminated sum signal was used as input to the TDCs.

3.10.1 Clock

We used a Stanford Research Systems (SRS) FS700 to produce a 10 MHz reference. The SRS FS700 received the LORAN-C frequency standard radio signal and used it to stabilize an internal crystal oscillator. The 10MHz was stable to 1×10^{-12} long term, and 1×10^{-10} in the short term[3]. The 10MHz from the SRS FS700 was fanned out and used to stabilize the NMR system's PTS-160 frequency synthesizer (used for magnetic field measurements), as well as the PTS-310 frequency synthesizer (used for the detector electronics, operating at 200MHz). The advantage of this approach was that any fractional drift in the NMR and detector clocks would be the same, thus would cancel in the ratio of ω_a/ω_p [39].

[2] Cables are timed-in by firing calibration laser into the the calorimeter station and then changing adjustment cables (1–10 ns in length) until the laser pulses were within $\sim$1 ns of each other.

[3] See http://www.srsys.com/srsys/html/fs700.html

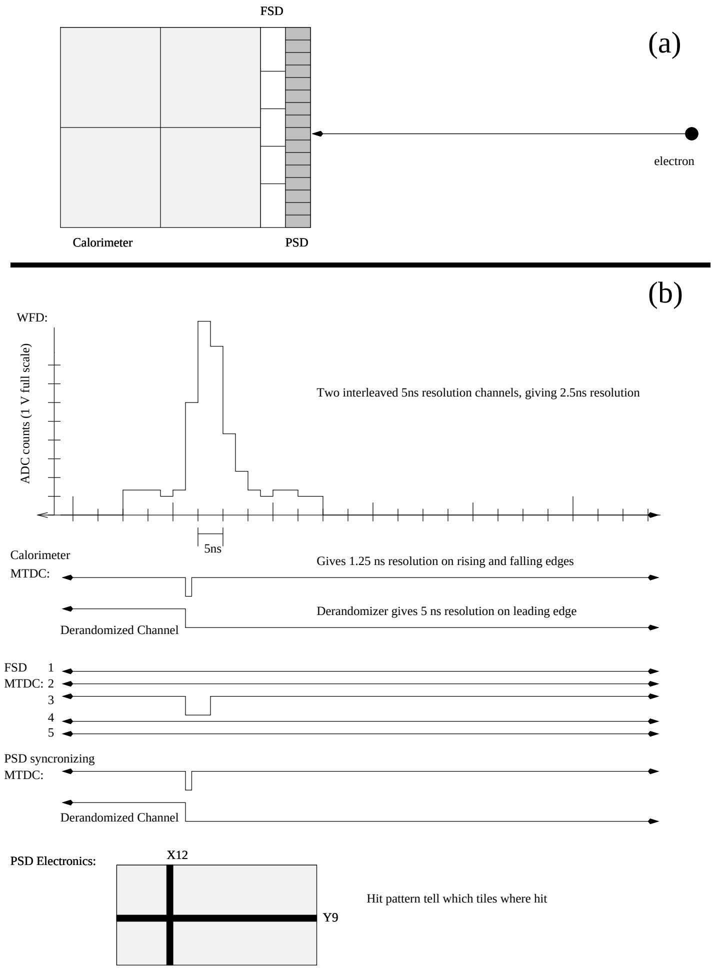

Figure 3.9: An incident electron striking a detector station *(a)* and corresponding VME electronics output *(b)*.

3.10.2 WFD

The WFD was essentially a digital oscilloscope that recorded a trace for each 640μs fill of the experiment [40](Figure 3.9). The digitizer ran at a rate of 400 MHz (2.5 ns between samples), achieving this rate by interleaving two 'phases' (oscilloscope traces) which each sampled at a 200 MHz rate. In order to align the two phases, a marker pulse was input to the WFD at the beginning of each fill. Since there was no data during most of the fill, and because a whole fill could not be recorded at 2.5 ns sampling (due to memory constraints), the digitizers were operated in zero-suppressed mode. In this mode, the digitizers always digitized (no dead-time), but they only wrote to their memory if the input voltage was above a programmable threshold 6.5 ns before its respective 200 MHz clock edge. Data was recorded in a minimum block of 20 ns, so that the minimum number of samples in a pulse was four. The 6.5 ns pre-sample was designed in order to establish a pedestal value for each digitized pulse (the first sample). In zero-suppressed mode, a pulse could be missed if it was over threshold for less than 2.5 ns. Therefore, additional circuitry was designed to 'stretch' the amount of time a pulse was over threshold in order to guarantee full digitization ($\geq$8 samples in each phase).

3.10.3 MTDC and Derandomizer

The MTDC and derandomizer were designed to give timing information for the pulses that was independent of rate. The MTDC registered the time of the leading and trailing edges of the input NIM or ECL level logic pulses at a sampling rate of 800MHz (1.25ns time resolution) and allowed for 27 independent channels of input per MTDC module [41]. The detector signals came at random times relative to the MTDC clock, so any rate dependencies involved in assigning pulses to time bins would directly contribute to the systematic error in ω_a. The principal worry in a TDC is assigning times to pulses which fall near the time boundaries; assigning times in a rate independent manner presents a big challenge. One way around this difficulty is to force the input pulses to come at specific times with respect to bin boundaries (i.e., centerall pulses in a time bin). A derandomizer module was designed which worked as follows: logic signals (minimum width 5ns=1/200MHz) were sent into a J-K flip-flop set in toggle mode and were enabled on one edge of a clock transition. When a discriminator pulse was input, the resulting flip-flop transition occurred synchronously with the clock (common to both MTDC and derandomizer).

3.11 Calibration

Both a light-emitting diode (LED) and a laser system were used to monitor the detector system. The purpose of the laser system was to measure short-term timing shifts and gain stability of the detectors from early to late times, as well as to monitor long-term gain changes of the PMTs. The flight simulator was used to pulse the laser during and between fills and comparisons with the same pulses seen in a reference (isolated from the experiment) were made to monitor any early-to-late timing shifts or gain changes. The LED system provided a backup to the laser and was used to maintain the overall balance between calorimeter quadrants.

3.11.1 Flight Simulator

The flight simulator (FS) was a 32 channel ECL-level programmable pulse generator used to control calibration electronics: It triggered the laser and LED to fire. The input clock (50MHz maximum) determined the output pulse widths (approximately half the clock period). The FS had 32 kbytes worth of 32-bit word memory. Patterns (0's or 1's) were set in the memory through the VME back-plane. Once set, the memory was scanned only after a computer 'scan' signal was sent and an external NIM level hold-off was disabled. A scan clocked the 32 kbytes of data onto the 32 ECL output lines at the clock frequency. At 50 MHz, a complete scan of the memory took 655μs. The outputs were high only when the clock was high and a '1' had been set in the pattern. Thus, the output widths were approximately half of a clock cycle. The FS was clocked at 25MHz (half of its maximum speed) to increase the output pulse widths and the stability.

3.11.2 Laser and LED

The laser system was comprised of a UV laser (337 nm) whose signal was attenuated and split appropriately, providing inputs to the isolated reference and the detector stations.

Laser light was directed through quartz fibers to small Lucite blocks located at the radially most outward end of the calorimeters. The blocks distributed the laser light which stimulated the calorimeter scintillating fiber and produced a signal comparable (slightly narrower) to those produced by decay electrons. Outputs from a reference photodiode (Hamamatsu S3590-01), which saw direct UV light, went into a channel of WFD, ADC, TDC. Since the detectors and the reference saw the same laser pulse, measured timing and gain differences between them were used to map out early-to-late timing and gain shifts of the detectors. Laser light also illuminated each FSD scintillator slab and one channel of the multichannel PMT attached to the PSD. The laser system could trigger at a maximum rate of 50 Hz, so it could be pulsed only once per fill.

The LED system was driven by two types of LED pulser modules. Two modules were 'low-voltage' pulsers [42], designed to drive fast blue[4] LEDs located on the calorimeters and PSDs. The others were 'high-voltage' pulsers, used to drive green[5] LEDs located on the FSDs. The blue LEDs came closer in matching the light spectrum and pulse shape produced by the scintillator, and the low-voltage pulsers were more reliable. Unfortunately, shortage of time precluded retro-fitting the FSD detectors. For each calorimeter, the blue LED was placed between the four lightguides such that it simultaneously illuminated the four PMTs. This setup proved to be a reliable way of maintaining the balance between the calorimeter quadrants to 10–20% [25]. Also, by ramping up the LED signal and measuring the ratio of the width to the mean PMT ADC distribution, the quantum efficiency of the PMTs was roughly characterized. In addition, the LED system was pulsed at rates of up to 5 MHz to simulate decay electrons in bench tests of the entire detector and data acquisition system.

---

[4]NICHIA Chemical Industries, NSPB series (blue)

[5]Radio Shack green LED

3.12 Data Acquisition (DAQ)

The DAQ [43, 44] was a distributed system whose primary purpose was to read data from the electronics and write it to tape as fast as possible. All online monitoring was done only if it did not interfere with data concatenation and tape writing. The hardware distribution for the DAQ is shown in Figure 3.10. The MVME-167 CPU, located in the

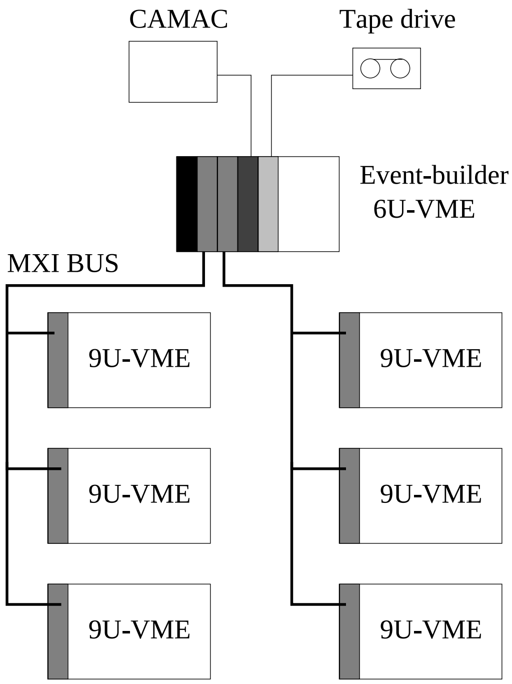

Figure 3.10: Hardware layout for the data acquisition system

'event-builder' 6U VME crate, communicated with the VME based electronics, located in the 9U-crates, over an MXI-bus which was daisy-chained between them. The MVME-167 communicated with CAMAC through a Kinetics 3922 interface located in the 6U-crate. Event building took place as follows: After each of the 8 fills, the CAMAC data was read out and buffered in the memory of the MVME-167. After the eighth fill, the WFD, MTDC, and PSD memory buffers were read out and this data was assembled with the CAMAC data to form an 'event'. After an event was built, it was written to a digital linear tape drive (DLT) through a SCSI interface in the 6U-crate.

Chapter 4

The 1997 (g-2) Run

The (g-2) experiment started its first run in 1997, and took data from April 23 to July 12. The run began with commissioning of the beamline—getting beam from the AGS to the ring and storing muons. After storing muons and observing the first 'wiggle plots' (histograms displaying the (g-2) precession frequency), the focus was set on insuring that all the hardware was operating properly, which proceeded in parallel with maximizing the amount of data collected.

4.1 Commissioning the Beamline

The first milestone was to get the beam from the AGS into the ring and store muons. This was accomplished by running in 'pulse-on-demand' mode. At the push of a button (literally) one of the 8 bunches circulating in the AGS would be extracted. This mode was useful for fine-tuning the beamline magnets, while minimizing the amount of 'wasted beam', giving operators time to analyze the pulse before the next bunch was injected. The first step was to get the extracted proton beam through the U-V beamlines and to the target. This step was accomplished quickly, taking only several hours. The second step was to select the momentum of the secondary beam (58% π^+, 27% p^+, 15% e^+[45]) and steer it into the storage ring. The central momentum of the pions was selected by using two large dipole magnets, located just after the target. Collimator jaws, situated between the two large dipoles, were used to select the width of the momentum distribution. Changing the central momentum also necessitated rescaling the rest of the beamline magnets by the amount of the momentum change, taking into account saturation effects in some of the larger beamline magnets. After the momentum was chosen, steering and focusing magnets were trimmed to center profiles seen in the SWICs and to maximize transmission (the fraction of pions which made it to the ion chamber located just before the entrance to the ring).

According to the commissioning plan, the third step was to look at the profiles of the beam seen in the fiber harps and adjust the inflection angle and momentum to match the profiles, from Monte Carlo[1][46], that corresponded to the maximum number of stored muons. However, when the beamline was finally adjusted to the theoretically optimal tune, *no* profiles where seen in the fiber harps, and *no* decay electrons were detected. At this point it was determined that either the beam was not getting through the inflector channel, or the fiber harps were simply not working. Therefore, the vacuum chamber was bled up to air and two crudely fashioned scintillating detectors (BC7 and BC13) were inserted into the storage region at 80°, and 165°respectively. Each detector consisted of an approximately 1 cm cube of scintillator at the end of a ~7' length of air (~3' straight) and Lucite (~4' L-shaped) light-guide. The scintillator cubes were inserted into the storage region according to the beam Monte Carlo, so that the goal was to maximize their signals. In conjunction with the BC counters, the calorimeter located at ring position 24 was used at reduced gain. At this ring position, the calorimeter would see an initial pulse from injected pions entering the ring followed by a second pulse ~149 ns

[1]The inflection angle most strongly influences the profiles at 90° and 270°, since it determines the center of the pion orbit. The injection momentum most strongly influence the profile at 180°, since it determines the radius of the pion orbit. The inflection angle was determined by how much the beam is bent in the inflector channel and hence determined by the net magnetic field in the inflector. Therefore, the inflection angle was adjusted by changing the inflector current (50 Amps≈4 mrad).

later, associated with the pion bunch going around one full turn and smashing into the inflector. Tuning proceeded by maximizing the second pulse to first pulse ratio. After signals in the counters were maximized, one of the BC counters was placed just upstream of the inflector to get a rough measurement of the transmission through the inflector. The inflector transmission was found to be $\sim 60\%$, and not a problem. After this, the vacuum chamber was pumped down; but still, no decay electrons were detected. It was finally discovered that the injection momentum had been set 2% too low (a 0.6% change would shift the equilibrium orbit by $\sim$4.5 cm in radius and put the center of the beam out of the storage region). This discovery came through the so-called 'Novosibirsk tune' which caused the beam to go snake-like, zig-zagging near the end of the V1 beamline. The Novosibirsk tune was arrived at by maximizing the second to first bump ratio in calorimeter 24, but this time pushing the settings further than was previously thought necessary. With this tune, decay electrons were detected and the first (g-2) wiggle was seen. Subsequent beamline tuning showed that the Novosibirsk tune was effectively selecting a +0.5% higher momentum. Thus, the beamline was re-tuned to +2.5% above the magic momentum and the 'snake' was straightened out (measurements made at the end of the run showed that the momentum of pions which made it through the inflector was indeed +0.5% above the magic momentum; therefore, the +2.5% momentum setting of the beamline actually corresponded to a +0.5% momentum selection). From then to the end of the run, beam tuning continued with small but steady increases in decay electron yield. In the end, the calorimeters themselves were used to count the number of decay electrons, and this guided beam tuning.

4.2 Problems Encountered

There were three major problems that adversely effected the data used in the analysis: AGS trickle, narrow pulses, and WFD inefficiency (listed in order of increasing seriousness). The first two problems were detected during the run, but the WFD inefficiency was masked by the narrow pulse problem, and not discovered until after the run was completed.

4.2.1 AGS Trickle

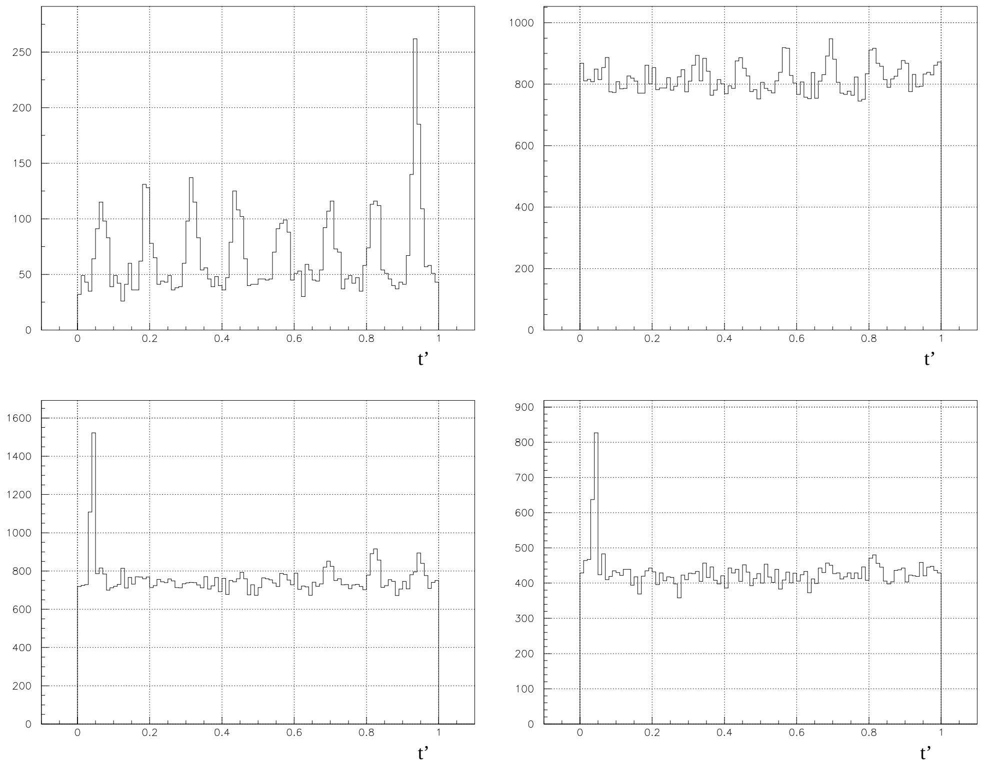

Figure 4.1: Several different modes of AGS trickle: The plots are obtained through correlation, by 'MOD'-ing the entire WFD trace by the AGS period—the 2694 ns it takes for a proton bunch to go around the AGS ring.

Protons from the AGS would leak through the extraction point due to miss-timing of the extraction bump (the current pulse in the extraction magnet) with respect to the proton bunch. This was referred to as AGS trickle. It showed up first in the on-line histograms as an unknown 'blob' $\sim 120\mu s$ after injection. Soon after, in a Fourier spectrum, it showed up as a peak at 370 kHz. And finally, by 'MOD-ing' the WFD time axis by the AGS period (2694 ns), the substructure of the 8 bunches, separated by 337 ns, was observed. Feedback of this discovery to AGS main control allowed them to re-tune the extraction bump and eliminate the trickle. Offline, any run that showed AGS trickle was eliminated from the (g-2) analysis. Figure 4.1 shows the AGS trickle with the 337 ns substructure as observed in one of the calorimeters[28].

4.2.2 Narrow Pulses

Narrow pulses were non-electron pulses detected by the calorimeters that were narrower than electron pulses (narrow$\sim$3.1 ns, electron$\sim$5 ns) and were produced as follows: The sea of neutrons produced in the flash would thermalize in surrounding concrete and steel and be absorbed by the hydrogen in the calorimeters and Lucite lightguides. Induced γ rays (2.2 MeV), or resulting Compton electrons (1.3 MeV), would produce Čerenkov light in the light-guides or the PMT glass.

Narrow pulses were first discovered when looking at plots of pulse height versus pulse area for detected pulses. Figure 4.2 shows a typical pulse height versus pulse area plot for one of the detectors. The narrow pulse time spectrum had a power-law shape, which is evident on the log(counts) versus log(time) plot seen in Figure 4.3. After finding them, further investigation showed that the narrow pulses were responsible for more than 80% of the data volume[47] and that narrow pulses that were below threshold and not detected, would not effect the (g-2) frequency[48]. Therefore, the thresholds on the WFDs were raised to 1 GeV in order to minimize the amount of noise that was written to tape (see Figure 4.2). Only electrons with energies $\geq$1.6 GeV would be used in offline frequency analysis, so this threshold setting seemed to be safe.

In addition to raising thresholds on the WFDs, an effort was made to 'tag' narrow pulses using the inherent coincidence provided by the four quadrants of the calorimeters. Unlike decay electrons, which would produce a front-back coincidence between quadrants of a calorimeter, narrow pulses would not.

WFD discriminator bits, intended to identify quadrants that were over a programmed threshold level, proved to be of little use in identifying narrow pulses. The WFD was

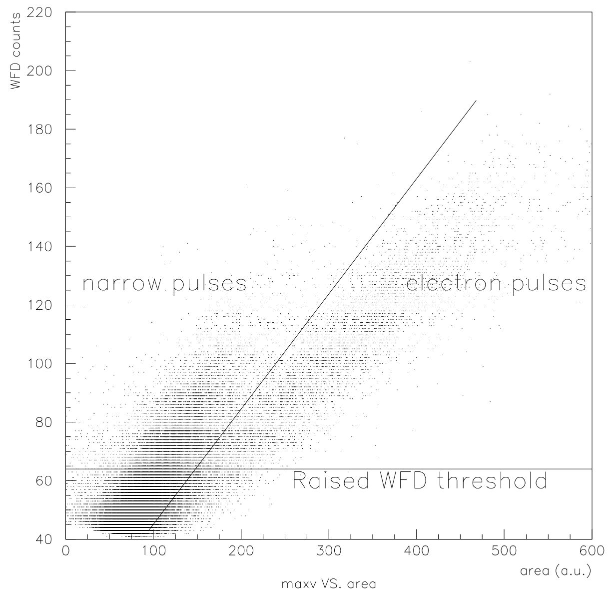

Figure 4.2: A scatter plot of pulse height (maxv) versus pulse area for detected pulses. The two regions representing narrow and electron pulses are indicated. The horizontal line represents the level of the WFD threshold after it was raised to reduce the number of narrow pulses (~1 GeV).

triggered to digitize on the 'OR' of the individual channels with the SUM of the four channels. If thresholds on the individual channels where set low enough so that the discriminator bits would fire and be recorded, then the effective trigger threshold for the sum would have been approximately 2 times lower, and the WFDs would have filled up with even more flash and narrow pulses.

Since the WFDs did not prove useful in tagging electrons, 'C-tags' were set up to tag electron hits. A C-tag required a two-fold coincidence between any of the four calorimeter quadrants. C-tags were implemented on detector stations without FSDs, since they used FSD signal cables to bring the four quadrant dynode signals from the PMT bases to the control room. In the control room, the dynode outputs were

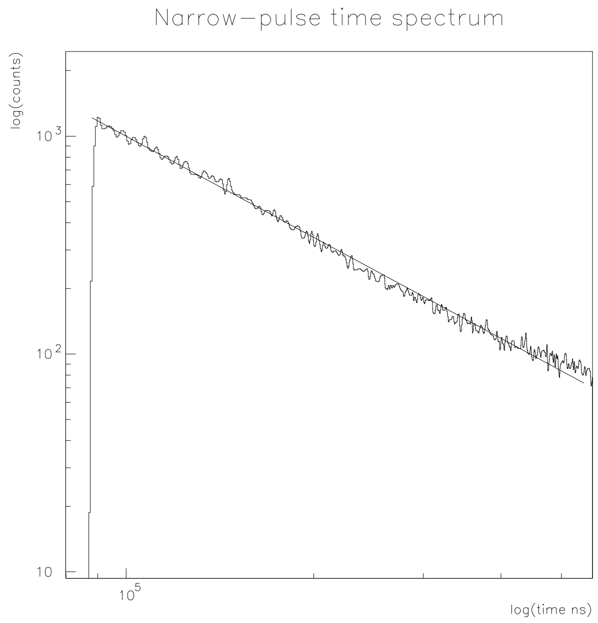

Figure 4.3: log(counts) versus log(time) for the narrow pulse time spectrum. The linear shape indicates a power-law relation.

inverted, discriminated and used to form the coincidence. Each C-tag was input to an MTDC and scaler channel. In the end, sophisticated pulse fitting algorithms proved to be more useful in rejecting narrow-pulses than the C-tags were; C-tags could not be implemented on all stations and the haste in which they had to be constructed led to secondary problems which ultimately precluded their use in rejecting narrow pulses for the (g-2) analysis.

Though raising thresholds and tagging electrons helped with the narrow pulse problem, it did not eliminate it. Extensive attempts at shielding detectors from neutrons using a host of neutron absorbing materials was fruitless—the neutrons were too pervasive and narrow pulses persisted.

One oddity was the varying level of narrow pulse contamination between detectors.

It was expected that those detectors near injection into the ring would have had more narrow pulses, which was in general the case; however, there were adjacent detectors far from injection (e.g., 16 and 17) that had huge differences in their narrow pulse fractions. A correlation was made between the number of narrow pulses and high voltage (HV) applied to the PMT. It seemed that detectors with HV settings greater than 2000 V had substantially more narrow pulses. This prompted investigations into micro-corona (small high voltage breakdown) as the cause for the narrow pulses; however, this was not the problem. Eventually, the yellow filters were removed on one of the calorimeters. The filters were in place to make the calorimeter energy response more uniform with respect to the radial position of an incident decay electron. Unfortunately, as a by-product of using the yellow-filters, the number of photons that make it to the PMT was reduced by about a factor of two. Hence, it was expected that yellow filter removal should increase the relative size of an electron pulse to that of a narrow pulse, since the high voltage applied to the PMT could be reduced. Figure 4.4 shows the distribution of narrow pulses and electron pulses before and after yellow filter removal. Removing the yellow filters greatly reduced the narrow pulse fraction. At the next break in the run, yellow filters on detectors with large fractions of narrow pulses were removed.

After yellow filter removal, the detector system was left basically untouched. It was decided that the remaining narrow pulses would have to be rejected offline, and for the rest of the run, focus shifted to maximizing the number of detected decay electrons.

WFD Inefficiency

WFD inefficiency was the missing or under-sampling of input pulses that were over the set voltage level threshold. The WFDs were inefficient because input pulses were not over threshold long enough to trigger the pulse-stretching circuitry which would have insured full digitization.

WFD inefficiency was not detected until after the run because it was masked by the

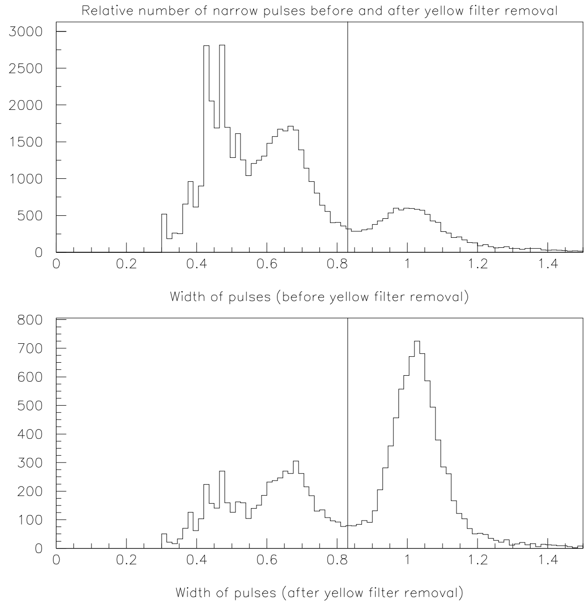

Figure 4.4: Width of the fitted pulses for detector 24 before and after yellow filter removal. A width of '1' corresponds width of an average electron pulse. The fraction of narrow pulses (left of the vertical line) has been reduced from 80% to 40% of the total number of pulses.

narrow pulse problem. Specifically, under-sampled pulses seen in the online histograms were written off as narrow pulses. In addition, the discrepancy between measured and expected values of the muon lifetime, was also attributed to narrow pulse contamination.

Narrow pulses not only masked the WFD inefficiency, they also indirectly created the problem. Analysis on runs taken before the threshold change showed that at the lower threshold, the measured muon lifetime matched the expected muon lifetime. Thus, raising the WFD thresholds to reduce the fraction of narrow pulses created the inefficiency problem.

WFD inefficiency would not have been a problem for analyzing the lifetime or ω_a if it had not changed during a fill. Unfortunately, this was not the case. The changing

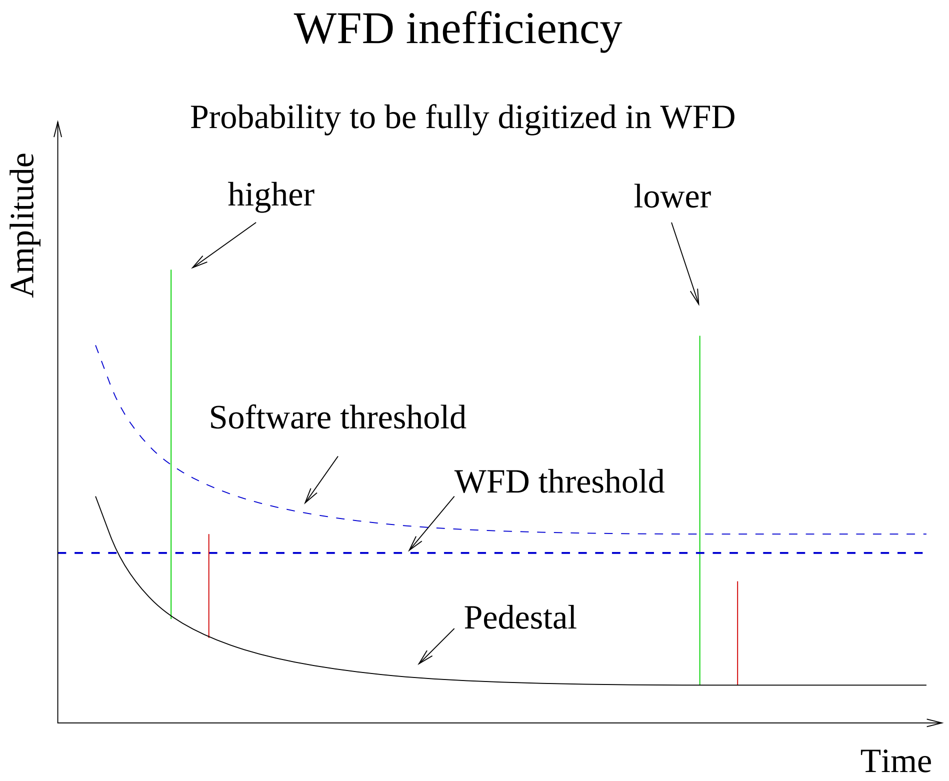

Figure 4.5: A schematic of a pulse on the pedestal at early and late times. A pulse at early times is over the WFD threshold longer so the probability to be fully digitized is higher.

pedestal in the WFDs changed the effective thresholds for digitization and made a lifetime measurement impossible (Figure 4.5). Muons 'lost' from inefficiency are directly coupled to the lifetime measurement, and could not be reliably simulated. On the other hand, inefficiency only indirectly contributed to a measurement of ω_a. Appendix A describes the Ratio Method: a prescription for analyzing ω_a which minimizes the contribution from WFD inefficiency.

The WFD inefficiency caused the average asymmetry to change with time. Since average energy of fully digitized pulses increased during a fill, the asymmetry also increased (higher energy decay electrons have higher asymmetry). This caused further complications when fitting the frequency.

4.2.3 Maximizing the Statistics

Maximizing the number of detected decay electrons meant moving gate-on times as close to T∅ as possible while finding the optimum between two competing effects: (1) The exponential increase in the number of decay electrons associated with earlier gate-on times. (2) The loss of statistics suffered from overflowing WFD memory buffers (each overflow event—8 fills—had to be thrown out of the offline analysis). Overflow events most often occurred when the pedestal level in the WFD was greater than the threshold for digitization. In this case, the WFDs would digitize continuously (400 MHz) and quickly overflow their memory buffers.

An unfortunate outcome of the above maximization, was that it made offline analysis more difficult. In order to take advantage of the statistics gained, the decay electron spectra for each of the different gating periods had to be analyzed separately. Otherwise, there would be a 'kink' in the resulting decay spectrum and latest of the gate-on times would have to be used (see Figure 4.6).

4.3 Data Used in Analysis

Table 4.1 gives a summary of the 1997 run conditions. Since each detector represents an independent (g-2) experiment and backgrounds and pulse-parameter are different for each detector (different energy scales and pulse-shapes), there is a natural division of the data on a detector by detector basis. In addition, there is another natural division into data collection periods. The different periods represent changes in the experimental setup. From table 4.1, periods 1–3 are used in the analysis. Changes made between these periods were: removal of yellow filters from some of the detectors and changing the gate-on times for the detectors—the difference between periods 1,2 and 2,3 respectively. Removal of the yellow filters represented a 'fundamental' change in the setup: the percentage of narrow pulses contaminating the data was much greater before removal

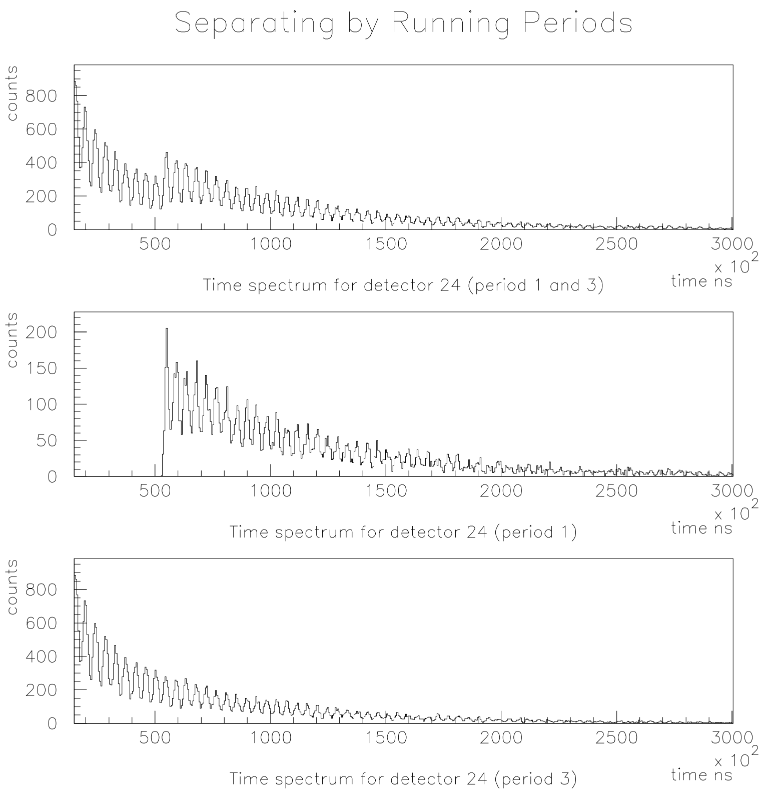

Figure 4.6: An example of a single detector with periods of different gating summed together (top) and separated out (following).

and PMT high voltage was necessarily higher. On the other hand, moving the gate-on times earlier did not 'fundamentally' change the setup, it simply allowed earlier start times to be used for the fits. With these considerations, 20 detectors[2] for each of the three periods were analyzed, for a total of 60 independent data groups.

[2]Detector 4 was excluded since it had *enormous* background—it caught a large portion of the injected pion beam. Detector 15 was excluded because had a poorly terminated inputs to the WFD which caused reflections.

Table 4.1: Summary of the 1997 running conditions: Periods 1–3 are used in the analysis of a_μ .

Period	Date	Run	description
	4/23	—	Begin commissioning beamline; single-bunch extraction
	5/08	405	Novosibirsk tune; first (g-2) signal; start 8-bunch extraction
	5/08	405	Beamline re-tuned to 'magic' momentum +2.5%
			Narrow pulses discovered
	6/08	770	WFD thresholds raised
			AGS trickle discovered
1	6/29	958	AGS trickle fixed
2	7/04	1021	Yellow filters removed from 1, 4, 5, 6, 7, 9, 10, 11, 22, 24; gate-on times changed
3	7/08	1080	Gate-on times moved earlier
	7/11	1150	Injection studies
	7/12	1175	End of 1997 run

Chapter 5

Analysis

Recall from chapter 2 that this experiment measures the ratio R (repeated here for convenience)

$$R = \frac{\omega_a}{\omega_p} = \frac{f_a}{f_p} \ , \tag{5.1}$$

where f_p is the proton NMR frequency, the measure of our magnetic field. Consequently, there are two basic parts of the analysis: extraction of f_a by fitting the decay spectrum and measuring the magnetic field in terms of f_p through NMR measurements.

5.1 Determining f_a

Data written to tape was processed through *G2off*[49]. *G2off* produced a general-purpose n-tuple[1] filled with all the relevant information for each of the ~1 hour data runs. It also applied a pulse fitting algorithm to the WFD data using fit parameters to characterize the pulses. In a second pass through the data, many general-purpose n-tuples were reduced and split to make individual detector n-tuples. The detector n-tuples contained the subset of information from the general-purpose n-tuples required

[1] An n-tuple is a data structure used in PAW[50] that allows easy manipulation of the data elements—think of it as a spread-sheet.

for analysis of f_a. During this second pass, calibration (laser) pulses were removed and poor AGS fills with low values in the ion chamber were excluded. Finally, pulse selection criteria (cuts) were applied to the detector n-tuples and final time spectra histograms for each of the 60 data groups were filled and fit using the Ratio method of appendix A to extract f_a[2].

5.1.1 Pulse Finding and Fitting

The object of fitting WFD traces or 'pulses' to a parameterized form was to assign an energy and time for each decay electron in a way that introduced *no* systematic shift, from early to late times, during the fill (i.e., the fitted time and energy of a pulse should not depend on when it came in the fill). The unexpected narrow-pulse background and WFD inefficiency complicated these assignments. The narrow-pulse background meant, that in addition to a time and energy assignment, electrons had to be characterized for separation from the background. WFD inefficiency made this separation even more difficult because many recorded pulses were under sampled (4-,8-, and 12-samples) and less information was available for the separation process. The method and description for accomplishing these goals is described below.

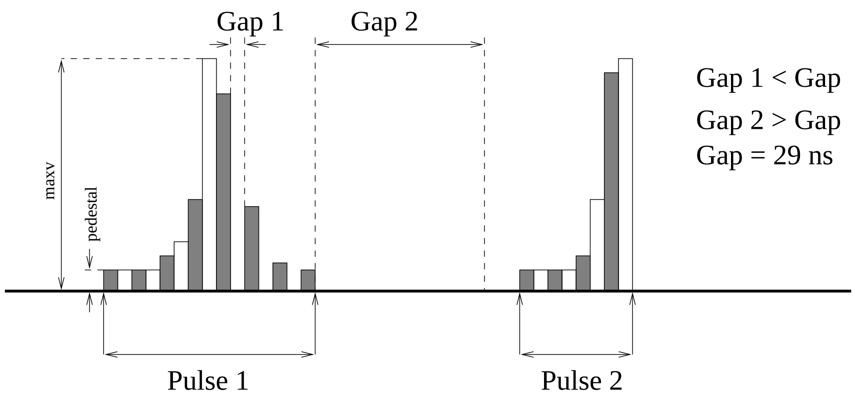

Figure 5.1: schematic of DEFNA pulse finding algorithm.

[2]The 'official' (g-2) analysis used an 8-parameter fitting function. Comparison between the Ratio method result and the 8-parameter result will be made in chapter 7.

The WFD data record was searched for pulses using the DEFNA algorithm in *G2off*. The DEFNA algorithm simply looked for gaps in the WFD time record to mark the beginning and end of pulses. To account for the possibility of a missing phase in a pulse (without defining a new pulse), only a gap in the time record $\geq$30 ns signified that a new pulse was starting (see Figure 5.1). Up to 48 samples were passed to the fitting subroutine, from the start to the stop of a pulse. Pulses were fit if: the number of samples was between 4 and 48, the maximum sample in the pedestal subtracted pulse was greater than 30 WFD counts, and the maximum sample was not the last sample. Figure 5.2 shows the different types of under-sampled pulses and indicates whether or not they were fit.

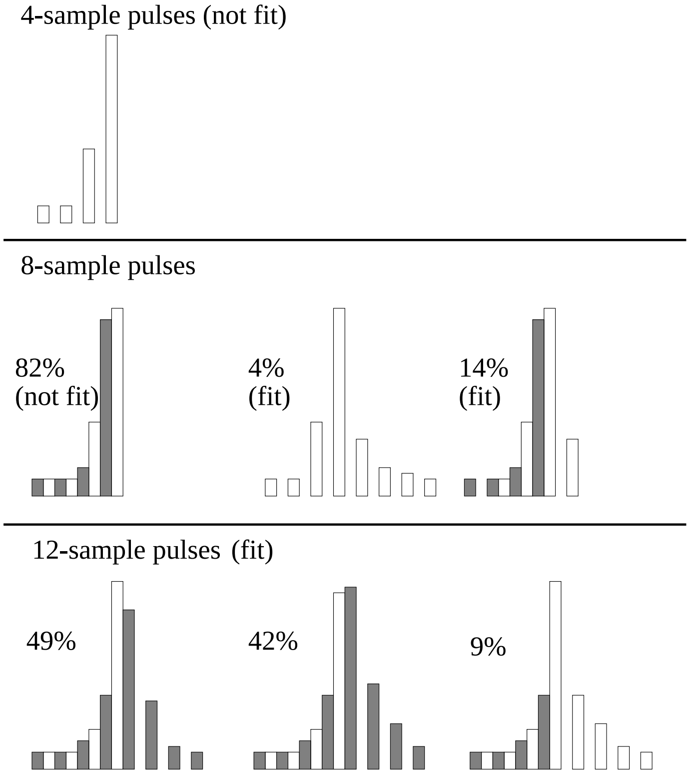

Figure 5.2: Typical 4-, 8-, and 12-sample pulses.

The pulse-shape function was determined through an iterative method (see Figure 5.3). First, a set of 1000 or so fully digitized pulses were fit with the asymmetric Gaussian

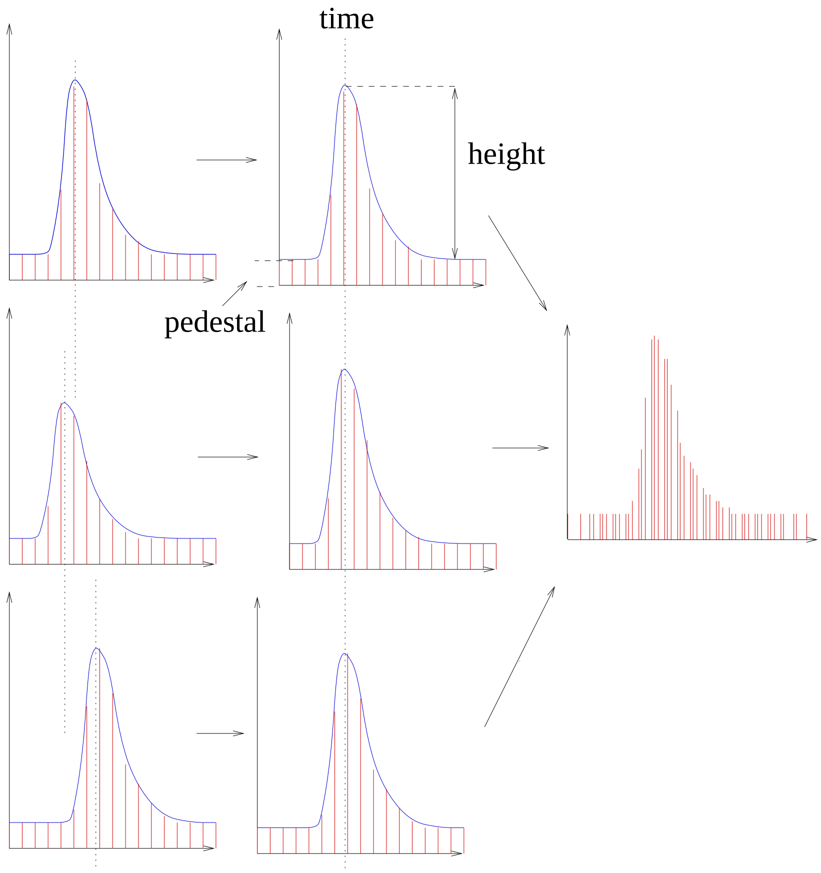

Figure 5.3: Obtaining an average pulse shape.

form

$$V_1(t) \quad = \quad P_1 + P_2 \cdot \exp\left\{-\ln^2\left[1 - \frac{(t-P_3)\cdot\eta}{P_4}\right]/2\sigma_0^2\right\}$$

$$\sigma_0 \quad = \quad \frac{\ln(\eta\sqrt{2\ln 2} + \sqrt{1+\eta^2\cdot 2\ln 2})}{\sqrt{2\ln 2}} \ ,$$

where,

$$P_1 = pedestal,\ P_2 = pulse\ height,\ P_3 = time,\ P_4 = width\ ,$$

establishing a value of η=-0.4 from the average. The next step was to construct an average pulse shape for each detector (before and after removing yellow filters). The function V_1 (η fixed) was fit to each group of fully-digitized pulses. Fit pulses were aligned according to their fit time (P_3=20) and normalized with respect to their pulse height (P_2=200) and pedestal (P_1=10) before averaging. After the average pulse shape had been constructed, it was fit with a 10-parameter function, and the resulting 10 parameters were fixed. This fixed, average, normalized, pulse shape was then scaled and shifted to fit individual pulses. Thus, the fitting function had the form

$$V_2(t) = P_1 + P_2 \cdot \mathcal{F}([t - P_3] \cdot P_4) \ ,$$

where $\mathcal{F}$ represents the fixed 10-parameter function. From here this process could be

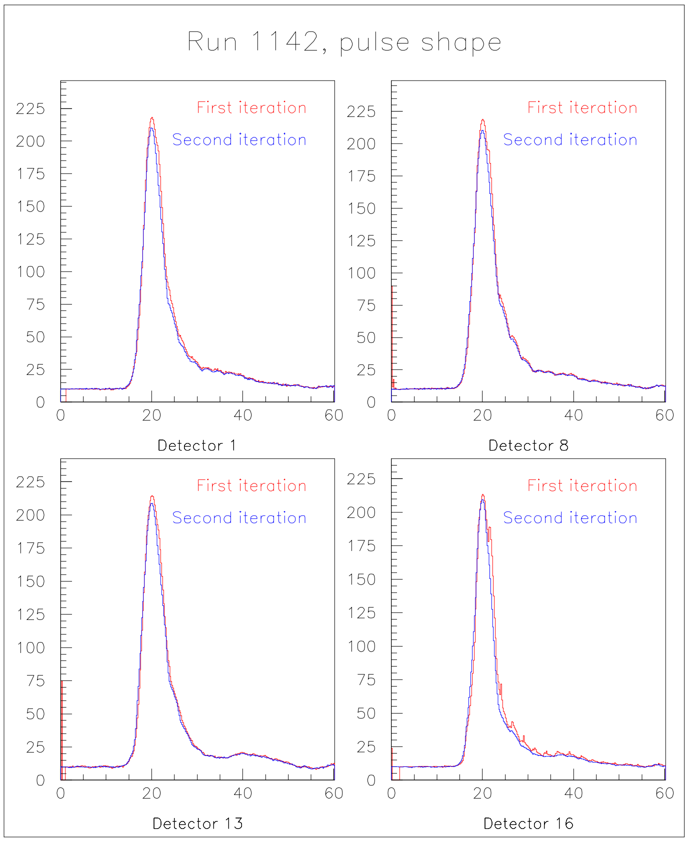

Figure 5.4: Average pulse shapes for several detectors after first and second iteration of alignment and normalization.

repeated using the newly defined 10-parameter function for fitting individual pulses and establishing a new average pulse shape. Figure 5.4 displays average pulse shapes after the first and second iteration of this process. With the exception of detector 16, only one iteration was necessary to establish an average pulse shape that was stable with respect to further iterations.

5.1.2 Filling the Decay Spectra Histograms

A simple cut on pulse width, as could be made in Figure 4.4, was not enough to minimize the amount of narrow-pulse contamination for all of the detectors. Therefore, pulses that were fit, were used to fill 40 fitted pulse height versus pulse width contour histograms: one for every active calorimeter both before and after yellow filter removal. Graphical cuts were applied to separate electrons from the narrow pulses, and the percentage of narrow-pulse contamination was estimated. Figure 5.5 shows this contour plot for detector 14, which had a narrow-pulse region that was easily separated. The narrow

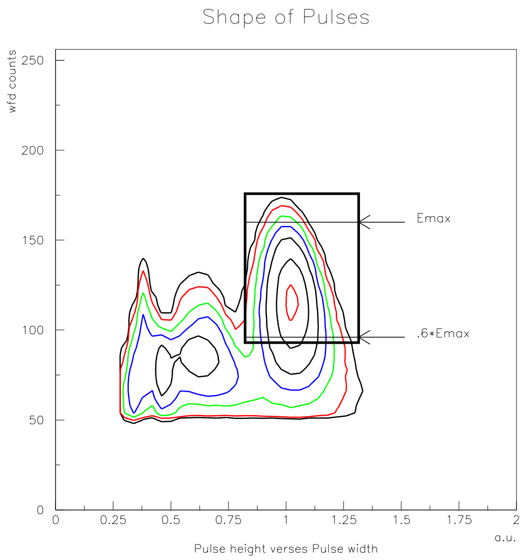

Figure 5.5: A contour plot of pulse height versus pulse width for detector 14. The contours, from outside to inside, represent levels of 1, 2, 5, 10, 20, 50, and 90% of the peak of the distribution within the 'box'. Pulses within the 'box', and with WFD pulse heights greater than 0.6*EMAX were used to fill time spectra histograms.

pulses appear in the lower left, and the electron pulses appear in the middle right. EMAX represents the endpoint of the pulse height spectrum (3.1 GeV)[51]. Only pulses within the 'box' and with pulse height (maxv) greater than 0.6*EMAX (~1.9 GeV) were used to fill decay-spectra histograms. The 0.6*EMAX energy threshold represented an optimization between competing deleterious effects: A lower energy threshold meant increased narrow-pulse contamination, a greater change in efficiency and asymmetry with time, and an overall reduction in the average asymmetry. A higher threshold meant a reduction in the number of electrons.

Decay-spectra histograms were created with one thousand 545.75 ns bins and ran from 15000–560750 ns as measured from T∅ . When they were filled, the time of a pulse, as determined by the pulse fitting, was scaled by the magnetic field for that particular data run. Namely, the time used for filling

$$t = t_{fit} \cdot [1 + B(run)].$$

In this way, all decay electrons saw the 'same' magnetic field, and the results over the different data groups could be directly compared. The magnetic field used for the scaling is shown versus run number in Figure 5.6. The '0' on the vertical axis corresponded to a magnetic field of 61.78850 MHz and represented the average magnetic field for the data run.

5.1.3 Start and Stop times for Fit

Before decay spectra could be fit, start-times (tstart) and stop-times (tstop) for the fits had to be determined. The earliest tstart for a fit was determined using the *latest* value satisfying the following criteria:

(1) To keep systematic shifts in the fit frequency < 1 ppm (caused by the changing pedestal and consequent digitization inefficiency), at tstart, the ratio of the second order to first order terms in Equation (A.9)

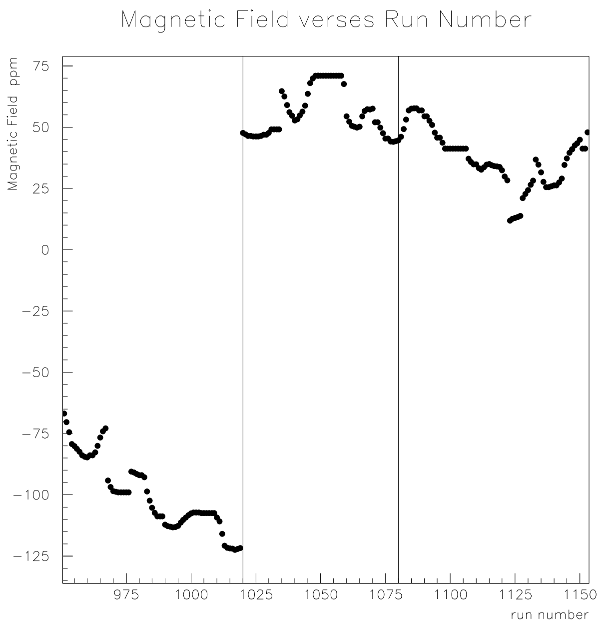

Figure 5.6: The magnetic field versus run number. The field values are referenced to 61.78850 MHz (the '0' on the graph) and are in ppm. The vertical lines delimit the three different periods used in the analysis.

should be less than $\frac{1}{40}$. Equation (A.9) defines an upper limit for the magnitude of this shift based on systematic studies in Chapter 6 (i.e., we choose to start the fits when this systematic shift will be < 1 ppm).

(2) To keep shifts associated with non-fit pulses (number of samples greater than 48) < 1 ppm, tstart should be such that the fraction of pulses with greater than 48 samples in a bin is $< 0.5\%$. Recall that the pulses are fit only if the number of samples is less than 48 samples. These non-fit pulses can create a discontinuity in the decay spectra at early times, when legitimate pulses are thrown out because they are riding on the flash.

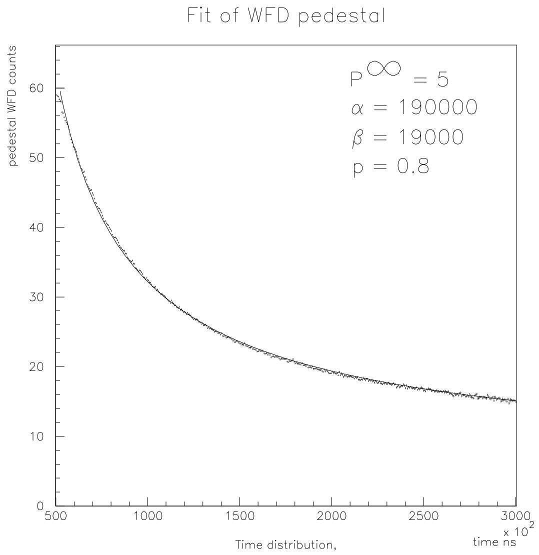

Figure 5.7: An example of a pedestal fit used for meeting criteria (1). The pedestal fit is superimposed on the data.

The criteria in (1) was met by fitting the pedestal with the power-law function

$$Ped(t) = P_\infty + \frac{\alpha}{(t-\beta)^p} \ ,$$

to each of the time spectra, and using the fit-parameters P_∞, α, β, and p to calculate the minimum value for tstart. Figure 5.7 shows a fit of the pedestal for detector one for period three. 'tstop' was established fitting decay spectra while bin errors were still Gaussian (i.e., tstop was defined when the average number of counts in 8 adjacent bins was < 5).

5.1.4 Fitting the Data

With tstart and tstop established, the 60 time spectra histograms were fit using the Ratio function in Equation (A.14), written here in terms of its fit parameters P_i

$$R(t) \;=\; \overbrace{\{P_1 + P_2 t\}}^{Asymmetry} \cos\left(2\pi \overbrace{[f_0 - P_3]}^{frequency}\, t + \overbrace{P_4}^{phase}\right)$$

where P_3 (Δf_a) is the difference in the fit frequency from $f_0 \equiv 2.291 \times 10^{-4}$MHz, and P_2 allows for the asymmetry to change with time. Figure 5.8 shows Δf_a from the fit

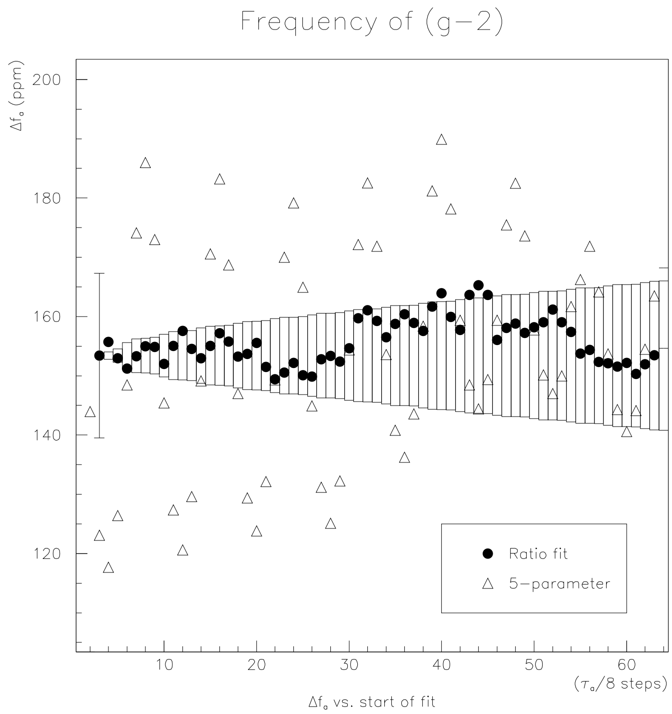

Figure 5.8: Δf_a versus start of the fit. Each point represents 60 fits. The fits are started on the same part of the (g-2) phase and tstart is incremented by one histogram bin ($\tau_a/8$=545.75 ns). The first point is Δf_a = 153.4 ±13.9 ppm, and has the error bar plotted. The envelope shows how much Δf_a can change due to the loss of statistics which accompanies a later tstart. The 5-parameter fit is overlaid for comparison.

for the 60 time spectra histograms as a function of the start of the fit. Because less and less data is fit with increasing tstart, the value of Δf_a can change with the start time of the fit. The envelope (ENV) delimits the *allowable* change, and is defined

$$ENV_i = \sqrt{[\delta(\Delta f_a)_i]^2 - [\delta(\Delta f_a)_1]^2}$$

where $\delta(\Delta f_a)_i$ represents the statistical error of Δf_a at the i^{th} point and $\delta(\Delta f_a)_1$ represents the error on the first point (earliest tstart). With the earliest tstart chosen as described above, there is no evidence of a systematic *shift* in Δf_a associated with tstart. However, a small *oscillation* of Δf_a in time can be seen. This oscillation is due to 'phase-pulling'. Choosing the value of Δf_a at the middle of the oscillation (zero crossing) will give the *true* value (section 6.2.1 will show that Δf_a oscillates around its *true* value). The fit using the expected decay spectrum function called the 5-parameter fit (Equation (2.6), is overlaid for comparison. The Ratio fit greatly reduces the magnitude of the phase-pulling oscillation, allowing the zero crossing to be determined more accurately.

Both the mean and width of the χ^2 distribution support the validity of the fits. Figures 5.9 show the χ^2 of the 60 fits at the first point in Figure 5.8. The $<\chi^2>$=1.015 from Figure 5.9 corresponds to a confidence level of 38% (the average number of degrees of freedom was $<ndf>$=574). The width of the χ^2 distribution, RMS=0.063 from the plot, agrees with the expected width: $\sqrt{\frac{2}{574}} = 0.059$.

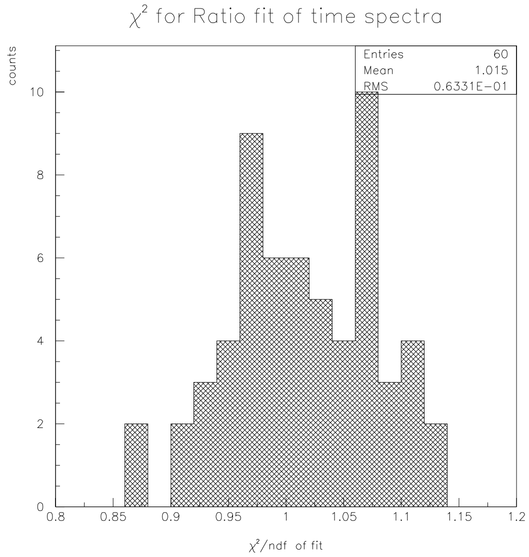

Figure 5.9: The χ^2 from the 60 time spectra fits

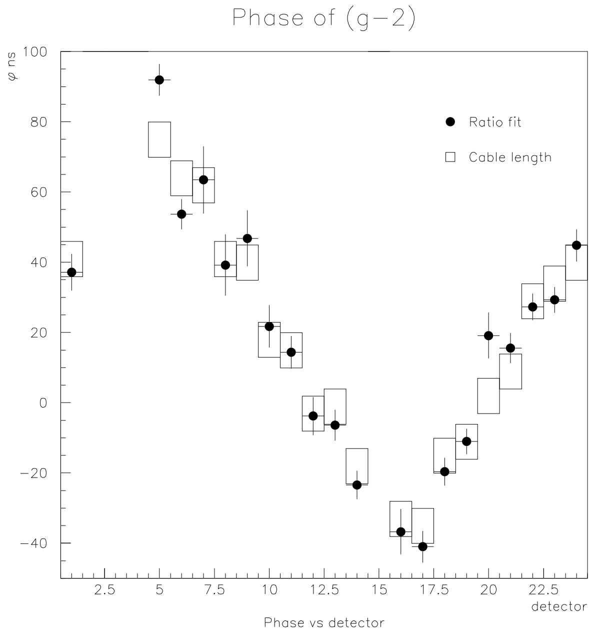

Figure 5.10: The phase of (g-2) spectra versus detector for the three periods of analysis. The phase is written in nanoseconds. Both the phase extracted from the fit and from a measurement of the relative detector timing with the LEDs are plotted. The error on the LED measurement is estimated to be ± 5 ns and is due to uncertainty in the 'firing' time of the LEDs.

The phase of the (g-2) spectra also indicate that the fits are correct. Figure 5.10 shows the phase extracted from the fit and from a measurement of the relative detector timing with the LEDs. The phase is different between detectors because the cable lengths were not the same. Since the phase and frequency are strongly correlated (section 6.1), agreement between the two separate measurements help confirm the value of Δf_a.

For completeness, the asymmetry from the fit time spectra is shown in Figure 5.11. Since the Ratio fit eliminates the muon lifetime as a fit parameter, we can use Equation (2.7) to calculate the average lifetime. With a total of 10.07 million decay electrons in the spectra and an average asymmetry of 0.39 (Figure 5.11), the calculated dilated muon lifetime is 57.1μs compared to the expected 64.4μs. Of course the WFD inefficiency

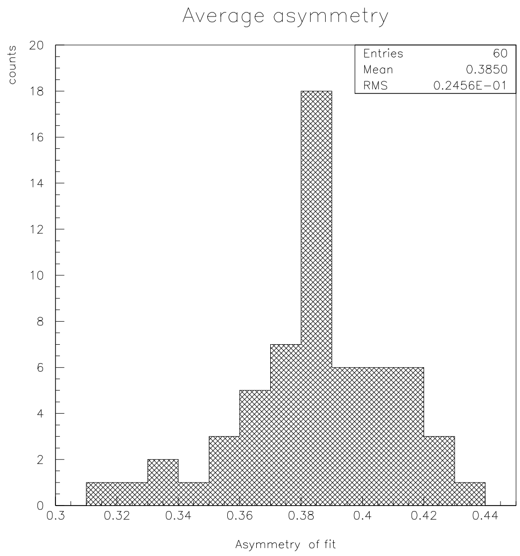

Figure 5.11: The asymmetry from the 60 time spectra fits

makes this a fairly meaningless calculation; nevertheless, its a further (rough) check of statistically consistency of the fits. Conversely, it is more useful for estimating the number of electrons that were lost due to the WFD efficiency. Assuming a dilated lifetime as expected above and the rest of the variables the same, about 20% fewer electrons would have been necessary to reach the same level of statistical precision.

5.2 Average Absolute Magnetic Field

The average absolute magnetic field seen by the muons is found by measuring the average magnetic field weighted by the measured muon distribution[52]. Using the field monitoring system described in section 3.7.2, for the 1997 run, the absolute magnetic field was known to a precision of 0.9 ppm. Figure 5.12 shows the average magnetic field cross-section seen in the storage region averaged over azimuth.

After the pion bunch is injected into the ring and the muons are stored, the muon

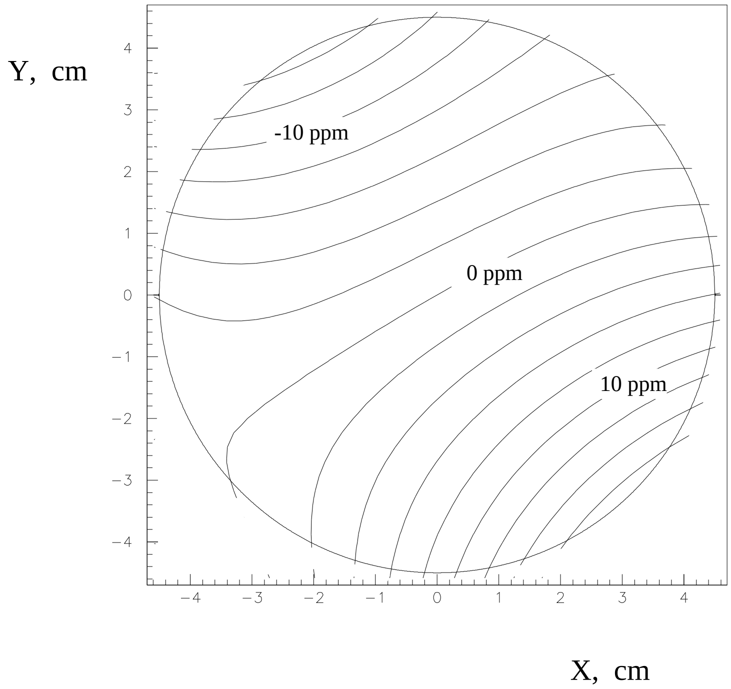

Figure 5.12: The azimuth averaged magnetic field profile in the storage region. The contour lines are in steps of 2 ppm. The multipole content in ppm is: Normal- quadrupole 6.5, sextupole 1.7, octupole -2.4, decupole 0.2; Skew- quadrupole 11.4, sextupole 2.3, octupole 1.1, decupole -0.2.

bunch begins to spread out in time. The muons spread at a rate related to the momentum spread which was $\Delta p/p \approx 0.5\%$. At times just after injection (12μs), the decay signal, referred to as the fast rotation, can be used to determine the average radial position of the muon distribution in the ring. Figure 5.13 shows the fast rotation signal at early times. The peaks are separated by the 149 ns muon time of flight around the ring. Figure 5.14 compares a Fourier transform of this signal with a signal from simulation in which the phase space of the storage ring was filled uniformly. The fast rotation signal is consistent with uniform filling of phase space.

The average vertical distribution of the muons in the storage region was studied by using current loops to change the radial magnetic field, which moved the beam up or

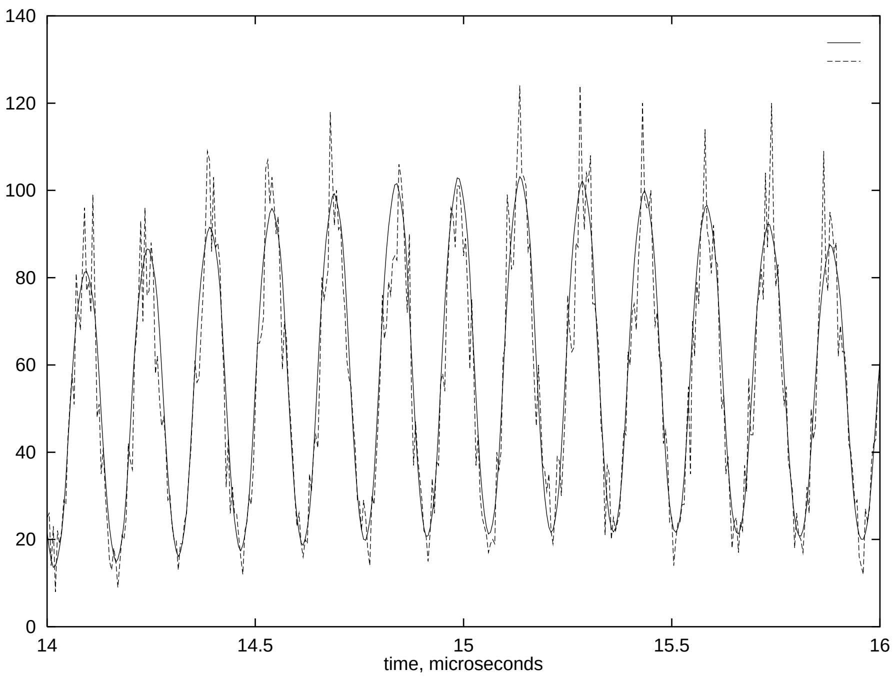

Figure 5.13: The electron decay spectrum at early times, called the fast rotation, shows the time evolution of the muon bunch. The vertical axis displays the number of decay electron counts and the horizontal axis has units of time.

down and changed the efficiency for storing muons. It was found that the stored muon beam filled the vertical phase space, but was shifted approximately 1 mm too high from the measured radial magnetic field.

By tracking simulated muons, which uniformly filled the storage ring phase space, through the measured magnetic field the final average absolute magnetic field was obtained:

$$< B >= 61.78850\ MHz \pm 0.9\ ppm \pm\ 1.0\ ppm\ ,$$

where the first uncertainty is from knowledge of the muon distribution weighted average magnetic field and the second uncertainty is from the absolute calibration of the magnetic field.

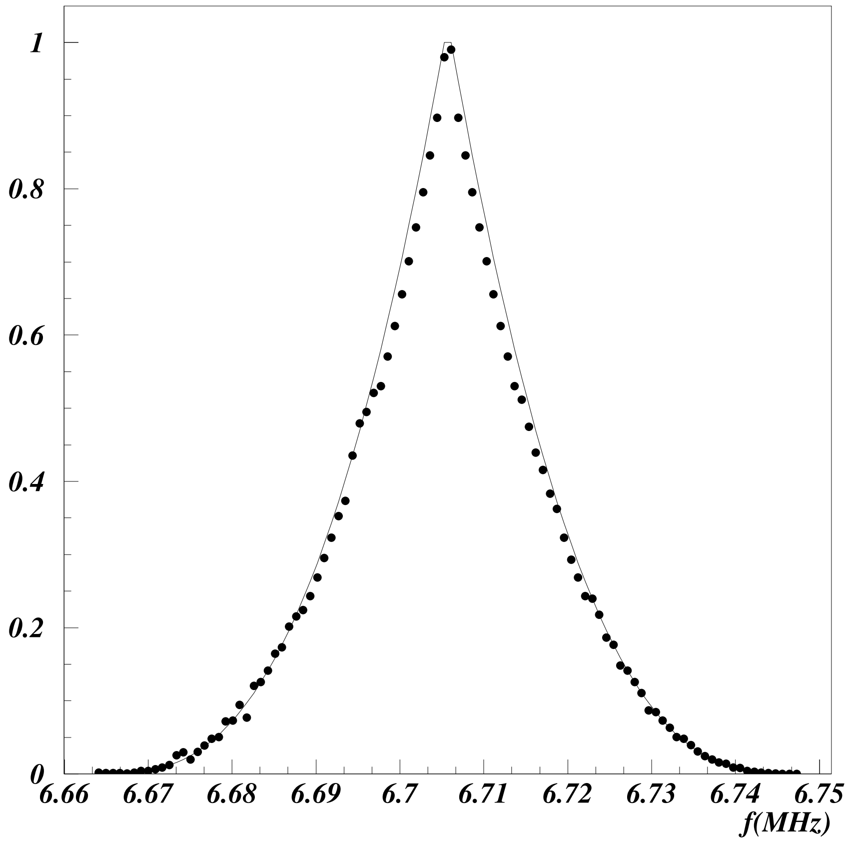

Figure 5.14: The fast Fourier transform of the fast-rotation signal (points). The solid curve is the frequency distribution expected if the phase space of the ring is uniformly filled by the muons.

Chapter 6

Systematic Uncertainties in f_a

Monte Carlo data was created to test the Ratio fit with three goals in mind. First, to test the fit for statistical consistency, making sure that the values and errors on fit parameters are correct. Second, to understand any systematic effects that were associated with 'backgrounds' seen in the data. Specifically, effects from narrow-pulses, WFD inefficiency, changing asymmetry, bin-width, shift-error, the 'laser hole', and the fast-rotation were examined. Third, to gauge the performance of the Ratio fit by comparing it with the standard 5-parameter fit function in Equation (A.1).

6.1 Statistical Consistency

Histograms based on the time spectrum in Equation (A.1), were created with random bin errors to determine whether the Ratio fit returned the correct values and errors for the fit parameters. The input parameters were the following:

$N_\circ = 150000.0$

$A = 0.5$

$\gamma\tau = 64400.0$ ns

$f_{MC} = 1/4366.0$ ns

ϕ = 0.0 rad.

ndf = (number of bins in fit) - (number of fit parameters) $\sim$ 909

Histogram bin-width of 545.75 ns was chosen so exactly 8 bins would constitute the 4366.0 ns (g-2) period. There were 1000 such time bins, and the lower and upper limits were 15000.0 ns to 560750. ns respectively—histograms were created to resemble the real data. There were 2800 histograms, each with 500k entries, and 700 ratios were constructed. The histograms were fit from bin 28 until bin contents were below the 5-count threshold (see section A.3). The results are shown in Figure 6.1 and 6.2 for the Ratio fit and 5-parameter fit respectively. Results for these fits are almost identical—as they should be. Several conclusions can be drawn about the Ratio fit applied to the this Monte Carlo data:

- The mean of the $f_{fit} - f_{MC}$ for the 700 histograms is on the order of the standard error of the mean (compare the Mean in plot (a) with its error). Therefore, at the level of 1 ppm, the Ratio fit returns the correct value for the frequency.

- The error returned by the fit is consistent with the statistical power of the input data (compare the Sigma in plot (a) with the Mean in plot (b)). Thus, the errors δR defined for the Ratio are correct.

- The mean and width of the $(\frac{\chi^2}{ndf})$ distribution (shown in plot (c)), agree with their predicted values of 1 and $\sqrt{\frac{2}{ndf}} \approx 0.047$ respectively. This means that the χ^2 can be used as a 'goodness of fit' parameter; and with point two, means that constructing the ratio with the 4 independent histograms has eliminated correlations—as expected.

- There is a strong correlation between the phase and the frequency (plot (d)). Correlation between these two parameters in the fit was 0.9 (or from the plot, 5.7 ppm in frequency for a 1 mrad shift in the phase). Correlation between the parameters means that the statistical error is increased, and this can be seen by the factor of $\sqrt{2}$ in the numerator of the analytical expression for the error on ω_a,

$$\frac{\delta\omega_a}{\omega_a} = \frac{\sqrt{2}}{\omega_a A\gamma\tau\sqrt{N_e}}.$$

Essentially, the error in the frequency includes the error in the phase added to it in quadrature (see reference [53] for further details on correlation).

6.2 Systematic Uncertainties from Background

With the statistical consistency of the Ratio fit established in the previous section, experimentally observed background effects were simulated to understand how they would influence the Ratio fit. Backgrounds of narrow-pulses, WFD inefficiency, changing asymmetry, the 'laser hole', and the fast-rotation were simulated. In addition, the effect of the shift-error and bin-width were examined.

In the previous section, 700 histograms were constructed to simulate the (g-2) spectrum with its random fluctuations in the bin contents. This was useful for testing the statistical nature of the Ratio fit, but fitting the histograms was time consuming. For the systematic background tests discussed below, effects from the background are understood by super-imposing background on top of decay spectra *without* statistical fluctuations in the bin contents. This allows tests to be done *much* more quickly, since only one histogram (not 700) needs to be fit. Testing in this fashion makes the *value* of the χ^2 meaningless in its statistical sense, but its relative value can still be used for minimization.

6.2.1 Phase Pulling

Phase pulling occurs if the fit function and the distribution to be fit are different. Phase pulling is observed by plotting f_{fit} versus the start of the fit (Figure 6.3.b), where the start of the fit (with respect to the phase of the (g-2) period) is what modulates the effect. In the 5-parameter fit, this could occur if the exponential decay of the distribution is not exponential (e.g., there is a time dependent efficiency). In the Ratio fit, it can arise from neglecting higher order terms in the fit function. In both cases, the amplitude of the effect is determined by how well the function models the data. At some level, there will always be phase pulling, but since it is an oscillatory effect, it can be minimized by using the fit values located at a zero crossing. An analytical description of phase pulling can be found in [53].

6.2.2 Shifting Error

Two of the four histograms used in the construction of the Ratio have their contents shifted. One is shifted by $+[\frac{T_{\omega a}}{2}+\delta]$, and the other by $-[\frac{T_{\omega a}}{2}+\delta]$. Because the frequency is not known exactly, δ is used and represents the shifting error. The effect from shifting error was examined by fitting time spectra with different input frequencies (the same bin-shift was used in each case). Figure 6.4 shows the difference between the frequency from the fit and the input frequency as a function of δ. From this Figure it is clear that the impact of shifting error on the frequency is a small. There is a relative phase pulling offset of about +0.12 ppm because the fit was started at the second point of Figure 6.3.b. With this offset subtracted out, a typical δ of 200 ppm, creates a bin shift error of just 0.03 ppm. If necessary, this graph can be used to correct for the shifting error.

6.2.3 Additive Background

The systematic shift associated with an additive background (narrow-pulses), is understood in two ways. First, the power law of Equation (A.10) is used to simulate an additive background and determine the general nature of the effect. Also, the indirect effect of histogram bin-width is examined (see section A.2). Secondly, because the additive background in the data cannot be accurately parameterized (the accuracy depends on the detector), narrow-pulse background from the data is used to contaminate the decay-spectrum. The effect of this contamination, together with the estimated amount of narrow-pulse contamination seen in the data, is used to assign a detector averaged systematic error due to the narrow-pulse background.

The effect of the additive power law background on f_{fit} for the Ratio and 5-parameter fit can be seen in Figure 6.5. The additive background amplifies the phase-pulling effect. For both fits (Figure 6.5.b), $f_{fit} - f_{MC}$ are centered on zero, where they oscillate because of the phase-pulling background. The fits oscillate with once and twice the (g-2) frequency, for the 5-parameter and Ratio fit respectively. The amplitude of the oscillation is much smaller for the Ratio fit ($\sim$ 10–15 times less over the range of added background).

Functional versus Histogram Errors

For the 5-parameter fit, errors from the histogram (*not* errors calculated from the fitting function) were used in the calculation of the χ^2 . Use of functional errors shifted the center of the oscillation away from zero. This occurred because the 5-parameter function no longer represented parent distribution. Consequently, the errors were not correct, and the center frequency was shifted. Figure 6.6 displays the difference between fitting with functional and histogram errors when there is an additive background of 10%. Though using functional errors may smooth out the χ^2 surface, functional errors should *not* be used if the distribution being fit is not derived from the fit function!

Bin-width

In section A.2, it is shown that the bin-width could influence f_{fit} by introducing a time-shift. The time-shift arose because the center of a histogram bin, which represents an *average* value of the distribution over its width, and *not* the value of the distribution at the center of the bin, is used in the calculation of the χ^2 . In order to isolate the bin-width effect from the effect of the additive background (recall from section A.2, without an additive background, there can be *no* bin-width effect), the difference $(f_{fit} - f_{MC})_{bin\ average} - (f_{fit} - f_{MC})_{bin\ center}$ is taken. The subscript 'bin average' means that a bin's contents was calculated by averaging the MC spectrum over the width of the bin. The subscript 'bin center' means that a bin's contents was calculated using the value of the MC spectrum at the center of the bin. Figure 6.7 shows this difference versus start of the fit for the Ratio and 5-parameter fits. Background contamination of 100% had to be used to make this difference visible for the Ratio fit. The effect of finite bin-width is to increase the amplitude of the phase-pulling oscillation. For both fits, increases were small (∼1–2%) compared to the amplitude of the phase-pulling induced from the background. In retrospect, this may have been expected considering the bin-width Δ enters in second order in Equation (A.12).

Additive Background from the Data

The effect of the additive background from the data on f_{fit} is shown in Figure 6.8. The plots are obtained by superimposing real background time spectra (pulses *not* selected as electrons in Figure 5.5) on top of the simulated decay spectrum so that the fraction of the integrated background to signal was 10%. The contour plots, like the one shown in Figure 5.5, were used to estimate the maximum percentage of background that spilled into the electron region. The estimated maximum percentage of background was $0.7 \pm 0.5\%$ (averaged over the detectors and running periods). Since the shift of about -1 ppm in Figure 6.8 represents 10% contamination, this shift should be reduced by the factor 0.7%/10%. Taking this into account, the effect from the additive background in the data should be on the order of -0.1 ppm.

6.2.4 WFD Inefficiency and Changing Asymmetry

In the real data, the efficiency changes because of the changing pedestal, and the changing efficiency induces a changing asymmetry. Though inefficiency and asymmetry are coupled, in order to understand their individual effect on f_{fit}, they are examined independently.

The effect of the WFD inefficiency on f_{fit} is examined by creating a time-dependent efficiency modeled as a power law . Specifically,

$$N_{\circ}(t) = N + \frac{\alpha}{(t-\beta)^p}. \tag{6.1}$$

Ratio and 5-parameter fits made on the spectrum created with $N_{\circ}(t)$ are shown in Figure 6.9. In Equation (6.1), N is a constant, $\beta = 15\mu$s, $p = 1.3$, and α is chosen so that the integrated drop in $N_{\circ}(t)$ corresponds to the percentage indicated in Figure 6.9. From section A.1, its expected that the Ratio fit will greatly reduce the effects of a time dependent efficiency. This is, in fact, the case (see Figure 6.9.a). However, the remaining phase-pulling oscillation does *not* oscillate around zero for the Ratio fit (Figure 6.9.b). Hence, there is a small early-to-late shift in due to WFD inefficiency for the Ratio fit. The shift is about +1 ppm per 10% loss in efficiency. The detectors exhibit losses in efficiency of typically 5%, so the +1 ppm should be an upper limit for any shift caused by loss of efficiency in the data. The 5-parameter fit does not exhibit this shift, though in practice, the large magnitude of its phase-pulling oscillation means that the uncertainty in determining the zero crossing is much greater than the shift seen in the corresponding Ratio fit.

A power law is also used to model the time dependent asymmetry. In this case,

$$A(t) = A\left(1 - \frac{\frac{\alpha}{(t-\beta)^p}}{N}\right),$$

where A is a constant, N serves as a normalization (the asymmetry should be between 0 and 1), and the minus sign indicates that the asymmetry *increases* with time (as it should since the effective energy threshold increases with time). Values for p and β are taken as above, and α is chosen so that the integrated asymmetry change is equal to the percent indicated if Figure 6.10.b. Figure 6.10.a shows what the changing asymmetry looks like in time, and Figure 6.10.b shows its effect on f_{fit} for the Ratio and 5-parameter fits.

There is a phase-pulling oscillation for both the Ratio and 5-parameter fits with a period of twice the (g-2) frequency. For the Ratio fit the oscillation is about zero. For the 5-parameter fit, the oscillation has peculiar periodicity.

6.2.5 Laser Hole

The calibration laser was fired during data collection so that calibration of timing shifts and gain stability of PMTs could be measured. As a result, 'holes', or more appropriately 'divots', were created in the decay electron spectra. Divots were created when a ± 30 ns window was excluded around the position of a laser pulse. With a histogram bin width of 545.75 ns, this meant that a bin which included a laser pulse would have its contents reduced by $\frac{60\,ns}{550\,ns} \approx 11\%$, if the laser was fired in the same bin every fill. Typically, the laser was fired in the same bin only once every 8 fills. In this case, a bin's contents would be reduced by $\frac{1}{8} \times 11\% \approx 1.4\%$. Figure 6.11 shows the effect of a divot in the data. From these plots, it is clear that a divot can lead to a major shift in f_{fit}. Also, the magnitude of the effect can be greatly reduced by choosing where the divot occurs in the decay distribution. It turns out that a 'laser surplus' leads to the same size effect, only with a different sign. A surplus, opposite in sense to a divot, can happen if all the laser pulses were not removed. A laser surplus is potentially more dangerous than a divot, because there is the chance that there would be a larger percentage change in the bin contents. The above numbers are based on a divot located near the start of the fit (8–16 bins away). A divot located further out in the distribution, relative to the start of the fit, created a smaller shift due to the lower statistical weight of the effected bin.

The simplest way around the problem is to eliminate the divoted bins from the fit, suffering only the small loss in statistics associated with the exclusion of these bins. This approach works without inducing a shift in the fit frequency when the fit function exactly matches the parent distribution. However, when the fit function is not an exact match (i.e., the real data), discontinuities associated with bin removal exist. Removing a laser bin from the simulated 10% changing efficiency data above, 8 bins away from the start of the fit, results in an shift of about 2 ppm. This shift is smaller than the 5 ppm shift that would have resulted from inclusion of a laser pulse in the real data (a laser pulse in the bin for 1 out of 8 fills). These shifts represent a maximal effect, since the changing efficiency in the detectors is closer to 5% (in worst case) and the effected bin was close to the start of the fit. However, to guard against a potential laser surplus and consequent large effect, it is important to remove the bins from the fit.

6.2.6 Fast Rotation

The effect of the fast rotation on the f_{fit} was determined by simulation. Jim Miller provided code that would simulate the fast rotation spectrum for our data. The code assumed that all particles were bunched at one place in the ring at T$\emptyset$, and then traced their evolution. The initial momenta of stored muons was divided up into narrow bins. At a given time, each bin is a 'box' distribution in azimuth. As time increases, the 'box' gets wider and its amplitude decreases—maintaining normalization. The amplitudes are added up over the angular acceptance of the detector for each momentum bin. The resulting probability distribution (Figure 6.12.a) was multiplied by the decay spectrum, and the result was fit (Figure 6.12.b). The result in Figure 6.12.b shows that start times of the fit should be taken in the ranges of 25–34μs or 56–65μs to keep systematic error associated with the fast rotation contamination below $\sim$1 ppm. Alternatively, if many different fits are used with various start times, this effect may average out.

Table 6.1: Systematic uncertainties in ppm[52].

Systematic Effect	error (ppm)
Absolute Magnetic field	1.0
Muon Distribution and $<B>$	0.9
Fitting Systematics:	
WFD inefficiency	0.5
zero crossing	1.0
additive background	0.1
changing asymmetry	0.1
laser hole	0.5
fast rotation	0.5
WFD Energy Threshold	1.5
Gain and Timing Shifts	0.6
Total Systematic Error	2.7

6.3 Summary of Systematic Uncertainties

Table 6.1 summarizes the systematic uncertainties for the 1997 (g-2) run. Beyond the fitting systematics, only effects which contributed at a level greater than 0.5 ppm were included.

In addition to causing problems when fitting the data, the changing WFD energy threshold (increasing average decay electron energy) induced a direct timing shift, since, on average, high-energy decay electrons traveled further than low-energy decay electrons before striking the calorimeters.

Gain and Timing shifts associated with the PMTs and fitting were measured by comparing the fit times of pulses with those from the reference photodiode. Gain and timing shifts were, on average, less than 3% (0.6 ppm) and 20 ps (0.1 ppm) respectively.

Two corrections were made to the frequency obtained from fitting. The first correction (0.7 ppm) was due to the electric field, which affected muons that were not at the magic gamma since $\frac{\delta p}{p} = 0.5\%$ for the storage ring. The second (0.4 ppm), was the so-called pitch correction that is necessary due to the vertical betatron oscillations[2].

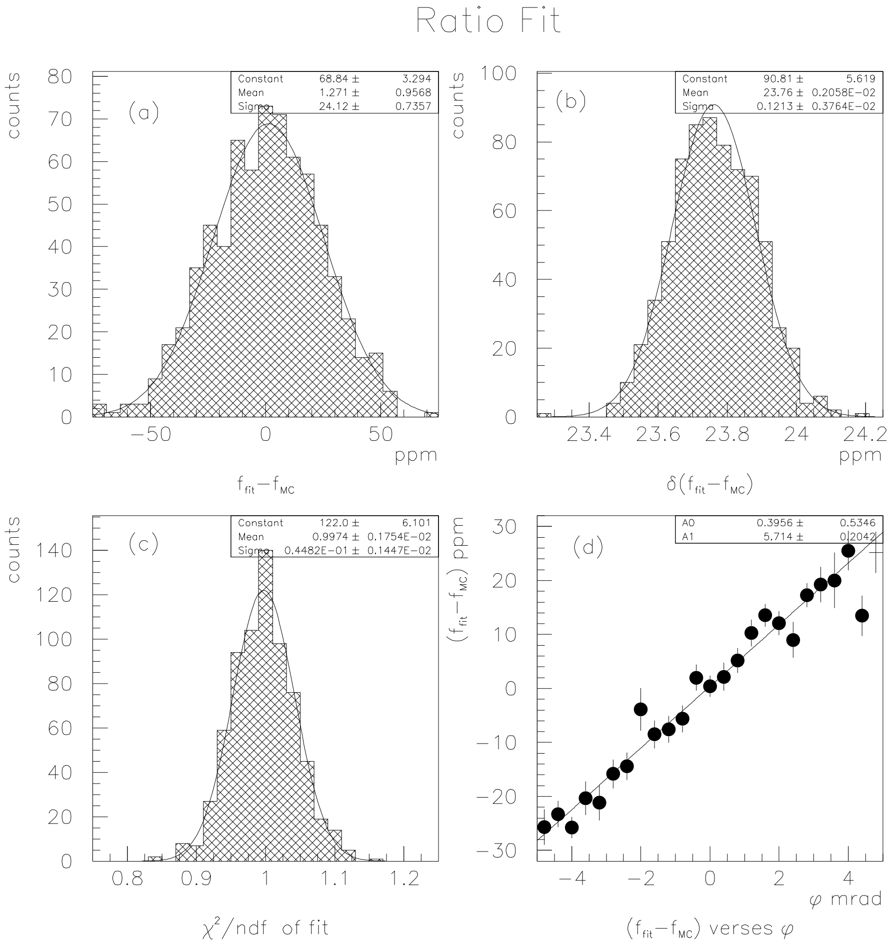

Figure 6.1: Results for the Ratio fit applied to the 700 Monte Carlo histograms: *(a)* shows the distribution for $f_{fit} - f_{MC}$, in units of parts-per-million (ppm). *(b)* shows the error on the fit-frequency in units of ppm. *(c)* shows the distribution χ^2/ndf of the fit. *(d)* is a plot of phase versus frequency from the fit and shows the correlation between them.

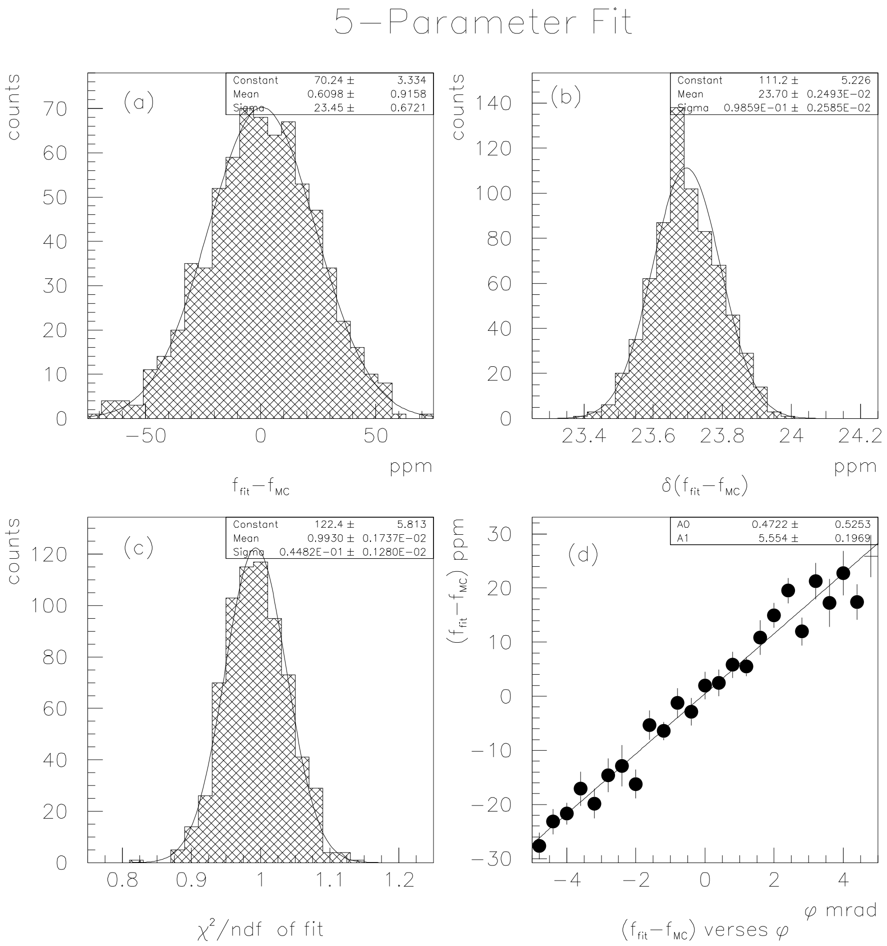

Figure 6.2: Results for the 5-parameter fit applied to the 700 Monte Carlo histograms: *(a)* shows the distribution for $f_{fit} - f_{MC}$, in units of parts-per-million (ppm). *(b)* shows the error on the fit-frequency in units of ppm. *(c)* shows the distribution χ^2/ndf of the fit. *(d)* is a plot of phase versus frequency from the fit and shows the correlation between them.

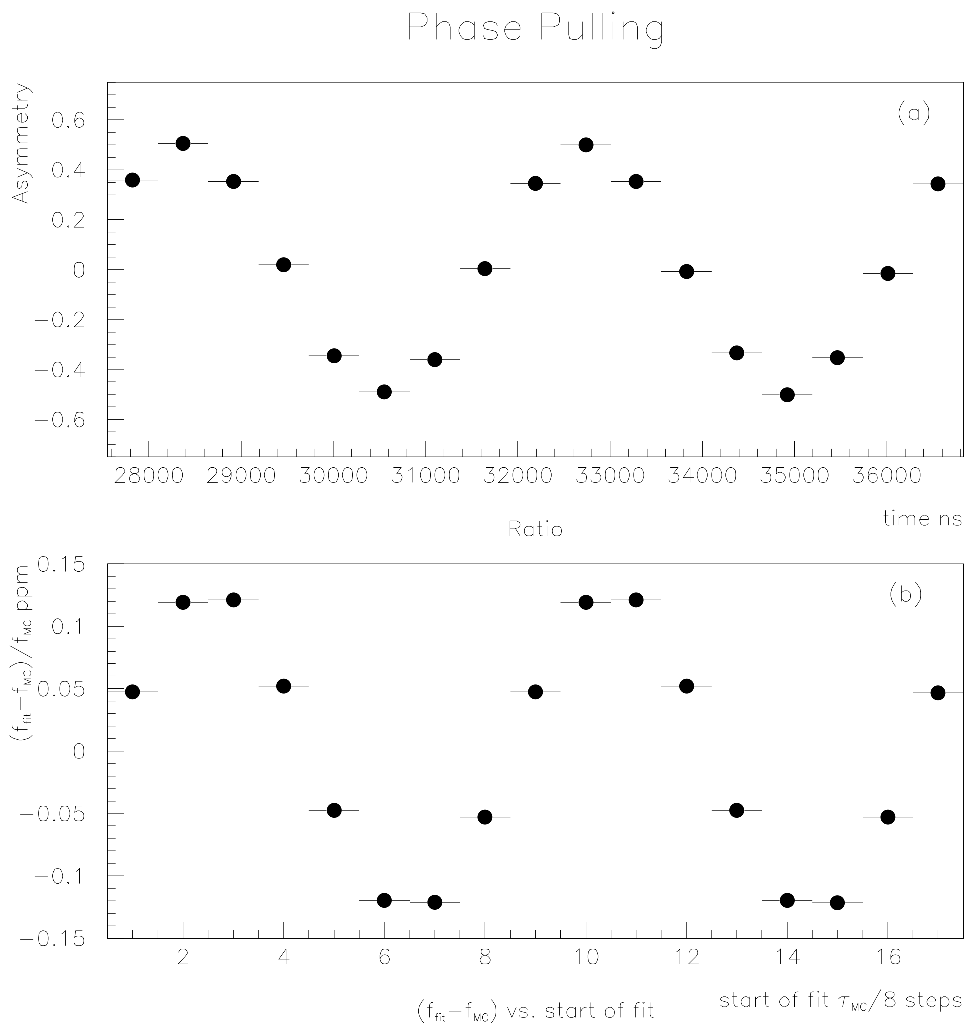

Figure 6.3: *(a)* Ratio for Monte Carlo data. *(b)* $f_{fit} - f_{MC}$ versus start of Ratio fit. The phase pulling oscillations are from neglected second order terms in the in the Ratio. The Ratio in (a) and the Phase pulling effect in (b) oscillate with the same frequency but there is a phase shift of $\sim \frac{\tau_{MC}}{2}$

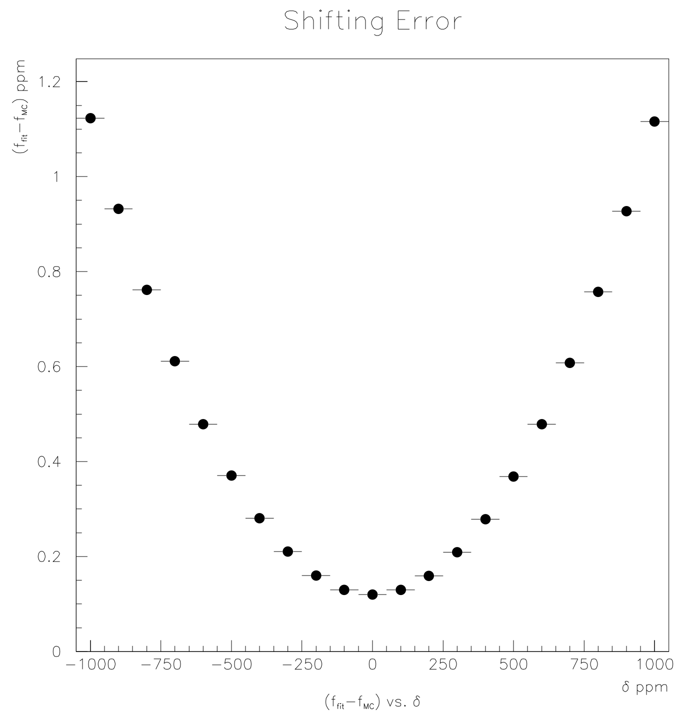

Figure 6.4: $f_{fit} - f_{MC}$ versus δ, where $\delta = f_{MC} - f_{bin}$ ($f_{bin} = 1/4366\ ns$). Both axes are divided by f_{bin}, and are in units of ppm.

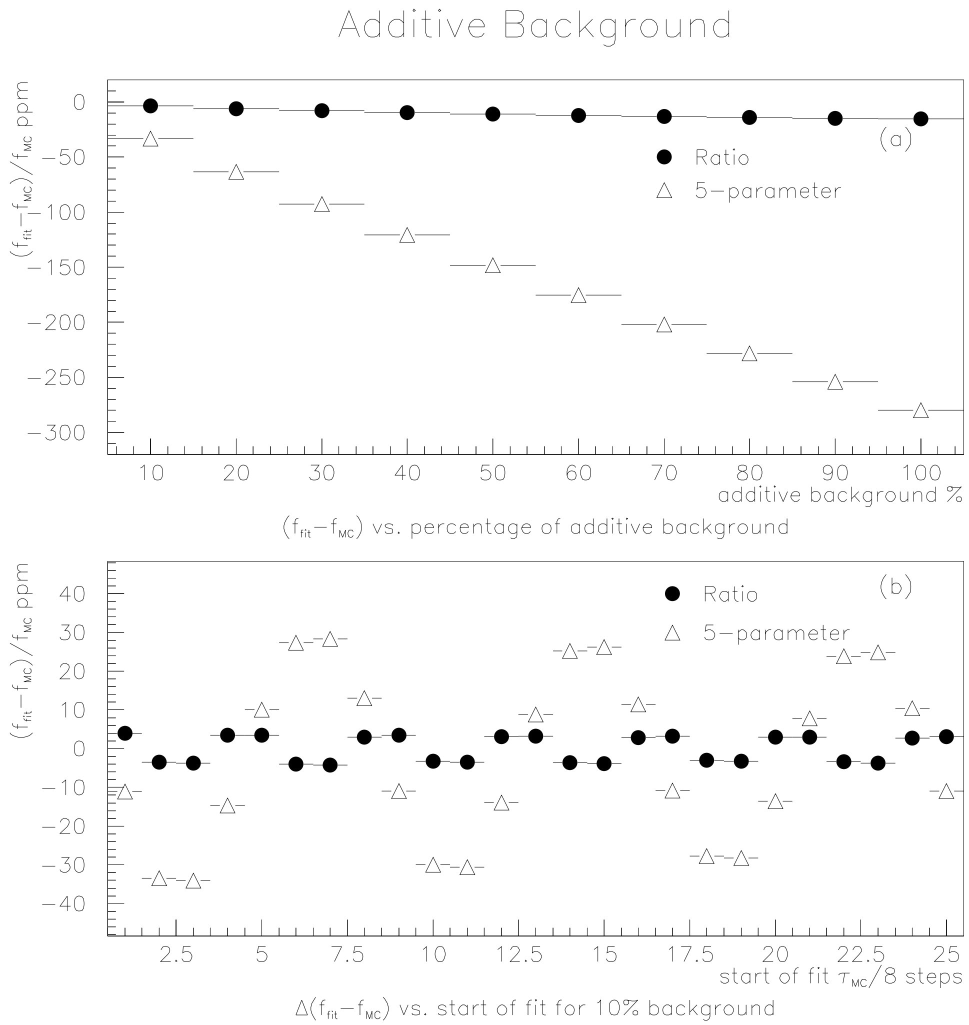

Figure 6.5: *(a)* $f_{fit} - f_{MC}$ versus the fraction of additive background. The background is generated by the power law in (A.10) with $\beta = 15000\ ns$, $p = 1.3$, and α chosen so that the fraction of integrated background to integrated signal corresponds to the percent indicated. *(b)* $f_{fit} - f_{MC}$ versus the start of the fit for 10% integrated background. Values for $f_{fit} - f_{MC}$ in (a) are taken where the phase pulling oscillation is a maximum (the second point in (b)). Histogram errors, instead of functional errors, are used for calculating the χ^2 for the 5-parameter fit.

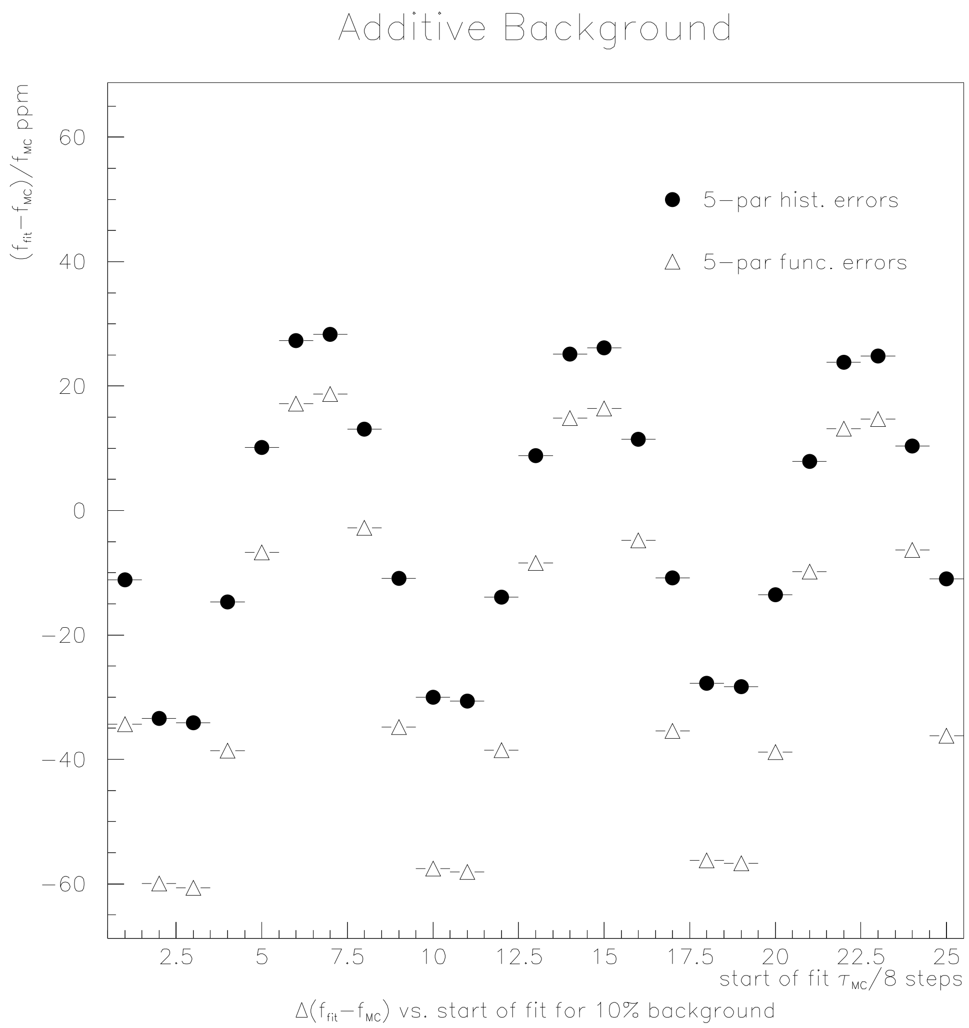

Figure 6.6: $f_{fit} - f_{MC}$ versus the start of the fit for 10% integrated background. The 5-parameter fit is performed using first the functional errors and then histograms errors in the calculation of the χ^2.

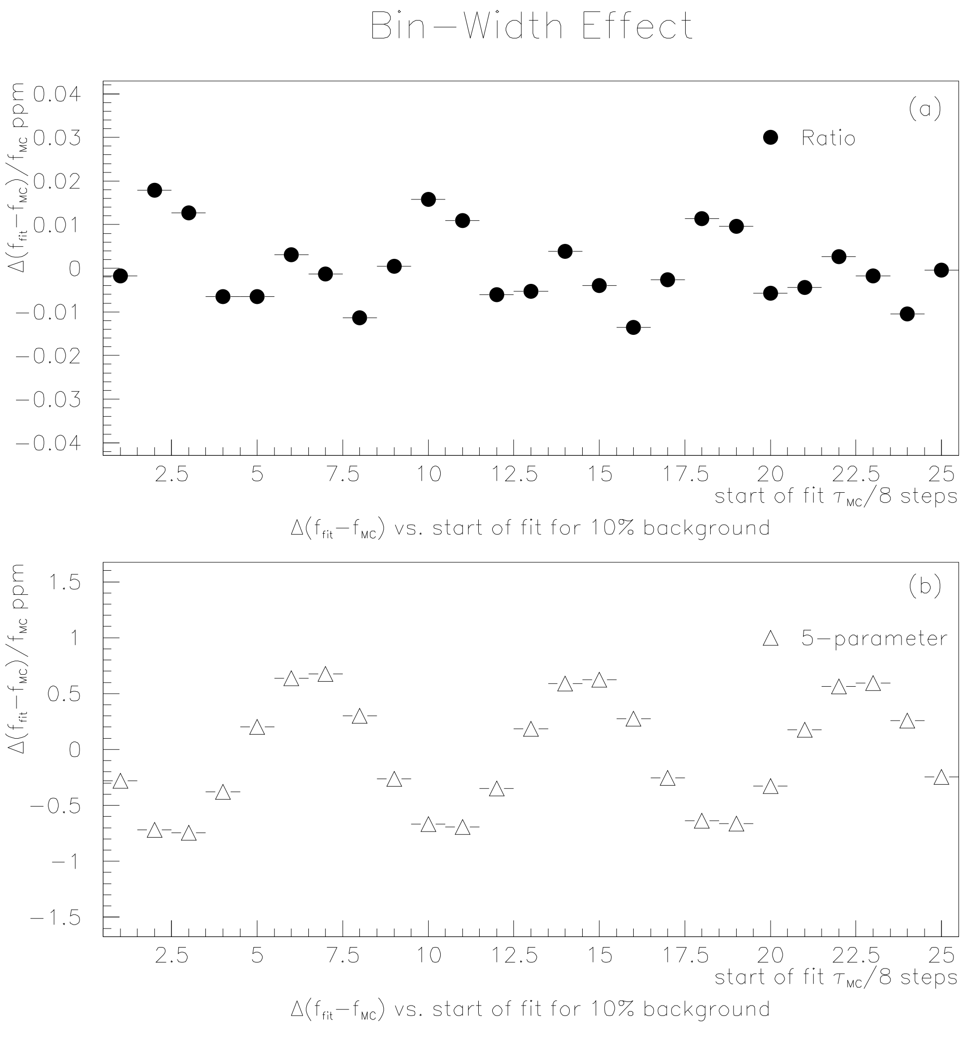

Figure 6.7: The difference between $(f_{fit} - f_{MC})_{bin\ average} - (f_{fit} - f_{MC})_{bin\ center}$ versus start of fit for *(a)* the Ratio fit, and *(b)* the 5-parameter fit. The subscript 'bin average' means that a bin's contents was calculated by averaging the MC spectrum over the width of the bin. The subscript 'bin center' means that a bin's contents was calculated using the value of the MC spectrum at the center of the bin.

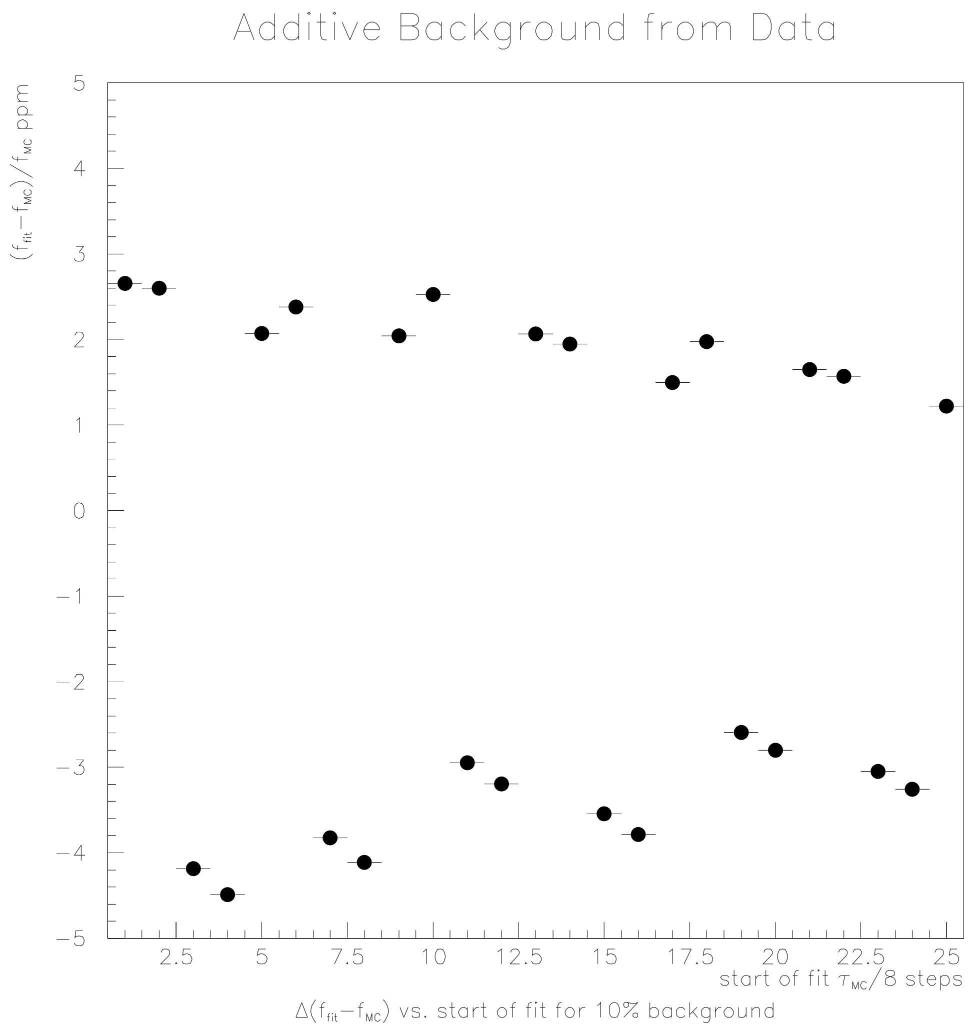

Figure 6.8: $f_{fit} - f_{MC}$ versus start of the Ratio fit for 10% background from the data.

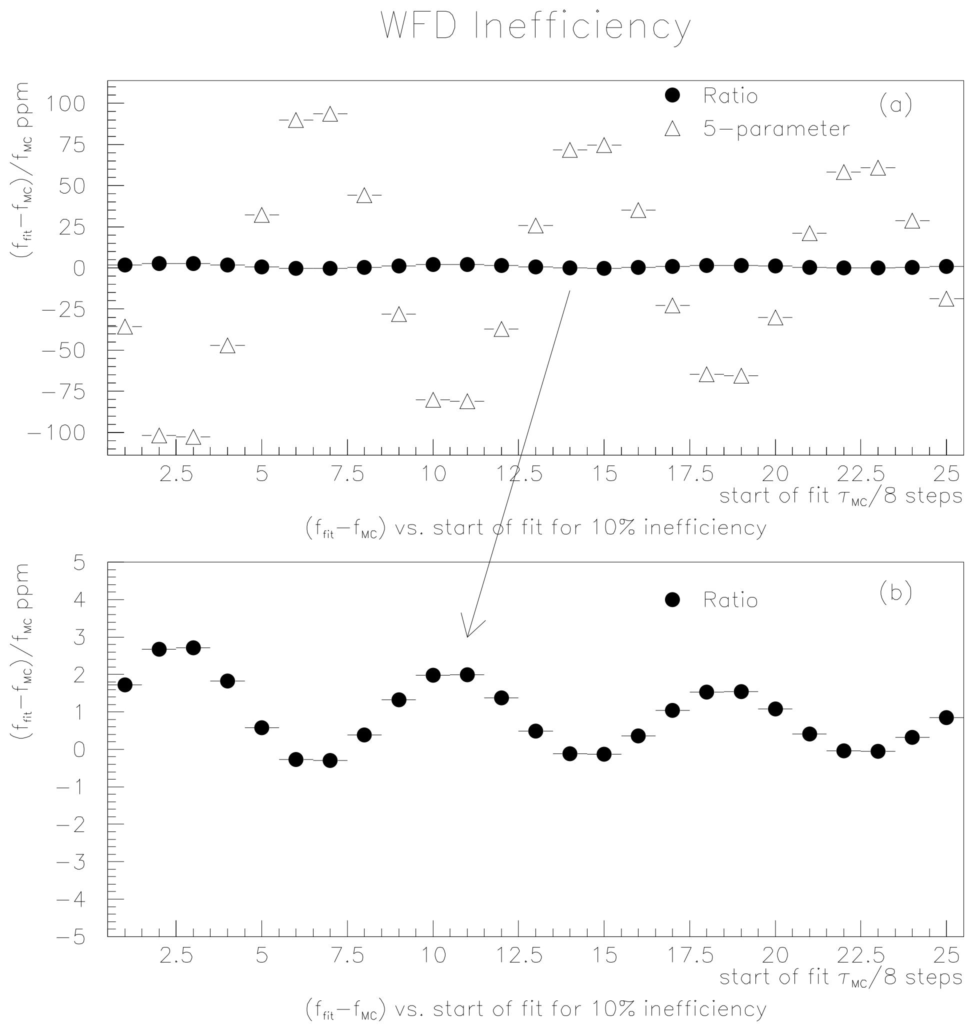

Figure 6.9: The effect of WFD inefficiency on Ratio and 5-parameter fits: *(a)* $(f_{fit}-f_{MC})$ versus start of fit for 10% WFD inefficiency. *(b)* Blow-up of Ratio fit. The Ratio fit does *not* oscillate around zero.

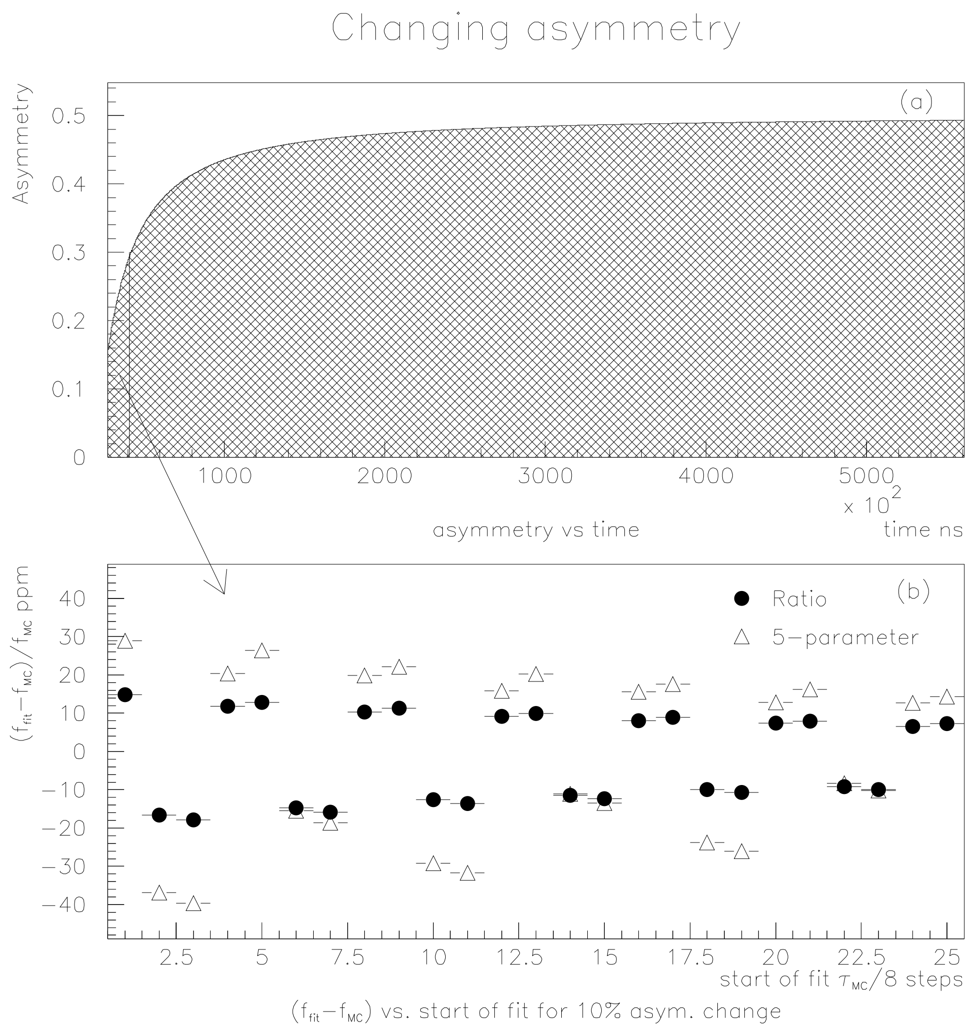

Figure 6.10: *(a)* Changing asymmetry with time. *(b)* $f_{fit} - f_{MC}$ versus the start of fit for the decay spectrum with the changing asymmetry shown in (a). $f_{fit} - f_{MC}$ oscillates around zero for the Ratio fit, but not for the 5-parameter fit.

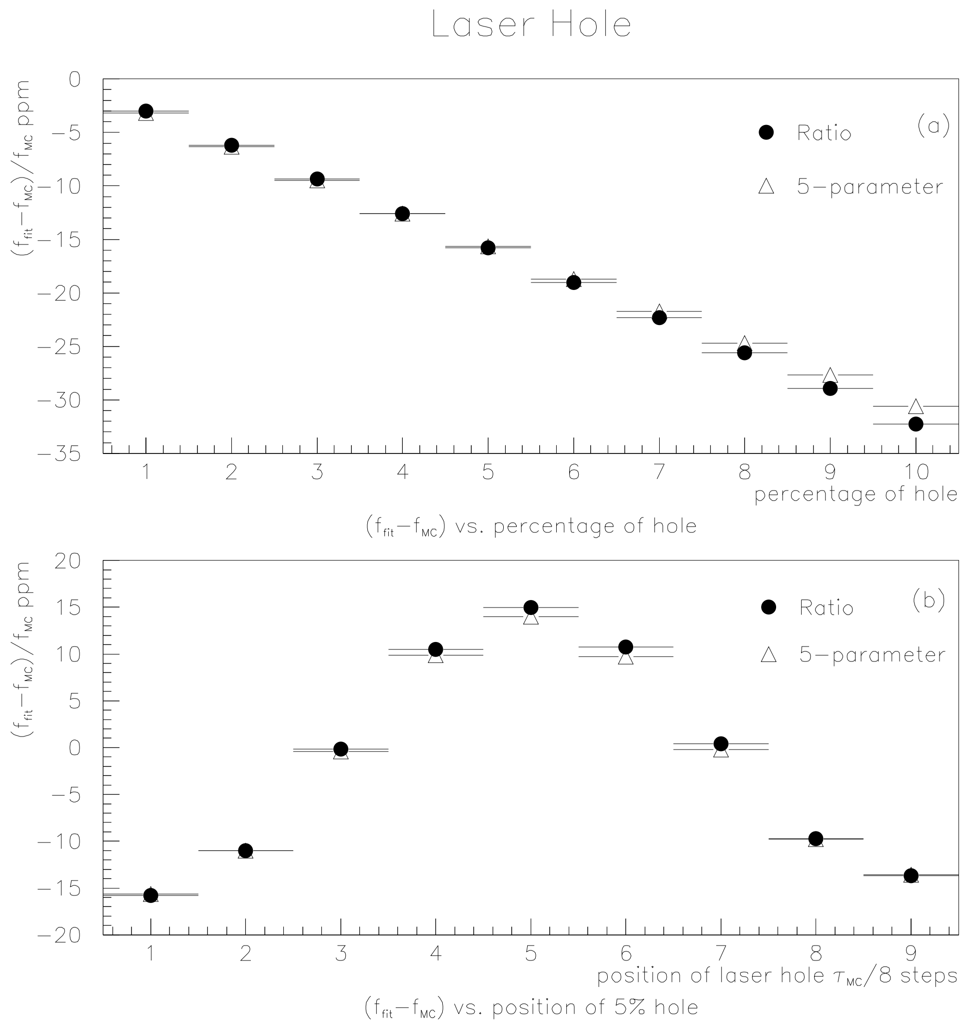

Figure 6.11: *(a)* $f_{fit} - f_{MC}$ versus the percentage size of the hole. The fits started 8-bins before the hole. *(b)* $f_{fit} - f_{MC}$ versus the position of a 5% laser hole with respect to the (g-2) frequency. The first point here corresponds to a zero-crossing (the eight point of the (g-2) oscillation seen in the Ratio of Figure 6.3.a.)

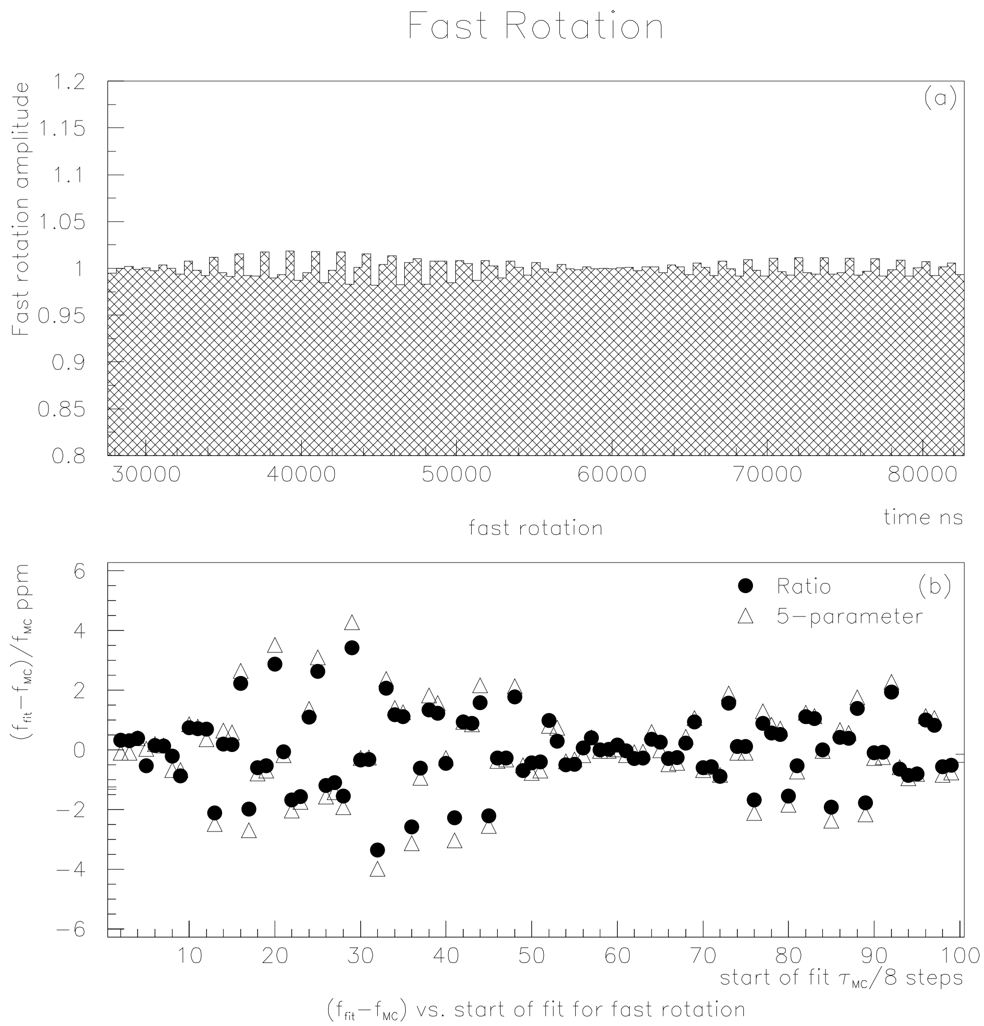

Figure 6.12: *(a)* Normalized probability distribution for the fast-rotation spectrum. The distribution was calculated every 5.4575 ns and binned (545.75 ns) to match the decay spectrum histogram so the two could be multiplied. *(b)* $f_{fit} - f_{MC}$ versus the start of fit for the fast rotation contaminated decay spectrum. Though they are written in different units, the start times are the same in both plots.

Chapter 7

Conclusions

Using the values obtained from Chapters 5 and 6 for f_a from the Ratio analysis, f_p from the magnetic field, and the corrections to f_a

$$\begin{aligned}
\mathcal{R} &= \frac{f_a}{f_p} \\
&= \frac{\overbrace{2.291 \times 10^{-4}\ Hz \cdot (1 - 153.4 \times 10^{-6})}^{f_a} \cdot (1 + \overbrace{0.69 \times 10^{-6} + 0.4 \times 10^{-6}}^{corrections})}{\underbrace{61.78850 \times 10^{+6}\ Hz}_{f_p}} \\
&= 3.707\ 245(52) \times 10^{-9}\ .
\end{aligned}$$

With $\lambda = 3.183\ 345\ 47(47)$[21]

$$\begin{aligned}
a_\mu &= \frac{\mathcal{R}}{\lambda - \mathcal{R}} \\
&= 1\ 165\ 933(16) \times 10^{-9}\ (\pm 14\ ppm)\ , \qquad (7.1)
\end{aligned}$$

where the error is the sum of the systematic errors (2.7 ppm) and the statistical error on the frequency (13.9 ppm) added in quadrature (14.2 ppm).

The official (8-parameter) analysis[52] reports the value

$$a_\mu = 1\ 165\ 925(15) \times 10^{-9}\ (\pm 13\ ppm)\ . \qquad (7.2)$$

Again the systematic error (2.9 ppm) and statistical error on the frequency (12.6 ppm) are added in quadrature (12.9 ppm). Figure 7.1 shows the values of a_μ for the Ratio and 8-parameter analysis, as well as the values from the previous CERN experiments (a_μ and a_{μ^-}). Due to the difference in statistical errors, a difference in the value of a_μ

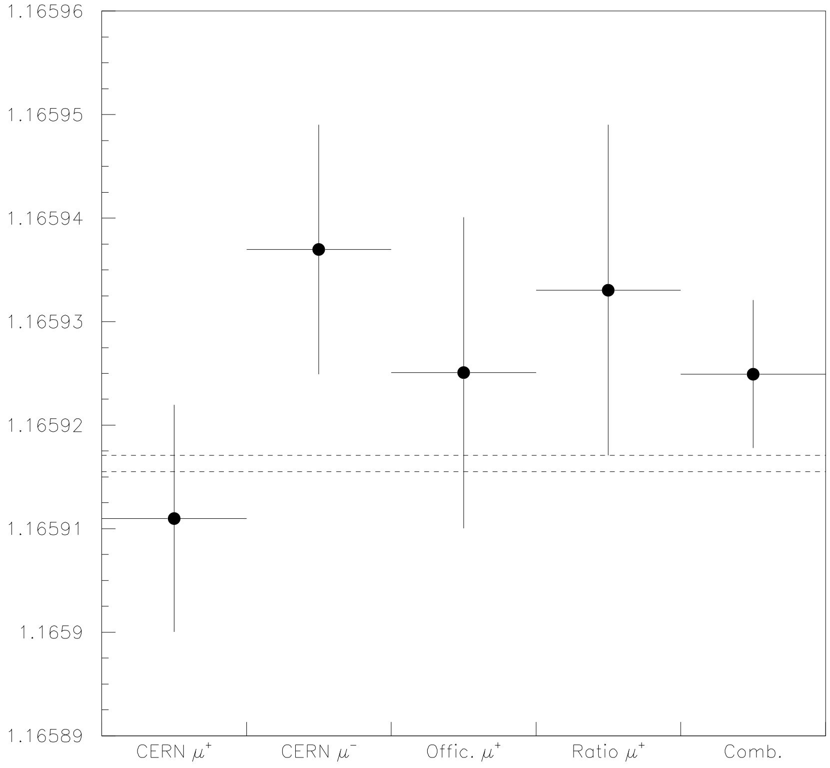

Figure 7.1: a_μ for the previous CERN and current Brookhaven muon (g-2) experiments. The dashed lines indicate the $\pm$ 1 σ region predicted by the Standard Model.

is expected. Indeed, the Ratio and official 8-parameter analysis differ from each other by 6.8 ppm. A one sigma difference for the two results for these statistical errors is

5.9 ppm; therefore, the two analysis agree within 1.16 σ. In addition, both the Ratio and 8-parameter analysis agree (1.0 σ and 0.5 σ respectively) with the Standard Model prediction.

The major differences between the Ratio and 8-parameter analyses were: the fitting function, time spectra groupings, and start-times of the fits. The difference between the statistical uncertainty for the Ratio (13.9 ppm) and 8-parameter (12.6 ppm) analyses was due to the later start-times used in the the former, which kept systematic effects associated with fitting the frequency below 1.3 ppm. Alternatively, the 8-parameter analysis had a less detailed study of the fitting systematics and assigned a single 2.0 ppm error to cover any shifts associated with the start-times of the fits.

Combining the CERN results and the Ratio analysis, a new world average is obtained (the point labeled "Comb." in Figure 7.1)

$$a_\mu \quad = \quad 1\ 165\ 925(7) \times 10^{-9}\ (\pm 6\ ppm)\ . \tag{7.3}$$

The 1997 data run proved useful for debugging *every* aspect of the new (g-2) experiment, spawning new analysis techniques, and improving the measured value of a_μ (world average). We are now ready to tackle the challenges which accompany muon injection, poised for the potential discovery that a 1 ppm measurement in the 1998 data runs might bring.

Appendix A

Ratio Method

The Ratio Method is a prescription for minimizing the effect of time-dependent inefficiency on the (g-2) frequency analysis. First suggested by Yuri Orlov, and developed independently by the author, the Ratio Method takes advantage of the periodicity of the decay electron spectrum, using the shifted decay electron spectrum to divide out the multiplicative background.

A.1 Theory

The expected decay electron spectrum for the (g-2) experiment can be represented by a 5-parameter function

$$N(t) = N_{\circ} e^{-t/\gamma\tau}[1 - A\cos(\omega_a t + \phi)] \ , \tag{A.1}$$

where $N_{\circ}$ and A are constants with respect to time. Including the WFD inefficiency and the narrow pulses, Equation (A.1) becomes

$$N(t) = N_{\circ}(t) e^{-t/\gamma\tau}[1 - A(t)\cos(\omega_a t + \phi)] + C(t) \ , \tag{A.2}$$

where $N_{\circ}(t)$ represents the changing efficiency which induces a changing asymmetry $A(t)$, and C(t) represents the narrow pulse background.

Now consider the Ratio

$$R(t) = \frac{u(t) - v(t)}{u(t) + v(t)} = \frac{\frac{u(t)}{v(t)} - 1}{\frac{u(t)}{v(t)} + 1} \ , \tag{A.3}$$

with

$$u(t) = N(t - [\tfrac{\tau_{\omega_a}}{2} + \delta]) + N(t + [\tfrac{\tau_{\omega_a}}{2} + \delta]) \ , \tag{A.4}$$

and

$$v(t) = 2N(t) \ , \tag{A.5}$$

where $\tau_{\omega_a} \equiv \frac{2\pi}{\omega_a}$ is the (g-2) period. The $\pm[\frac{\tau_{\omega_a}}{2} + \delta]$ terms represents a shift of the decay spectrum to the left or right by half a (g-2) period. Because the period of the real data is not known exactly, δ is included and represents the error in the half-period shift. Since $\delta \ll \frac{\tau_{\omega_a}}{2}$,

$$\frac{\delta}{\frac{\tau_{\omega_a}}{2}} \sim \frac{1\ ns}{\frac{4366\ ns}{2}} \sim \frac{1}{2200} \ ,$$

and it is only important when expanding $\cos(\omega_a t + \phi)$ in Equation (A.2). Specifically,

$$\cos(\omega_a t \pm [\tfrac{\tau_{\omega_a}}{2} + \delta] + \phi) = -\left(\cos(\omega_a t + \phi)\cos(\frac{2\pi\delta}{\tau_{\omega_a}}) \mp \sin(\omega_a t + \phi)\sin(\frac{2\pi\delta}{\tau_{\omega_a}})\right) \tag{A.6}$$

Using this, and the Taylor series expansion

$$N_\circ(t \pm [\tfrac{\tau_{\omega_a}}{2} + \delta]) \approx N_\circ(t \pm \tfrac{\tau_{\omega_a}}{2}) = N_\circ(t) \pm N'_\circ(t)[\tfrac{\tau_{\omega_a}}{2}] + \frac{1}{2}N''_\circ(t)[\tfrac{\tau_{\omega_a}}{2}]^2 \pm \cdots \ ,$$

Equation (A.3) yields

$$R(t) = \frac{-A\cos(\omega_a t + \phi)}{1 + \frac{C(t)}{N_\circ(t)e^{-t/\gamma\tau}}} \approx -A(t)\cos(\omega_a t + \phi) \ , \tag{A.7}$$

through first order in τ_{ω_a} and δ.

Examining the effect of second order terms in $N_\circ(t)$, and the shift τ_{ω_a} ($\delta \ll \tau_{\omega_a}$, so terms involving δ are neglected), Equation (A.3) becomes (through second order),

$$\mathcal{O}^{0+2}(R(t)) = \frac{\mathcal{O}^0(\frac{u(t)}{v(t)}) + \mathcal{O}^2(\frac{u(t)}{v(t)}) - 1}{\mathcal{O}^0(\frac{u(t)}{v(t)}) + \mathcal{O}^2(\frac{u(t)}{v(t)}) + 1} \ . \tag{A.8}$$

Thus, comparing the amplitude of the second and zero order terms in Equation (A.8),

$$\frac{\mathcal{O}^2(\frac{u(t)}{v(t)})}{\mathcal{O}^0(\frac{u(t)}{v(t)})} = \left(\frac{1}{(\gamma\tau)^2} - 2\frac{N_\circ'(t)}{N_\circ(t)}\frac{1}{\gamma\tau} + \frac{N_\circ''(t)}{N_\circ(t)}\right)[\tfrac{\tau_{\omega a}}{2}]^2 \ . \tag{A.9}$$

In order to evaluate this, we must assume a form for $N_\circ(t)$. Since the efficiency is related to the pedestal, which ultimately determines the effective threshold of the WFD, and the pedestal time dependence has the form of a power law (Section 5.1.3), it follows that WFD efficiency should have a power law time dependence[1]. Thus, the efficiency is parameterized as

$$N_\circ(t) = N + \frac{\alpha}{(t-\beta)^p} \ , \tag{A.10}$$

where N, α, β, and p are constants. Fitting this function to the WFD pedestal in the data gives: $0.6 \leq p \leq 1.3$, and $(t-\beta) \sim 30\mu s$ for the detectors. Using this form to evaluate the derivatives, we get

$$\frac{N_\circ'(t)}{N_\circ(t)} = \frac{-p}{t-\beta}\left(\frac{1}{1+\frac{N(t-\beta)^p}{\alpha}}\right) \sim -\frac{1}{23\mu s} \ ,$$

and

$$\frac{N_\circ''(t)}{N_\circ(t)} = \frac{p\,(p+1)}{(t-\beta)^2}\left(\frac{1}{1+\frac{N(t-\beta)^p}{\alpha}}\right) \sim \frac{3.0}{(30\mu s)^2} \ ,$$

where $p = 1.3$ has been used as worse case. Substituting the numbers into Equation (A.9) (with $\gamma\tau = 64\mu s$ and $\frac{\tau_{\omega a}}{2} = 2.2\mu s$)

$$\frac{\mathcal{O}^2(\frac{u(t)}{v(t)})}{\mathcal{O}^0(\frac{u(t)}{v(t)})} \sim \frac{1}{40} \ . \tag{A.11}$$

The Ratio has managed to eliminate $N_\circ(t)$ and its first derivative, as well as the first order contributions of $\frac{\tau_{\omega a}}{2}$ and δ from the shift. $N_\circ(t)$ still appears in the denominator in Equation (A.3), but is substantially reduced by the narrow-pulse to electron-pulse fraction. Also, second order terms show that contributions from time dependent efficiency

[1] In general, the only requirement for the Ratio Method is that derivatives of $N_\circ(t)$ are small with respect to the shift $\frac{\tau_{\omega a}}{2}$, so that Taylor series expansion is valid.

should be reduced by *at least* a factor of 40. $A(t)$ remains, and its time dependence is accounted for by a linear approximation (see Section A.3). The narrow-pulse term, $C(t)$, is minimized by eliminating narrow-pulses based on parameters from the pulse-fitting routine.

A.2 Constructing the Ratio with the Data

The Ratio Method is applied to the (g-2) decay electron spectrum in the following way: decay electron pulses are randomly distributed into four histograms, creating four independent ensembles of data. Each histogram is created with about 8 time bins per (g-2) period (since $\tau_{\omega_a} \sim 4365.5\,ns$, choosing 8 bins with a 545.75 ns width gives a histogram period of 4366.0 ns). Construction of the Ratio then proceeds from Equation (A.3), where the distributions shifted by $\pm\tau_{\omega_a}$ are created by shifting the contents of a histogram by ± 4 bins. Figure A.1 shows an example of the Ratio constructed with the data.

In principle any even number of bins per (g-2) cycle would work. Eight bins represents an optimization between two competing effects: The wider the bins, the more events per bin and the further out the (g-2) frequency can be fit. However, with fewer than 8 bins per (g-2) cycle, the asymmetry becomes appreciably diluted, and statistical error is increased.

For the 5-parameter fit, bin-width may significantly shift the fit frequency if there is a time-dependent efficiency or additive background. Assuming a multiplicative background of the functional form in Equation (A.10), and performing an integrated average of the background over the width of the bin (bin-width = 2Δ), we find that the difference between the function and integrated average is,

$$N_\circ(t) - \bar{N}_\circ(t) = N_\circ(t)\left\{-p\,(p-2)\left[\frac{\Delta}{t-\beta}\right]^2\right\}\;, \tag{A.12}$$

where

$$\bar{N}_\circ(t) = \frac{1}{2\Delta}\int_{t-\Delta}^{t+\Delta} N_\circ(t) \ .$$

The integrated average represents what filling a histogram with bin-width 2Δ would give. From Equation (A.12), the associated timing shift δt, which makes $N_\circ(t+\delta t) = \bar{N}_\circ(t)$, is

$$\delta t = \frac{(p-2)\Delta^2}{t-\beta} \sim -1.7 \ ns \ .$$

Where a bin-width of $2\Delta \sim 0.5\mu$s, and $(t-\beta) = 30\mu$s, and $(p-2) \sim -0.7$ have been used in the estimate. This 1.7 ns shift in timing, would correspond to a 8.5 ppm shift in the measured frequency.

For the Ratio fit, the bin-width effect associated with $\bar{N}_\circ$(t) drops out, as it did for time-varying efficiency. Unfortunately, like the 5-parameter fit, there will still be a bin-width effect associated with the additive narrow-pulse background. This effect is investigated in Section 6.2.

When constructing the Ratio, there are four histograms, and four possible places to put them, so one might ask, "Which permutation should be used?" The answer is, of course, the permutation chosen is irrelevant. The fit value for each of the permutations *will not* be the same, but they *will* be within the allowed statistical uncertainty of each other (see Section 6.1).

In principle, a single histogram could be used to construct the Ratio, avoiding the permutation question altogether. However, using one histogram would mean that bins in the Ratio would be correlated (bins: i, i+4, and i-4). By using four independent ensembles to construct the Ratio, the error calculation becomes straightforward. Employing the standard error propagation on Equation (A.3), the error for each bin in the Ratio becomes

$$\begin{aligned}\delta R &= \sqrt{\left(\frac{\partial R}{\partial u}\delta u\right)^2 + \left(\frac{\partial R}{\partial v}\delta v\right)^2} \\ &= \sqrt{\left(\frac{2v}{(u+v)^2}\delta u\right)^2 + \left(\frac{2u}{(u+v)^2}\delta v\right)^2}\end{aligned}$$

$$= \sqrt{\frac{1-R^2}{(u+v)}}\ , \tag{A.13}$$

where the standard Poisson errors

$$\delta u \equiv \sqrt{u} \quad \text{and} \quad \delta v \equiv \sqrt{v},$$

have been used for constituent bin errors.

A.3 Fitting the Ratio

The function used to fit the the Ratio is essentially Equation (A.3)

$$R^{fit}(t) = \frac{A(t)\cos(2\pi f_a t + \phi)}{1 + \frac{C(t)}{N_\circ(t)e^{-t/\gamma\tau}}} = A_{eff}\cos(2\pi f_a t + \phi), \tag{A.14}$$

where

$$A_{eff} \equiv \frac{A(t)}{1 + \frac{C(t)}{N_\circ(t)e^{-t/\gamma\tau}}}.$$

The time dependency of A_{eff} was accounted for by a linear approximation (i.e. $A_{eff} = A_\circ + A_1 t$ where $A_\circ$ and A_1 are constants). Though crude, this reasonably approximated the changing asymmetry seen in the data; consequently, this reduced the χ^2 of the fits and the 'phase-pulling'-induced oscillations (see Section 6.2.1). The variable parameters used in the the Ratio fit are as follows:

- $A_\circ$ Constant asymmetry term
- A_1 Coefficient of the linear asymmetry term
- f_a (g-2) frequency
- ϕ Phase of (g-2) oscillation

Fitting was accomplished through MINUIT[54]. At a very basic level, MINUIT minimizes any function you give it by changing the values of the variable parameters. In the case of the Ratio fit, the χ^2

$$\chi^2 \equiv \sum_i \left(\frac{R_i^{data} - R_i^{fit}}{\delta R_i^{fit}}\right)^2, \tag{A.15}$$

was the object of minimization. The sum runs over all bins included in the fit. Note, the error used is the error from the fit function (δR^{fit}) *not* from the Ratio built from the data[2](δR^{data}). The error for the function is calculated by substituting R^{fit} in for R in Equation (A.13), and using the value of the 'smoothed' $(u+v)$ histogram (Figure A.1.c). Smoothing is accomplished by replacing the contents of the i^{th} bin with the average of the $(i^{th}-8)$ thru $(i^{th}+8)$ bins. Looking at how δR changes with respect to changes in R and $(u+v)$ reveals,

$$\frac{\frac{\partial(\delta R)}{\partial R}\delta R}{\delta R} = R \sim \frac{1}{3}, \quad and \quad \frac{\frac{\partial(\delta R)}{\partial(u+v)}\delta(u+v)}{\delta R} = \frac{1}{2(1-R^2)\sqrt{u+v}} \sim \frac{1}{60}.$$

Hence, δR is much more sensitive to fluctuations in R than in $(u+v)$, and the smoothing technique has little influence—and is arguably unnecessary.

Because Gaussian errors are assumed in a χ^2 fit, the stop time of the fit is determined when the errors become non-Gaussian—bins in the $(u+v)$ histogram have less than 5 counts. To reduce sensitivity to fluctuations for determining the stop time, a moving 8-bin average of the $(i^{th}-7)$ thru i^{th} bins is used to compare with the 5-count threshold.

[2] In general, the error from the data or the fit function should produce the same results for the fit parameters. However, using errors from the function makes the fit more stable—there is less fluctuation in the χ^2—and it is the correct way to proceed[53] (provided the fit function is representative of the distribution being fit).

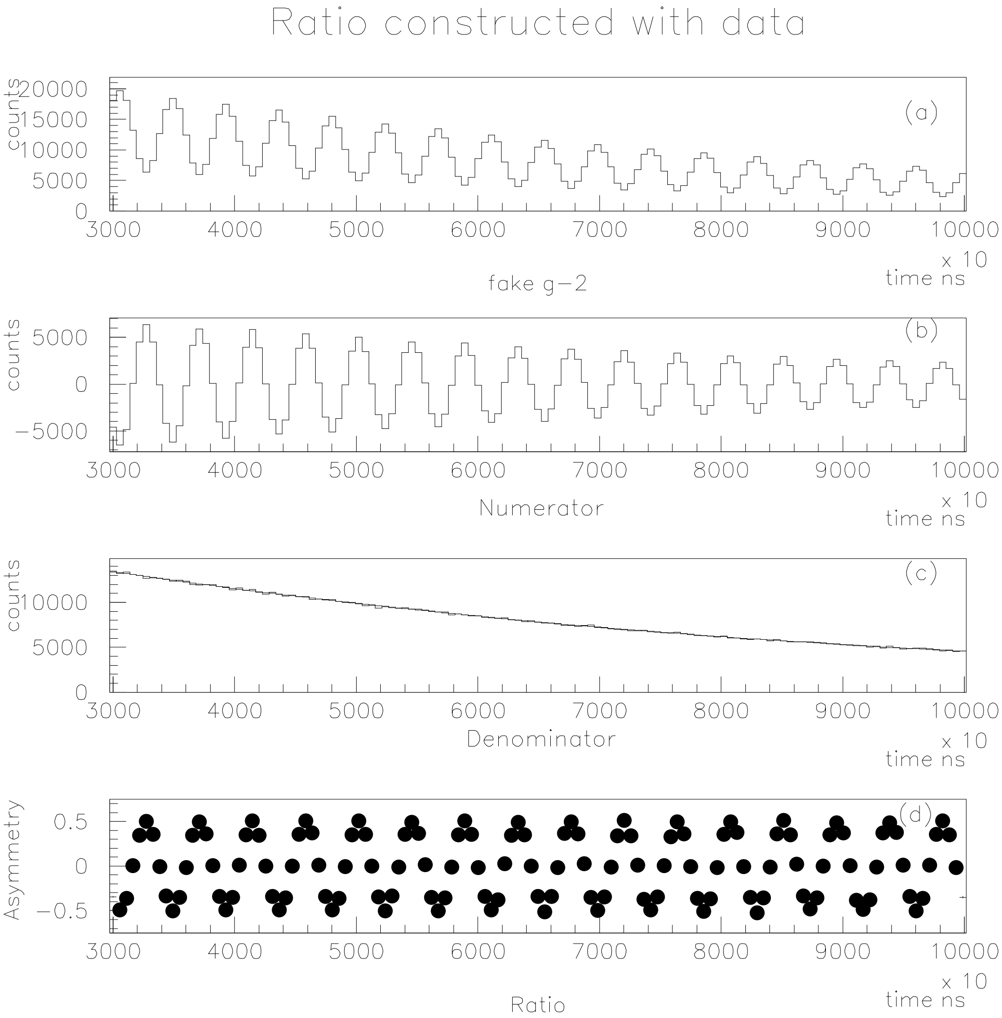

Figure A.1: The Ratio of Equation (A.3) constructed with the data: *(a)* shows the (g-2) decay electron spectrum for simulated data. *(b)* Numerator of the Ratio. *(c)* Denominator of the Ratio. *(d)* The Ratio, the vertical axis is the asymmetry of the distribution.

References

[1] J. Bailey, *et al.*, Nucl. Phys. **B150**, 1 (1979).

[2] F.J.M Farley and E. Picasso in *Quantum Electrodynamics*, (Directions in High Energy Physics, Vol. 7) ed. T. Kinoshita, (World Scientific, Singapore, 1990), p. 479.

[3] C. Kittel, *Introduction to Solid State Physics*, (Wiley, New York, 1996) p. 420.

[4] G. Bunce, *The Brookhaven Muon g-2 Experiment*, g-2 internal note 242 (1995).

[5] J. Schwinger, Phys. Rev. **73**, 416 (1948); **76**, 790 (1949).

[6] T. Kinoshita, Rep. Prog. Phys. **59** (1996) 1459–92.

[7] A. Jeffery *et al.*, *1996 Conf. on Precision Electromagnetic Measurements*, (17–20 June, 1996, Braunschweig, Germany).

[8] R. Van Dyck, Jr., *et al.*, *Phys. Rev. Lett.* **59**, 26 (1987); R.S. Van Dyke, Jr. in *Quantum Electrodynamics*, ed. T. Kinoshita, (World Scientific, Singapore, 1990), p. 322.

[9] T. Kinoshita and W.J. Marciano in *Quantum Electrodynamics*, (Directions in High Energy Physics, Vol. 7) ed. T. Kinoshita, (World Scientific, Singapore, 1990), p. 419.

[10] A. Czarnecki, B. Krause, and W. Marciano, *Phys. Rev. Lett.* **76**, 3267 (1996), and references therein.

[11] R. Alemany, M. Davier, and A. Höcker, *Eur. Phys. J.* **C2**, 123 (1998); M. Davier, and A. Höcker, *Phys. Lett.* **B419**, 419 (1998) and references therein.

[12] B. Krause, *Phys. Lett.* **B390**, 392 (1997).

[13] M. Hayakawa and T. Kinoshita, *Phys. Rev.* **D57**, 465 (1998) and references therein.

[14] A. Czarnecki, B. Krause, and W.J. Marciano, *Phys. Rev.* **D52**, R2619 (1995).

[15] P. Mery, *et al.*, *Z. Phys.* **C46** 229 (1990).

[16] T. Moroi, *Phys. Rev.* **D53**, 6565 (1996).

[17] U. Chattopadhyay, P. Nath, *Phys. Rev.* **D53**, 1648 (1996).

[18] B. L. Roberts, *Status of the Theoretical Value of (g-2)* , g-2 internal note 289 (1998).

[19] J.D. Jackson, *Classical Electrodynamics*, (Wiley, New York, 1975) p. 546.

[20] G. Danby *et al.*, to be submitted to *Nucl. Inst. and Meth.*

[21] Particle Data Group, *Phys. Rev.* **D54** (1996) 1.

[22] G. Bunce private communication.

[23] G. Knoll, *Radiation Detection and Measurement*, (Wiley, New York, 1989) p. 131ff.

[24] J. Kindem, *V1-beamline Readout System*, to be submitted as g-2 internal note.

[25] S. Sedykh, private communication.

[26] E821 Collaboration. Technical Design Report BNL AGS E821, 3rd Ed., March 1995, p. 191.

[27] A. Grossmann, Heidelberg University Dissertation (1998).

[28] S. Redin, Yale University Dissertation (1998), and references therein.

[29] R. Prigl *et al.*, *Nucl. Inst. and Meth.* **A374** (1996) 118.

[30] W.D. Phillips *et al.*, *Metrologia* **13**, 179 (1977).

[31] X. Fei, V.W. Hughes, and R. Prigl, *Nucl. Inst. and Meth.* **A394** (1997).

[32] P. Debevec, *et al.*, *Beam Profiles and Measurement of the Inflector Transmission and Ion Chamber Calibration with Activated Al-Foils*, g-2 internal note 298 (1997).

[33] S. Sedykh, *et al.*, Proceedings of the 7th Int. Conf on Calorimetry in High-Energy Physics (CALOR 97), Tucson, AZ, Nov. 9–14, 1997, (in press).

[34] P. Cushman, *et al.*, *Nucl. Inst. and Meth.* **A378** (1996) 116-130.

[35] J. Miller, R. Carey, and E. Hawk, *Measurement of the Muon Electric Dipole Moment in E821*, g-2 internal note 215 (1994)

[36] Y. Semertzidis and F. Farley, *Nucl. Inst. and Meth.* **A394** (1997) 7.

[37] J. Ouyang and W. Earle, *Rate and pileup studies for photomultiplier tubes/bases*, g-2 internal note 201 (1994).

[38] J. Kindem, Proceedings of SciFi '97, Notre Dame, IN, Nov. 3–7, 1997, (in press).

[39] D. Kawall, private communication.

[40] R. Carey, *How Does the WFD Work?*, g-2 internal note (1997).

[41] E. Hazen and G. Varner, *A Users' Guide to the g-2 Multi-hit TDC (MTDC)* g-2 internal note (1994).

[42] J. Kindem, *Design of Fast LED Pulser Module*, to be submitted as g-2 internal note.

[43] S. Giron, *et al.*, *Recording the State of the g-2 Experiment*, g-2 internal note 281 (1997).

[44] D. Miller, University of Minnesota Masters Thesis (1997).

[45] E.P. Solodov, *The WFD Pulse Shape Study*, g-2 internal note 293 (1997).

[46] H. Brown, E. Efstathiadis, B.L. Roberts, Y.K. Semertzidis *Commissioning the g-2 Storage Ring with Beam*, g-2 internal note 278 (1996).

[47] C. Timmermans, *Data Volume*, g-2 white paper (1997).

[48] F.J.M. Farley, *Effect of Stray Pulses on the g-2 Frequency*, g-2 internal note 288 (1997).

[49] *G2OFF Program Manual.*

[50] *Physics Analysis Workstation: An Introductory Tutorial*, CERN Program Library Long Writeup Q121 (1993).

[51] Y.K. Semertzidis private communication.

[52] R.M. Carey *et al.*, *A New Measurement of the Anomalous g-value of the Positive Muon*, to be submitted *Phys. Rev. Lett.*, and references therein.

[53] D. Kawall, *Statistical and Systematic Errors in Fitting* ω_a, to be submitted g-2 internal note.

[54] *MINUIT*, CERN Program Library Long Writeup D605 (1992).